5-2014

Structural, magnetic and microstructural studies of composition-modified Sm-Co ribbons

Xiujuan Jiang
University of Nebraska-Lincoln, xiujuan.jiang@huskers.unl.edu

STRUCTURAL, MAGNETIC AND MICROSTRUCTURAL STUDIES OF COMPOSITION-MODIFIED SM-CO RIBBONS

by

Xiujuan Jiang

A DISSERTATION

Presented to the Faculty of

The Graduate College at the University of Nebraska

In Partial Fulfillment of Requirements

For the Degree of Doctor of Philosophy

Major: Engineering

(Materials Engineering)

Under the Supervision of Professor Jeffrey E. Shield

Lincoln, Nebraska

May, 2014

Structural, magnetic and microstructural studies of composition-modified Sm-Co ribbons

Xiujuan Jiang, Ph.D.

University of Nebraska, 2014

Adviser: Jeffrey E. Shield

There is an increasing interest in developing desirable microstructures in hard magnetic materials. Sm-Co-based magnets, bearing superior intrinsic magnetic properties, are good candidates for further development. Two Sm-Co-based alloys, $(Sm_{12}Co_{88})_{100-x-y}Cr_yC_x$ (taking $SmCo_7$ phase) and $SmCo_{4-x}Fe_xB$ (a derivative of $SmCo_5$ phase), were produced using melt-spinning technique. The magnetic properties are correlated to the structural and microstructural properties.

Within the $SmCo_7$ (1:7) stoichiometry, cumulative effects of Cr and C additions on the structural and magnetic properties have been investigated. Experimental results have shown that these additions along with nanostructuring stabilized the 1:7 phase, refined the grain size and triggered promising modifications in the magnetic properties. Annealing was also performed to further optimize the magnetic properties. For both the as-spun and as-annealed samples, structural, magnetic and microstructural results will be shown and correlated among each other to explain observed behavior. Specifically, the maximum coercivity obtained was 10.1 kOe at 3 at.% C and 4.5 at.% Cr conditions annealed at 600 °C.

Within the $SmCo_4B$ (1:4:1) stoichiometry, efforts were made to explore the possibility of a potential exchange coupled nanocomposite based on Fe additions into the 1:4:1 structure. As-spun Fe-containing samples were amorphous. For the crystallized

samples, different Fe content brought in significant changes in the phase evolution and magnetic behavior. A secondary phase $Sm_2(Co,Fe)_{17}B_y$ was also observed at higher Fe content. We find that Fe additions increase the coercivity for up to x = 1 ($SmCo_{4-x}Fe_xB$) and increase magnetization for up to x = 2, the latter of which is highly desired for permanent magnet applications. In order to further optimize the magnetic properties of the composition with both high coercivity and magnetization ($SmCo_2Fe_2B$), secondary annealing at a lower temperature was performed. Pronounced enhancement in both magnetization and coercivity was observed. Microstructural analysis and microchemistry information obtained from TEM/HRTEM and 3D atom probe revealed the possible reasons behind the improvement.

To my parents

Acknowledgements

I had the most fortune for having Dr. Jeffrey Shield as my Ph.D. advisor, who has provided the best guidance and support that I can ever get during my academic years. I would like to thank Dr. Shield for having me work in his group, for the continuous guidance, encouragement and constructive criticism on the research projects, for the patience and understanding towards any mistakes that I have made, and above all, for recognizing and cultivating the best qualities in me. Dr. Shield has set up a role model for me for my professional development.

I also would like to thank Dr. Balamurugan from department of physics in UNL for help with the X-ray diffraction analysis, Dr. Jun Cui and Dr. Arun Deveraj from Pacific Northwest National Lab for their help in completing the atom probe studies. The collaborative efforts have been a rewarding process.

I also would like to thank all the group members and friends from NCMN facilities that I have worked with and shared experiences with. The research input they have provided and the joyful & stimulating discussions I had with them are important ingredients in my Ph.D. career. Their continuous encouragement and support cannot be overstated. I also would like to thank Evan and Najla for their help in making samples.

I would like to thank my friends and family, especially Zhifeng for being there for me always while I was faced with challenges in this process.

I also would like to take this opportunity to thank the rest of the committee members: Dr. Jinsong Huang, Dr. Michael Nastasi, Dr. David Sellmyer, Dr. Ralph Skomski, as well as Dr. Brian Robertson for their time commitment and valuable input

regarding my research. Thanks are especially due to Dr. Skomski for the valuable discussions.

The research conducted in this dissertation cannot be accomplished without the funding from Army Research Office and National Science Foundation. Thanks are also due to Central Facilities of the Nebraska Center for Materials and Nanoscience supported by the Nebraska Research Initiative and Environmental Molecular Sciences Laboratory (EMSL) at Pacific Northwest National Laboratory (PNNL) supported by PNNL Multiscale Synthesis and Simulation Initiative.

Freedom to differ is not limited to things that do not matter much. The test of its substance is the right to differ as to things that touch the heart of the existing order.

Robert H. Jackson, 1943

Table of Contents

List of figures

List of tables

Chapter 1 Introduction

1.1 Background

Permanent magnets are indispensable components in countless applications, such as motors and actuators, household appliances, medical devices (MRI) and electronics (portable audio/video devices). The function of a permanent magnet is usually to provide magnetic flux in the working gap of a device, which can be generally divided into four categories [1]:

a) Applications that employ the tractive or repelling force of a magnet (either between a magnet and ferromagnetic materials or attraction/repulsion between two magnets). Examples may include magnetic separators, magnetic holding/bearing devices and magnetic torque drives;
b) Applications that convert mechanical energy to electrical energy via the magnetic field flux. Generators and alternators belong to this category;
c) Applications that convert the electrical energy to mechanical energy. Motors, loudspeakers and actuators are the common examples of this category;
d) Applications that direct, shape and control electron or ion beams using a magnetic field. Several common examples include magnetrons, traveling wave tubes and ion pumps.

Thanks to the rapid technological development in other areas of the industry, permanent magnets are facing more challenges to keep pace. Despite the high demand for permanent magnets in recent years driven by hybrid electric vehicles and wind power generation, research and development in permanent magnets have mostly been seeking to

improve energy efficiency (more energy with smaller volume) and cost effectiveness. First of all, focus has been given to increase the strength of a magnet—characterized by the maximum energy product ($BH|_{max}$) — in order for the magnet to be more energy efficient. Additionally, since the commercial drivers mentioned above require that the permanent magnets operate at elevated temperatures (above 200 ºC) and the maximum operating temperature of a magnet is related to another attribute of permanent magnets—the Curie temperature T_c (the temperature at which the magnets lose their functionality), additional consideration has also been given to enhance $BH|_{max}$ at elevated temperature via increasing T_c of a magnet. Last but not least, since the type of permanent magnets attributing to most of the magnet market share—Dy compensated NdFeB magnets—contain economically and politically critical elements (Nd and Dy), the research community is also exploring alternative magnets without critical elements. Additionally, since the production of Sm-Co high temperature magnets $Sm(CoFeZrCu)_7$ requires a complex heat treatment procedure, simplified processing is of interest.

The aforementioned figure of merit of permanent magnets—$BH|_{max}$ —is governed by the more fundamental characteristics of the magnetic materials, which comprise both the intrinsic and extrinsic parameters. The former includes saturation magnetization M_s and the first anisotropy constant K_1, while the latter incorporates remanent magnetization M_r and coercivity H_c. Meanwhile, the temperature dependence of the energy product can be simply characterized by two additional parameters, the temperature coefficients of either remanence (α) or coercivity (β), where the lower the parameter, the better the magnet performs when temperature varies. As a result, a desirable permanent magnet characterized by a large $BH|_{max}$ can essentially be obtained by enhancing one or several

of the fundamental parameters. From a materials engineering perspective, it is well known that the intrinsic parameters can be mostly controlled by composition variations, while the extrinsic properties can be vastly manipulated by processing techniques and processing conditions.

A historical development of different hard magnetic materials with the corresponding energy product can be found in Fig. 1. As the energy product increases both within each magnet and among different magnets, the volume of the magnets providing the same amount of magnetic energy decreases tremendously. The current commercially available hard magnets mainly consist of hard ferrites, Alnico, $SmCo_5$ and Sm_2Tm_{17} (refers to $Sm(CoFeZrCu)_7$), SmFeN and NdFeB.

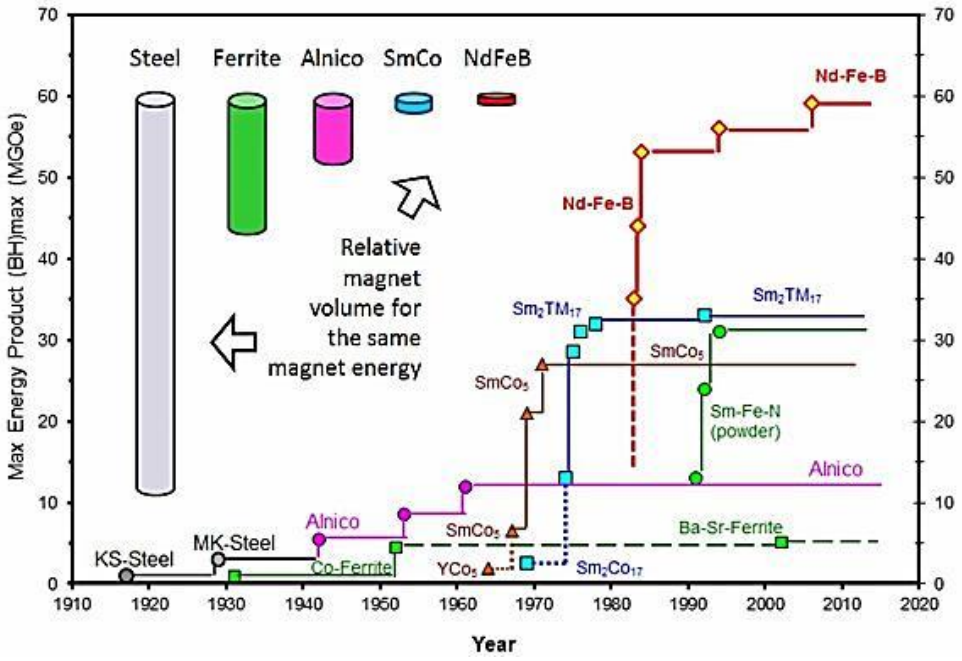

Fig. 1.1 A historical development of energy product for different permanent magnets [2]

The noteworthy intrinsic properties of the different types of permanent magnets including magnetization M_s, anisotropy constant K_1, Curie temperature T_c and the maximum operating temperature can be compared in Table 1.1.

Table 1.1 Different parameters of commercial permanent magnets [3]

Materials	**M_s (emu/cm^3)**	**K_1 (10^7 erg/cm^3)**	**T_c(°C)**	**T_{max}(°C)**	**α (%/◦C)**	**β (%/◦C)**
$BaFe_{12}O_{19}$	380	0.33	467	300	-0.2	0.27
Alnico	1120	0.68*	937	540	-0.02	-0.01
$SmCo_5$	860	17.2	747	250	-0.04	-0.4
Sm_2Tm_{17}	970	4.2	810	350	-0.035	-0.2
$Sm_2Fe_{17}N_3$	1226	8.6	476	80	-0.06	-0.51
$Nd_2Fe_{14}B$	1280	4.9	265	180	-0.1	-0.55

*shape anisotropy

Hard ferrites ($BaFe_{12}O_{19}$ is one type of hard ferrites) are known for their low cost and high electrical resistivity. Alnico magnets have the highest Curie temperature amongst all the permanent magnets in addition to their extremely low temperature coefficients. However, due to their low anisotropy constant, some of the applications are being superseded by NdFeB magnets. Sm-Co magnets, besides their high magnetic strength and high Curie temperature, also are famous for their corrosion resistance which allows them to work in severe environments. SmFeN materials are mostly used in bonded

magnets which are non-conductive and can form complex shapes. NdFeB magnets, due to their relatively new discovery in the timeline, experienced incremental enhancement in the energy product during recent years and are by far the strongest magnets. However, the price and availability of the raw Nd and Dy (a substitute of Nd) elements are a limiting factor for NdFeB's broader usage.

Therefore, recent research efforts, on one hand, aim to optimize the traditional magnets given the advanced processing and characterization techniques which were hitherto not applicable. For instance, in Nd-Fe-B magnets, grain boundary structure is found to play a significant role in altering the magnetic properties, especially coercivity [4]. Research has been carried out to understand the mechanism of grain boundary effect on both commercial magnets [5] and stoichiometric magnets under different processing [6, 7]. The effect of post-sinter annealing [8] and various alloying [9, 10] are also extensively studied due to their beneficial effect in improving the grain boundary structure. Sm-Co 1:7 phase, due to its high magnetocrytalline anisotropy, has attracted extensive attention for its potential in high temperature applications [11, 12]. A comprehensive study of the alloying effects in this system and the impact on magnetic properties can be found in ref. [13]. On the other hand, there has been a surge to look for new magnetic phases or structures which avoid using critical elements. A review of rare earth-free magnetic materials and their magnetic performance can be found in several sources [14, 15]. Transition metal-Co based materials, such as Hf-Co and Zr-Co, show potential in proving moderate energy product for next generation magnets [16-18]. It is also worth mentioning that the combination of hard and soft phases, in order to take the best of both worlds, also has been largely endeavored and tested during the past two

decades [19]. The structural and magnetic properties of materials with certain soft phase (including $Fe_{65}Co_{35}$, α-Fe, FeNi or Fe_3B phase) selectively combined with Sm-Co or NdFeB magnets have been investigated [20, 21].

While the intrinsic properties of a magnet, determined by the electronic structure (short-range order), are mostly controlled by a material's composition, extrinsic properties which are highly dependent on microstructures can be manipulated largely by microstructure control. Microstructure can be defined as any feature within a material which is not visible to the naked eye. In magnetic materials, microstructure can include grain size, phase components and distribution, crystallographic texture, defects and grain morphology. Developing and controlling microstructure has also been the bottleneck which is limiting further breakthroughs in permanent magnets [22, 23]. Unfortunately, there is no single rule for the effect of different microstructures on the magnetic behavior of a particular material system. The fact that there is not only one microstructural feature in a real material in observation further complicates the attempt in both developing the optimal microstructure and understanding the interplay between microstructure and the magnetic properties. Furthermore, microstructure can be controlled via different strategies, for instance, composition variations (alloying and doping), processing conditions manipulation (including post treatment) and differing processing techniques. To simplify the matter, the discussion is usually limited to the microstructural control within a particular material system produced via a specific processing technique.

The present study will contribute to the understanding of microstructural effects on the magnetic behavior in modified Sm-Co magnets produced via rapid solidification (i.e. melt-spinning). Magnetism and microstructure will be the themes of the current

dissertation. The fundamentals of magnetism and the generally accepted interplay between microstructure and magnetism can be found in chapter 2. The Sm-Co system was chosen mainly because of its intriguing phase formations when alloying, intrinsically high anisotropy and low temperature coefficients. The particular materials of interest are $(Sm_{12}Co_{88})_{100-x-y}Cr_yC_x$ (forming the $SmCo_7$ phase) and $SmCo_{4-x}Fe_xB$ (a derivative of $SmCo_5$ phase) (note "x" does not necessarily take the same value in different systems). A complete description of the structural and magnetic aspects of the Sm-Co system will be recounted in chapter 3.

The overall study takes the experimental approach for the synthesis (arc melting and melt-spinning) and characterization, including structural (XRD), thermal (DTA), magnetic (AGFM and SQUID) and microstructural investigations (TEM, HRTEM and 3D atom probe). A brief introduction of each experimental method including the basics and a general procedure will be explained and illustrated in chapter 4. Additionally, for $SmCo_7$, a semi-empirical method was also attempted in helping understand the fundamental cause for the anisotropy variations of different alloying within the SmCo 1:7 phase, which can be found in chapter 5.

Structural and magnetic behavior was thoroughly evaluated using different characterization techniques. The effect of Cr and C on the structural and magnetic properties of $(Sm_{12}Co_{88})_{100-x-y}Cr_yC_x$ (with x ranging from 1 to 6 with a fixed ratio of y/x = 3/2) magnets will be discussed in chapter 6, which has been published in ref [24]. Specifically, the microstructural evolution after annealing was correlated with the magnetic properties variations in $(Sm_{12}Co_{88})_{92.5}Cr_{4.5}C_3$. The phase formation and magnetic behavior of $SmCo_{4-x}Fe_xB$ (x = 0, 0.25, 0.5, 0.75, 1 and 2) were investigated as a

function of Fe content x, which can be found in chapter 7, which has been published in ref [25]. The grain size and distribution were associated with the magnetic reversal behavior. For $SmCo_2Fe_2B$, the effect of secondary annealing was also discussed in the context of microstructural variations. Precipitation and a grain boundary phase were found to be responsible for the magnetic properties enhancement. A detailed analysis from HRTEM and 3D atom probe results for multistage annealed $SmCo_2Fe_2B$ can be found in chapter 8, which has been published in ref [26]. The summary and conclusions of the dissertation will be presented in chapter 9.

1.2 Objectives

The present study aims to optimize the composition and processing procedures for excellent magnetic properties in compositionally modified Sm-Co magnets synthesized via rapid solidification. The nanostructural features formed during rapid solidification created unseen microstructural features compared to that synthesized via conventional techniques. The investigation and understanding of the relationship between microstructure and magnetic properties are inevitable in designing future magnetic materials and are critical in alloy design.

Specifically, the objectives of this study include the following aspects:

- To examine the effect of different alloying on the magnetocrystalline anisotropy in the $SmCo_7$ structure from thermodynamic considerations;
- To investigate the combined effects of Cr and C on the structural and magnetic properties of the $SmCo_7$ system;

- To study the effect of Fe on the structural and magnetic properties of the $SmCo_4B$ structure;
- To understand the correlation between microstructure and magnetic properties in the multistage heat treated $SmCo_2Fe_2B$ composition.

References

[1] http://www.arnoldmagnetics.com/Permanent_Magnet_Applications_Guide.aspx.

[2] http://www.magnetnrg.com/pm-history.html.

[3] J.M. Coey, Magnetism and magnetic materials, Cambridge University Press, 2010.

[4] K. Hono, H. Sepehri-Amin, Scr. Mater., 67 (2012) 530-535.a

[5] H. Sepehri-Amin, T. Ohkubo, T. Shima, K. Hono, Acta Mater., 60 (2012) 819-830.

[6] H. Sepehri-Amin, T. Ohkubo, K. Hono, Acta Mater., 61 (2013) 1982-1990.

[7] H. Sepehri-Amin, Y. Une, T. Ohkubo, K. Hono, M. Sagawa, Scr. Mater., 65 (2011) 396-399.

[8] W.F. Li, T. Ohkubo, K. Hono, Acta Mater., 57 (2009) 1337-1346.

[9] Y. Xu, M. Kramer, Y. Wu, K. Dennis, R. McCallum, J. Appl. Phys., 99 (2006) 08B511-508B511-513.

[10] J. Ni, T. Ma, M. Yan, J. Magn. Magn. Mater., 323 (2011) 2549-2553.

[11] Z. Zhang, X. Song, W. Xu, Acta Mater., 59 (2011) 1808-1817.

[12] X. Song, N. Lu, M. Seyring, M. Rettenmayr, W. Xu, Z. Zhang, J. Zhang, Appl. Phys. Lett., 94 (2009) 023102-023102-023103.

[13] Y. Guo, W. Feng, W. Li, J. Luo, J. Liang, J. Appl. Phys., 101 (2007) 023919--023917.

[14] J. Coey, Scr. Mater., 67 (2012) 524-529.

[15] M. Kramer, R. McCallum, I. Anderson, S. Constantinides, JOM, 64 (2012) 752-763.

[16] M.A. McGuire, O. Rios, N.J. Ghimire, M. Koehler, Appl. Phys. Lett., 101 (2012) 202401.

[17] W. Zhang, X. Li, S. Valloppilly, R. Skomski, J. Shield, D. Sellmyer, J. Phys. D: Appl. Phys.,, 46 (2013) 135004.

[18] B. Balasubramanian, B. Das, R. Skomski, W.Y. Zhang, D.J. Sellmyer, Adv. Mater., 25 (2013) 6090-6093.

[19] M. Lamichanne, B. Rai, S. Mishra, V. Nguyen, J. Liu, Open J. Compos. Mater., 2 (2012) 119-124.

[20] L.M. Ortega, J.E. Galindo, J.F. Mancilla, C. Santillan, J.M. Aquino, J. Appl. Phys.,, 111 (2012) 07B505.

[21] C.B. Rong, D. Wang, V. Van Nguyen, M. Daniil, M.A. Willard, Y. Zhang, M. Kramer, J.P. Liu, J. Phys. D: Appl. Phys., 46 (2013) 045001.

[22] O. Gutfleisch, J. Phys. D: Appl. Phys., 33 (2000) R157.

[23] O. Gutfleisch, M.A. Willard, E. Brück, C.H. Chen, S. Sankar, J.P. Liu, Adv. Mater., 23 (2011) 821-842.

[24] X. Jiang, J.E. Shield, J. Magn. Magn. Mater., 333 (2013) 63-68.

[25] X. Jiang, B. Balamurugan, J.E. Shield, Manuscript submitted, J. Allo. Compd., 2014.

[26] X. Jiang, A. Devaraj, B. Balamurugan, J. Cui, J.E. Shield, J. Appl. Phy., 115 (2014) 063902.

Chapter 2 Magnetism and microstructure

This chapter first briefly introduces the fundamentals of magnetism including the sources of magnetism and anisotropy, domain and domain walls, and magnetization reversal mechanisms in magnetic materials. The generally accepted correlation between microstructural features and magnetic properties in hard magnets is also described.

2.1 Magnetism and magnetic properties

Magnetism is a phenomenon in which materials assert an attractive or repulsive force or influence on other materials. Although it has been discovered for thousands of years, the fundamental understanding has not started since very recent years. This section will briefly discuss the underlying mechanisms of magnetism and different macroscopic magnetic properties.

2.1.1 The source of magnetism

There are some well-known examples of materials that exhibit magnetic behavior, such as iron, some steels, and the naturally occurring mineral lodestone. The fundamental characteristic they share is the magnetic moment in the materials, which is generated by moving electrically-charged particles—electrons. In other words, the macroscopic magnetic properties of materials are a consequence of magnetic moments associated with individual electrons. The magnetic moment of an individual atom is a sum of the spin moment and orbital moment, taking into account the moment cancellation.

Depending on how the electrons and the atomic magnetic dipoles within materials respond to an external magnetic field, magnetism can be classified into different

categories including diamagnetism, paramagnetism, and ferromagnetism; in addition, antiferromagnetism and ferrimagnetism are considered to be subclasses of ferromagnetism. All materials exhibit at least one of these types. In diamagnetic materials, the applied field induces a change in the orbital motion of electrons which results in an extremely small magnetic response in the direction opposite to that of the applied field. It is characterized as nonpermanent and persists only while an external magnetic field is maintained. It should be noted that diamagnetism exists in all materials. However due to its weak nature, it can only be observed when other types of magnetism are totally absent. On the other hand, in paramagnetic materials, each atom already possesses a permanent dipole moment in the form of incomplete cancellation of electron spin and/or orbital magnetic moments. An external magnetic field will align the magnetic moments in the field direction which would otherwise remain random. However, the magnetic moments have no mutual interaction between adjacent dipoles.

Both diamagnetism and paramagnetism are considered nonmagnetic since they only exhibit magnetization in the presence of a magnetic field (Fig. 2.1), as opposed to ferromagnetic materials which possess a permanent magnetic moment even in the absence of a magnetic field, as shown in Fig. 2.2(a). Here the coupling between adjacent atoms cause net spin magnetic moments to align with one another. In contrast, antiferromagnetism refers to the alignment of the spin moments of neighboring atoms or ions in exactly opposite directions; antiferromagnetism can be found in MnO. It is schematically illustrated in Fig. 2.2(b). It is apparent that the opposing magnetic moments cancel one another resulting in no net magnetic moment. Some ceramic materials display ferrimagnetic behavior, which is similar to ferromagnetism, but with different sources of

net magnetic moments. One typical example is Fe_3O_4, schematically illustrated in Fig. 2.2(c).

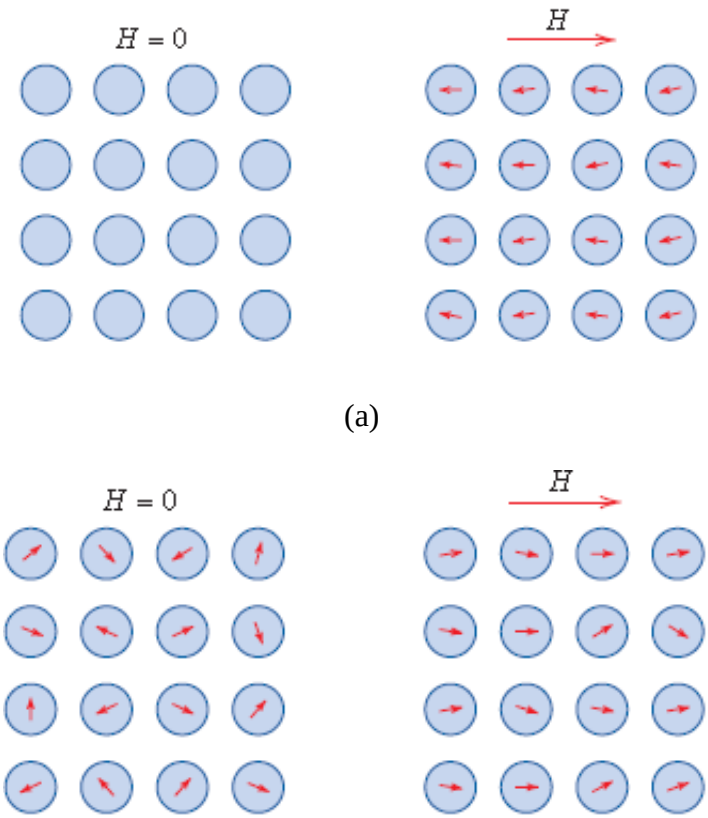

Fig. 2.1 Schematic illustration of the atomic dipole arrangement in a (a) diamagnetic materials and (b) paramagnetic materials [1]

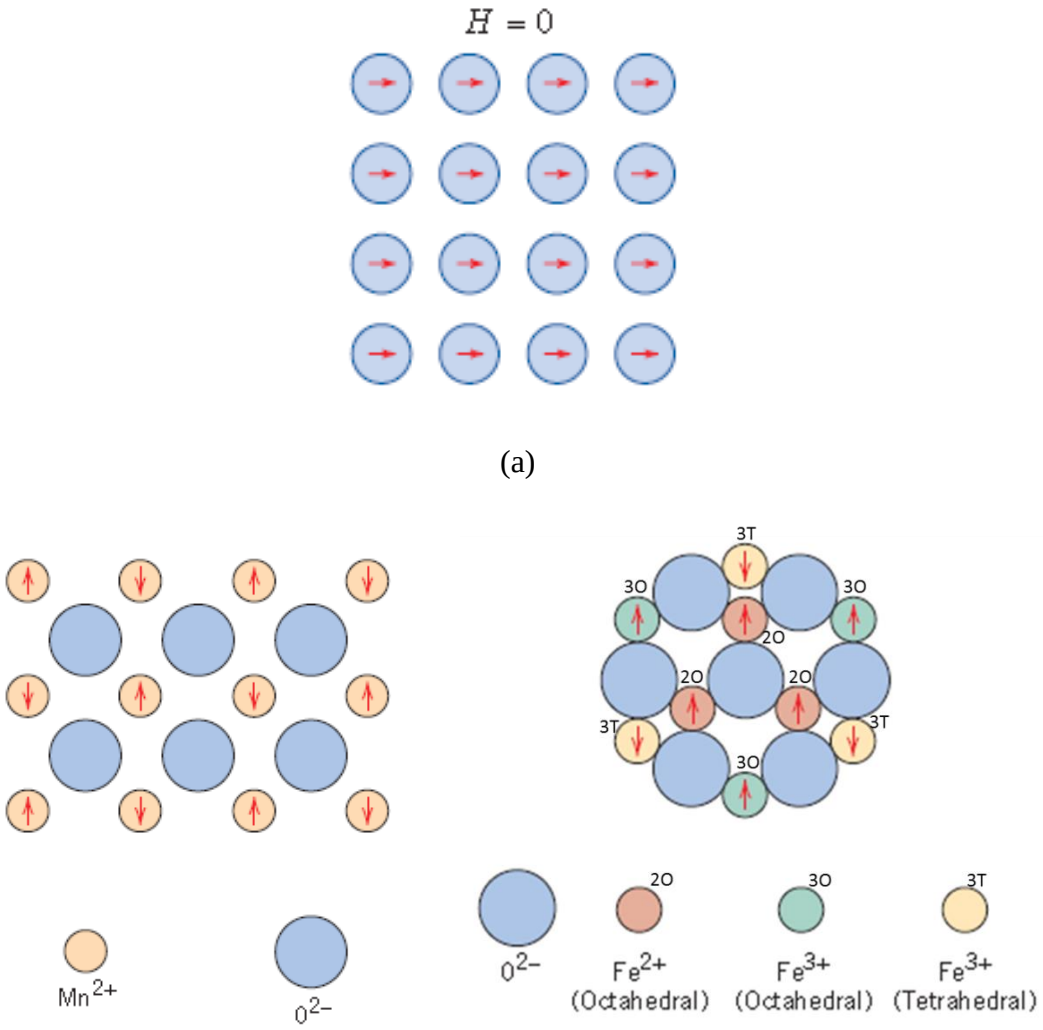

Fig. 2.2 Schematic illustration of (a) ferromagnetism: mutual moment alignment; (b) antiferromagnetism in Manganese oxide: antiparallel alignment of spins and (c) ferrimagnetism configuration in Fe_3O_4 [1]

Elemental materials that exhibit ferromagnetism at room temperature include α-Fe, Co, Ni and the rare earth element Gd. The permanent magnetic moments in ferromagnetic materials results mostly from uncancelled electron spins as well as a small amount of orbital magnetic moment contribution. The coupling interaction between

adjacent atoms, according to the Weiss theory, is caused by a powerful "molecular field", which aligns the atomic moments. This interaction is also called the "exchange force" [2], which can be represented by the exchange energy E_{ex}. If two atoms *i* and *j* have spin angular momentum $S_i h/2\pi$ and $S_j h/2\pi$, respectively, the exchange energy between them is given by

$$E_{ex} = -2J_{ex}S_i \cdot S_j = -2JS_iS_j \cos\varphi \tag{2.1}$$

Where J_{ex} is the exchange integral, which occurs in the calculation of the exchange effect, and φ is the angle between the spins. If J_{ex} is positive, E_{ex} is a minimum when the spins are parallel (cos φ = 1) and a maximum (cos φ = -1) when they are antiparallel. If J_{ex} is negative, the lowest energy state results from antiparallel spins. Since ferromagnetism is due to the alignment of spin moments on adjacent atoms, a positive value of the exchange integral is therefore a necessary condition for ferromagnetism to occur [3, 4].

Fig. 2.3 shows the postulated variation of the exchange integral as a function of the ratio between r_a (the radius of an atom) and r_{3d} (the radius of the 3*d* shell of electrons). It can be concluded that only materials with a certain range of ratio can exhibit ferromagnetism. It should be noted that this concept is under debate for risk of being oversimplified regarding the underlying mechanism for ferromagnetism, but it offers some simple rationale.

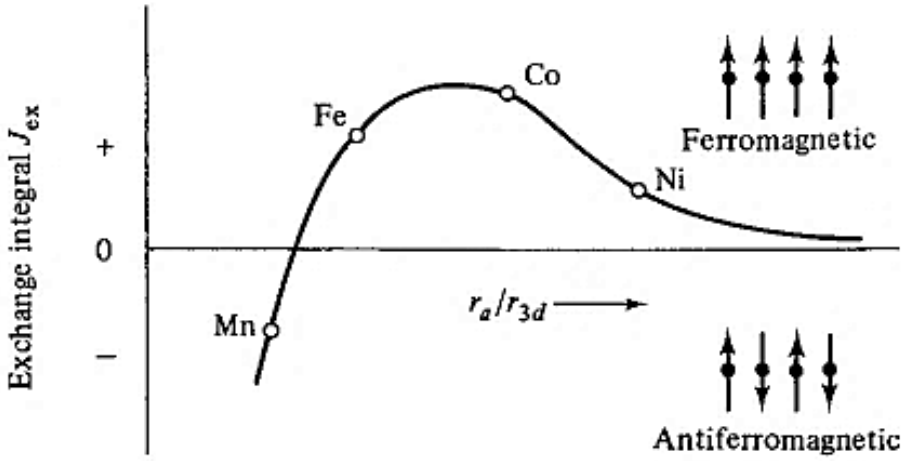

Fig. 2.3 The schematic Bethe-Slater curve [2]

Ferromagnetic materials exhibit non-linear magnetization behavior with respect to an external magnetic field, known as hysteresis loops (Fig. 2.4). According to the hysteric behavior, ferromagnets are divided into two types. Usually, when the coercivity of a ferromagnet is less than 12.6 Oe (200 kAm^{-1}), it is defined as a soft magnet. When the coercivity is larger than 2.5 kOe (1 kAm^{-1}), it is considered a hard magnet or a permanent magnet [5]. A schematic comparison of the two types of magnets is shown in Fig. 2.4. Soft magnets are characterized by their easy switching of magnetization and can be used for flux enhancement, while hard magnets are used to provide magnetic field due to their "permanent" magnetization once magnetized.

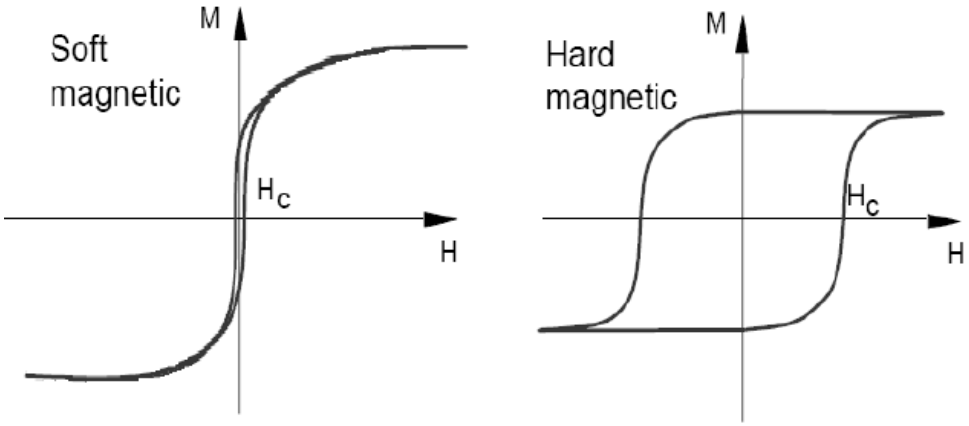

Fig. 2.4 Typical hysteresis loops for soft and hard magnets [6]

For hard magnets, both M-H and B-H curves are important, shown in Fig. 2.5. The M-H curve will be discussed first. When the applied field reaches a point where it can no longer increase the magnetization, saturation magnetization M_s can be obtained. When the field decreases to zero, the remaining magnetization is defined as remanence. When the field extends to the opposite direction, the field strength needed to reduce the magnetization to zero is the intrinsic coercivity. In order to calculate the energy product (BH) of the material, the M-H curve is transformed into B-H curve by using one of the following expressions, $B = 4\pi M + H$ (cgs unit system) or $B = \mu_0 (M + H)$ (SI unit system). The $(BH)_{max}$ is the maximum rectangular area within the second quadrant. It is worth noting that given sufficient external field, hysteresis loops usually are symmetric.

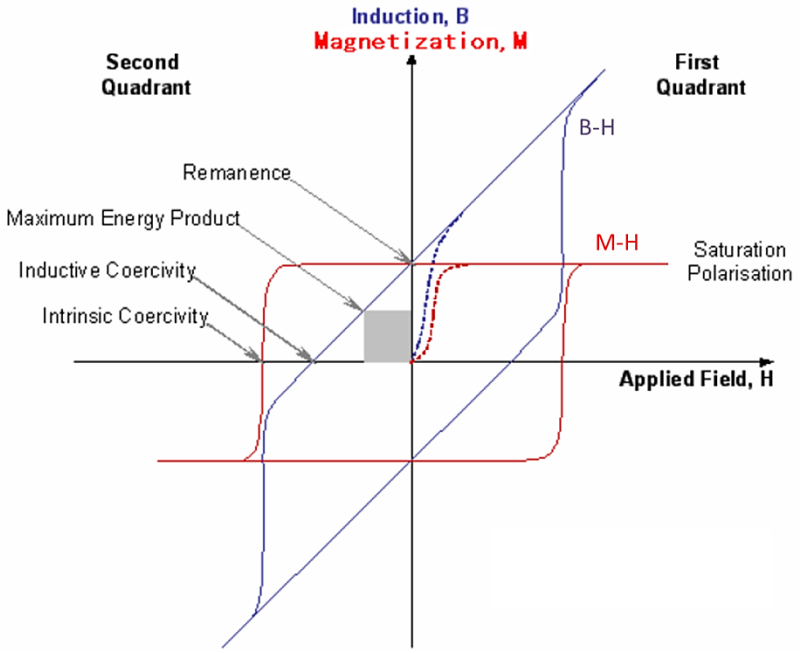

Fig. 2.5 Typical M-H and B-H hysteresis loops [6]

The magnetic moments in ferromagnetic materials are strongly affected by temperature. The thermal vibrations of atoms tend to randomize the directions of any moments that may be aligned, which counteract the coupling forces between the adjacent atomic dipole moments, causing some dipole misalignment, regardless of whether an external field is present. The direct effect is the decrease of saturation magnetization with increasing temperature. At absolute temperature $T = 0\ K$, the saturation is a maximum. For ferromagnetic materials, at Curie temperature T_c, the saturation magnetization decreases to zero.

2.1.2 Sources of magnetic anisotropy

Magnetic anisotropy refers to the directional dependence of the magnetic properties, specifically the preference of magnetization to lie in a particular direction known as an easy axis. Several sources of anisotropy include magnetocrystalline

anisotropy, shape anisotropy, stress anisotropy and induced anisotropy (e.g. by magnetic annealing or plastic deformation). Here the discussion will center on the magnetocrystalline anisotropy since it is the only intrinsic one and also the one related to this dissertation.

The physical origin of magnetocrystalline anisotropy is spin-orbit coupling [2]. By comparison, the coupling between spins can be strong, but the exchange energy is isotropic, independent of the direction of the spin axis relative to the crystal lattice. On the other hand, the orbit-lattice coupling is also strong, but much weaker than the crystal field and/or hopping energies. This leads to the quenching of the orbital moment, as in Fe. Simply speaking, orientations of the orbits are bound strongly to the lattice, which prevents them from turning toward the applied field direction. In the case of dominating spin-orbit coupling, when the applied field tries to reorient the spin of an electron, the orbit of that electron also tends to be reoriented. This is the case for rare earth elements, such as Sm. The energy required to rotate the spin system away from the easy direction, referred to as the anisotropy energy and represented by the anisotropy constants such as K_1 and K_2. For a material with uniaxial anisotropy, the magnetocrystalline anisotropy energy can be expressed as $E \sim -K_1 V sin^2\theta$, here θ refers to the angle between the magnetization direction and the easy axis and V is the volume of the magnet. Magnetocrystalline anisotropy, similar to magnetization, also decreases with increasing temperature. For hard magnetic materials, uniaxial anisotropy with a large K_1 is desired, whereas either easy plane anisotropy or multiple easy axes in cubic symmetry is preferred for soft magnetic properties.

2.1.3 Domains and domain walls

One of the characteristics of ferromagnetic materials is the presence of magnetic domains [7] below the Curie temperature. Domains, which are usually microscopic in size, are small regions within which the local magnetization is saturated. Some materials are made up of a large number of domains separated by domain walls, the interfaces between domains.

The formation of a domain wall can be explained considering a large single crystal (Fig. 2.6). When this large single crystal is uniformly magnetized forming a single domain, the surface charges at both ends will create a demagnetizing field in the opposite direction to the domain saturation direction. The energy related to the surface charge distribution is the magnetostatic energy, which can be approximately halved if the magnetization within forms a closed loop (e.g. magnetization in opposite directions) within the single crystal. It is because when the opposite charges are brought closer together, the spatial extent of the demagnetization field is also decreased.

However, subdivision into domains also requires energies to create and maintain the domain walls. As a result, domain wall formation is a competition between the magnetostatic energy and the domain wall energy. In real materials, with the interplay of the magnetostatic energy and exchange energy, the domain wall states are the result of both long range and short range effects, and are thus dependent on the grain size of the material. Equilibrium can be reached when the total energy is a minimum. If the grain size of a specific material decreases to a critical grain size below which it can no longer support a domain wall, a “single-domain” grain is formed. Intrinsically, the magnitudes of these energies are also strongly dependent on temperature and the composition. The

wall energy can generally be described as $\gamma\pi R^2$ where $\gamma = 4\sqrt{(AK_1)}$ (specific domain wall energy), whereas the magnetostatic energy is $\mu_0 M_s^2 V/12$ [8], hence the single domain radius can be obtained as $R_{SD} = \frac{36\sqrt{AK}}{\mu_0 M_s^2}$ [2], where μ_0 is vacuum permeability. The single domain radius, strongly dependent on K_1 can range from a few nm in soft magnets to micron size in hard magnets.

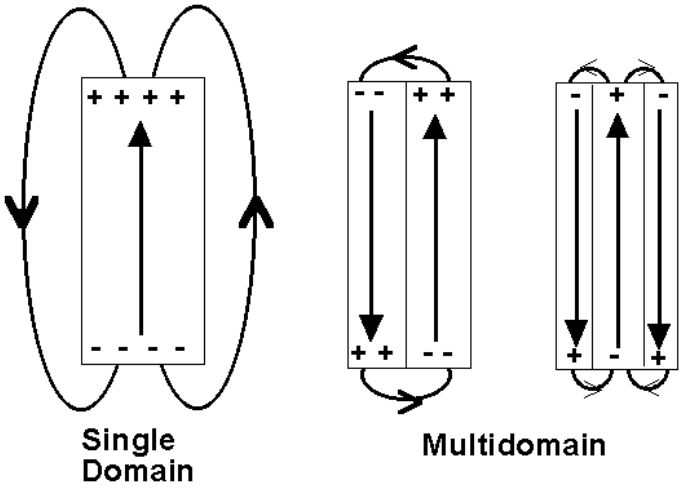

Fig. 2.6 An illustration of the formation of a domain wall [9]

The thickness of a domain wall (Fig. 2.7), is governed by exchange and magnetocrystalline energy. The exchange energy, promoting parallel alignment of spins, prefers a gradual change of magnetization (i.e. a wide domain wall). In contrast, the magnetocrystalline energy acts to align the magnetization along the easy axis of magnetization and thus favors a thin domain wall. The resulting domain wall thickness can be calculated using the expression $\delta = \pi\sqrt{(A/K_1)}$, where A is the exchange stiffness (usually on the order of 10^{-13} J/m) and K is the anisotropy constant of the material. The domain wall generally has a finite width ranging from 0.1 nm to100 nm. For instance, δ is 14 nm for Co and 3.6 nm for $SmCo_5$ [10].

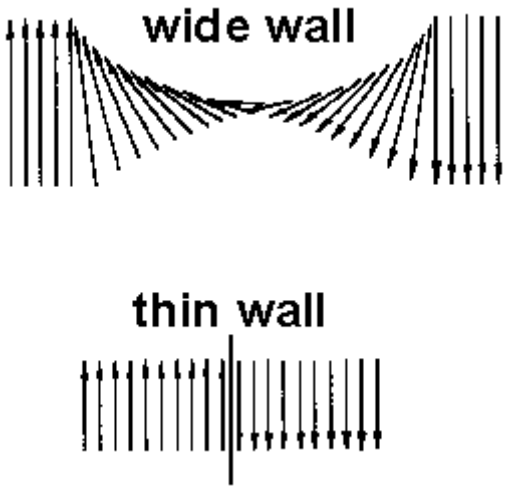

Fig. 2.7 A comparison of thick and thin domain walls [9]

2.1.4 Magnetization reversal mechanisms

After a material is magnetized in one direction, a field in an opposite direction will act to reverse the magnetization. For a material which shows single-domain behavior, ideally, the magnetization reverses by spin rotation, which can be coherent (spins of atoms remain parallel during the rotation) or incoherent [2]. On the other hand, for materials which have large particles and form multidomains, the reversal usually occurs through domain wall motion. This section focuses on the discussion of domain wall motion since it is closely related to this research.

The magnetization reversal process involves the nucleation of reversed magnetic domains and their growth through domain wall motion. A ferromagnetic material can be made hard or soft by manipulating the reversal process.

In an ideal homogeneous defect-free material, the external field should overcome the anisotropy field of the material and the resultant coercivity can be expressed as

$H_c = \frac{2K_1}{M_s} - N_{eff}M_s$ [11]. N_{eff} is the demagnetizing factor due to local stray fields which assist the nucleation of reversal domains under a reverse applied field. However, in most cases, real materials are subject to microstructural imperfections. One possibility is that those imperfect regions can lower the anisotropy field and act as ***nucleation*** sites of reversed domains at a relatively low field, resulting in a lower coercivity. Another possibility is that the structural defects can act as domain wall ***pinning*** centers which hinder domain wall motion, increasing the coercivity.

(1) Nucleation

In order to incorporate the microstructural effects on the reduction of the local anisotropy field, the expression for coercivity is modified to $H_C = \alpha_\varphi \alpha_k \frac{2K_1}{M_S} - N_{eff}M_s$ [12]. α_k and α_φ refer to the reductions of the anisotropy constant due to microstructural inhomogeneities and the grain misalignment, respectively [12]. Several types of regions can reduce the local anisotropy, including grain boundaries, granular inclusions and lamellar precipitates [13], small changes in lattice parameters due to deviation in stoichiometric compositions [14], and lattice imperfections such as lattice disorders, point defects or dislocations [15].

(2) Pinning

After nucleation of a reversed domain, the external field exerts a driving force for domain wall motion. The domain wall motion can be hindered by various kinds of structural defects such as voids, point defects, dislocations, second phases and antiphase boundaries within the material [16], all of which act as pinning centers.

The pinning behavior of either structural defects or secondary phases depends on two factors:

(1) The size of the defect;

(2) The difference in magnetocrystalline anisotropy between the localized anisotropy of the defect or the precipitate and the bulk anisotropy of the matrix.

For the first factor, effective pinning centers should be of similar size to the domain wall thickness of the matrix material [17]. In order to take the second factor into consideration, Kronmuller proposed an expression of coercivity for $SmCo_5$ with Sm_2Co_{17} precipitates, which is $H_C = \frac{1}{M_S^P}\left(\pi\frac{\bar{\gamma}\sqrt{2}}{2d} + \frac{\overline{\delta_0}}{2}\frac{dK}{dx}\right)$ [18, 19]. In this expression, M_s^P refers to the saturation magnetization of the precipitate, *d* is the diameter of the precipitate and *r* is the dimension of the transition region. The domain wall energy (γ) and the domain wall thickness (δ) are calculated using the average anisotropy constants of the matrix and the precipitate. The first term of this expression is determined by the microstructural scale while the second term is determined by the magnetocrystalline anisotropy constant gradient. It can be seen that in order to achieve the highest possible coercivity, the anisotropy gradient *dK/dx* between precipitate and matrix should be maximum.

It has been shown that point defects, with sufficient density, can act as pinning centers by changing the exchange interaction and the magnetocrystalline anisotropy [20]. A high density of dislocations in cold rolled steel provided higher coercivity due to the pinning resulted from the magnetostrictive interaction between the wall and the dislocation [21]. Antiphase boundaries, a surface or interface between two halves of an ordered crystal structure [22], also showed pinning behavior in FePt [23] and MnAl [24, 25]. It has been suggested that the local magnetocrystalline anisotropy is low at the

boundaries and serve as pinning centers [26, 27]. Secondary phases also can affect domain wall motion and increase the coercivity, for example, Fe_3C in steel [28], iron oxide in iron [29] and the $SmCo_5$ cellular structure in $Sm(Co,Fe,Cu,Zr)_7$ magnets [30]. In most cases, the second phase can either result in lower domain wall energy when the domain wall intersects it or serve as a barrier for further propagation of the reversed domains.

2.1.5 Magnetization processes

Magnetization reversal processes are very important in understanding materials' magnetic behavior and in designing magnetic materials with desired hysteresis [31]. One of the manifestations of the magnetization reversal behavior is the initial magnetization curves [32, 33]. In a material with multidomains, the initial magnetization process is fundamentally the elimination of domain walls by domain wall motion and can be utilized to discern the nucleation and pinning behavior. For example, in a nucleation-controlled magnet where the process is controlled by the formation of reversed domains, saturation is reached quickly at a field much lower than the coercive field, shown in mode 1 in Fig. 2.8. The domain walls can be easily moved and are not subject to any barriers or pinning in the material.

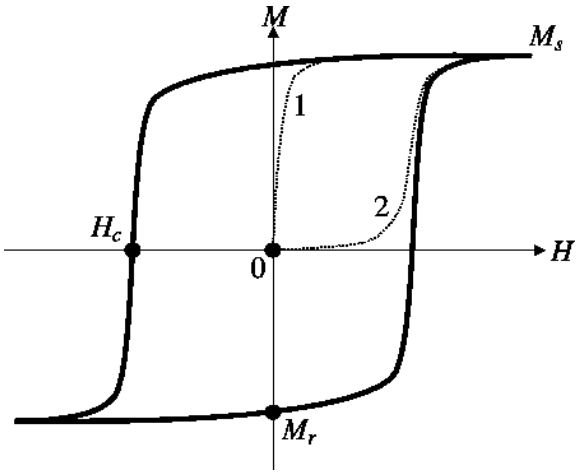

Fig. 2.8 Schematic illustration of the initial magnetization curves for (1) nucleation and (2) pinning

In a pinning-controlled magnet, an applied field close to the coercive field is necessary to reach saturation magnetization. In this case, domain wall energies being different across the material results in difficulties of domain wall motion (Fig. 2.9). Regions with higher domain wall energies act as barriers of domain wall motion, whereas regions with lower domain wall energies serve as pinning sites for domain walls [34]. In some materials, both nucleation and pinning mechanisms will be present resulting in a curve between line 1 and line 2 in Fig. 2.8.

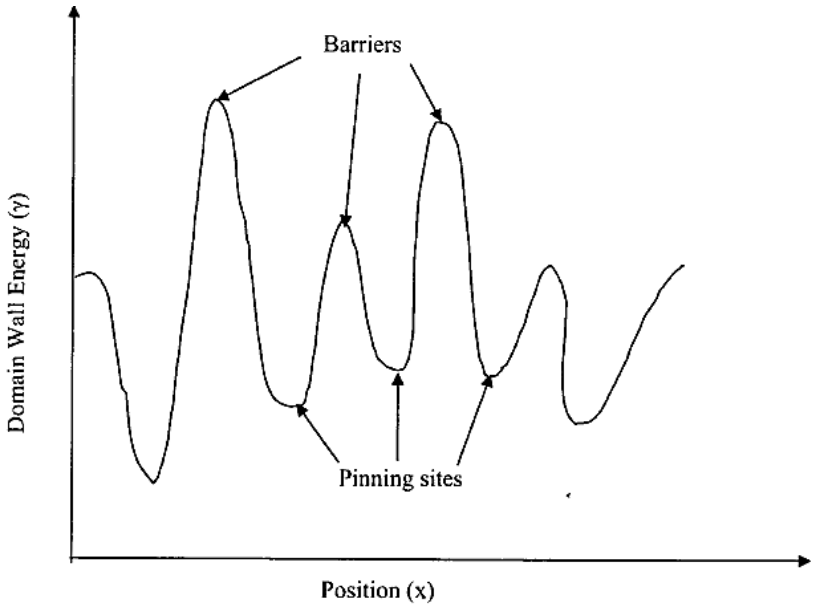

Fig. 2.9 The domain wall energy as a function of position in a magnetic material showing barriers and pinning sites for domain wall motion [16]

2.2 Microstructure features and magnetic properties

Microstructure, in its original sense, means the structure inside a material that could be observed with the aid of a microscope. Microstructural features can include grain size, texture, phase component and different defect structures including grain boundaries or interfaces. As with any structural or functional properties, different microstructural features can play various roles in the extrinsic magnetic properties. Here the literature review will mainly focus on bulk hard magnetic materials, as are related to the dissertation.

(1) Grain size: in soft magnetic materials, it is well established that different magnetic materials with different grain sizes exhibit coercivities which vary several orders of magnitude, shown in Fig. 2.10 (a). In nitrided SmFe hard magnets, certain trend for

coericivty is also observed as a function of grain size (Fig. 2.10 (b)). Generally speaking, in the single domain regime, the intergranular interaction increases as the grain size decreases, which decreases the coercivity; in the multi-domains regime, as the grain size increases, there are more domains within the grain, which facilitates the domain wall motion hence reduces the coercivity. Similar examples can also be found in other hard magnets including NdFeB [35], $SmCo_5$ [36] and various nanocomposite magnets [37, 38].

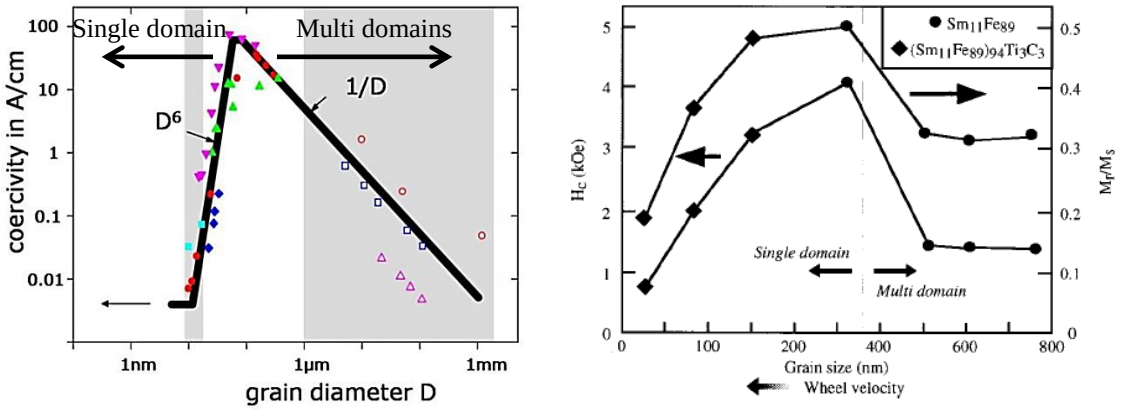

(a) (b)

Fig. 2.10 Grain size effect on coercivity in (a) soft magnetic materials (different colors represent different soft magnetic materials) [39] and (b) nitrided SmFe hard magnets [40]

(2) Phase component: Commercial NdFeB magnets are composed of the magnetic phase 2:14:1 and a Nd-rich grain boundary phase which increases the coercivity of the magnets [41]; in commercial $Sm(CoZrFeZr)_7$ magnets, the $SmCo_5$ phase in the grain boundary with a larger anisotropy field provides a high pinning field which resists the magnetization reversal [42]. Co soft precipitates significantly increase the remanence

ratio in SmCoNbC system [43]. The amorphous phase, which usually induces desirable properties in soft magnets, also showed its unique contribution in hard magnets [44]. Different configurations can be found in Fig. 2.11.

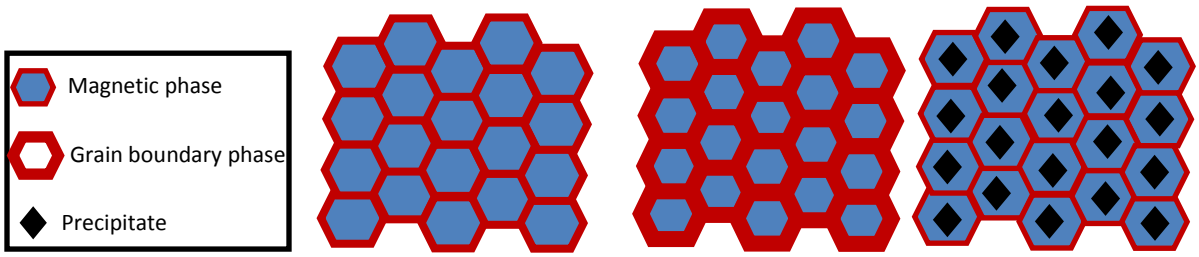

(a) NdFeB + Nd-rich phase (b) Sm_2Co_{17}+$SmCo_5$ (c) $SmCo_7$+Co

Fig. 2.11 Schematic illustration of magnetic materials with different phase components: (a) single magnetic phase; magnetic composites (b) grain boundary and (c) magnetic precipitates Co

(3) Phase configuration and distribution: in magnetic nanocomposites, the configuration and microstructural scale play pronounced roles in shaping the magnetic hysteresis loop [45]. Different features can result in either decoupled or exchanged magnetic behavior, shown in Fig. 2.12. Here microstructural engineering at a nanoscale become extremely important [46].

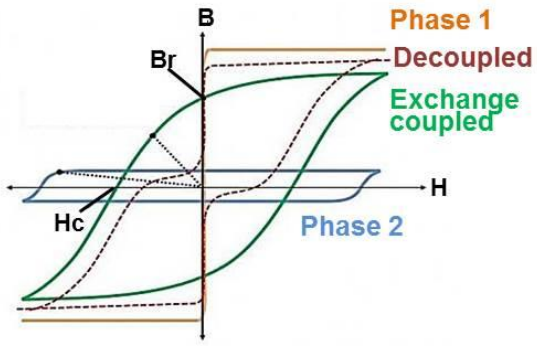

Fig. 2.12 Magnetic behavior in multiphase configurations

(4) Texture: in the multiple-phase configuration, the crystallographic alignment between the phases will result in different energy product values in permanent magnets. Generally speaking, the material with a random alignment between phases only accomplishes a quarter of that with full alignment (following the formula $BH|_{max} \sim M_s^2/4$).

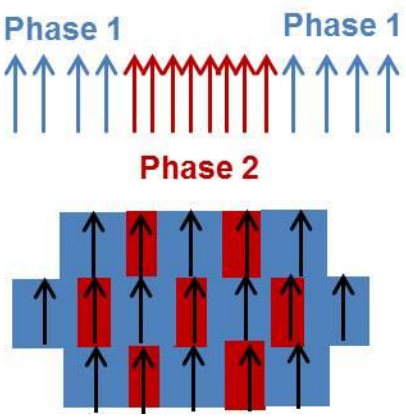

Fig. 2.13 Crystallographic alignment of multiple phases

(5) Other defects: defects such as atomic disorder [47, 48] or twin boundaries [27] also affect the magnetic properties, usually by providing more pinning centers, as discussed in section 2.1.4.

References

[1] J. William D. Callister, John Wiley & Sons, (2007) W25, W27-W29, W34.

[2] B.D. Cullity, C.D. Graham, Wiley IEEE publishing, (2009) 130-132, 204, 102.

[3] J.C. Slater, Phys. Rev., 49 (1936) 537.

[4] C. Zener, Phys. Rev., 81 (1951) 440.

[5] R. Skomski, J.M.D. Coey, Bristol UK and Philadelphia USA, (1999) 177.

[6] X. Rui, dissertation, Crystal structure, microstructure and magnetic properties of inert gas condensed iron-platinum alloys, 2007.

[7] H. Williams, R. Bozorth, W. Shockley, Phys. Rev., 75 (1949) 155.

[8] R. Skomski, Simple models of magnetism, Oxford University Press Oxford, 2008.

[9] http://www.irm.umn.edu/hg2m/hg2m_d/hg2m_d.html.

[10] R. Skomski, J. Phys. Condens. Matter, 15 (2003) R841.

[11] H. Kronmüller, Phys. Status Solidi B, 144 (1987) 385-396.

[12] D. Goll, M. Seeger, H. Kronmüller, J. Magn. Magn. Mater., 185 (1998) 49-60.

[13] J.B. Goodenough, Phys. Rev., 95 (1954) 917-932.

[14] A. Deryagin, Le J. Phys. Colloq., 40 (1979) C5-165-C165-170.

[15] R. Ramesh, J. Appl. Phys., 68 (1990) 5767-5771.

[16] S. Aich, dissertation, Crystal structure, microstructure and magnetic properties of rapidly solidified samarium-cobalt based alloys (2005).

[17] H. Kronmüller, Microstructure and Micromagnetism, in: magnetism and magnetic materials—1972: Eighteenth Annual Conference, AIP Publishing, 1973, pp. 1006-1025.

[18] H. Kronmüller, H. Hilzinger, J. Magn. Magn. Mater., 2 (1976) 3-10.

[19] H. Hilzinger, H. Kronmüller, J. Magn. Magn. Mater., 2 (1976) 11-17.

[20] H. Kronmüller, H. Hilzinger, Int. J. Magn, 5 (1973) 27.

[21] D. Hull, D.J. Bacon, Introduction to dislocations, Pergamon Press Oxford, 1984.

[22] A. Young, J. Jakubovics, J. Phys. F: Met. Phys., 5 (1975) 1866.

[23] M. Hong, K. Hono, M. Watanabe, J. Appl. Phys., 84 (1998) 4403-4409.

[24] X. Chen, P. Gaunt, J. Appl. Phys., 67 (1990) 2540-2543.

[25] D. Hoydick, E. Palmiere, W. Soffa, Scr. Mater., 36 (1997) 151-156.

[26] B. Zhang, W. Soffa, Scr. Metall. et Mater., 30 (1994) 683-688.

[27] T. Klemmer, D. Hoydick, H. Okumura, B. Zhang, W. Soffa, Scr. Metall. et Mater., 33 (1995) 1793-1805.

[28] M. Kersten, Z. Phys, 44 (1943) 63.

[29] J. Kallor, D.I. Paul, A. Tobin, J. Appl. Phys., 37 (1966) 4979-4986.

[30] A. Yan, A. Bollero, K.H. Müller, O. Gutfleisch, J. Appl. Phys., 91 (2002) 8825-8827.

[31] J. Livingston, J. Appl. Phys., 52 (1981) 2544-2548.

[32] X.C. Kou, W.J. Qiang, H. Kronmüller, L. Schultz, J. Appl. Phys., 74 (1993) 6791-6797.

[33] M. Grönefeld, H. Kronmüller, J. Magn. Magn. Mater., 88 (1990) L267-L274.

[34] D.A. Huse, C.L. Henley, Phys. Rev. Lett., 54 (1985) 2708.

[35] T. Sasaki, T. Ohkubo, K. Hono, Y. Une, M. Sagawa, Ultramicroscopy, 132 (2013) 222-226.

[36] W. Li, H. Sepehri-Amin, L. Zheng, B. Cui, A. Gabay, K. Hono, W. Huang, C. Ni, G. Hadjipanayis, Acta Mater, (2012).

[37] C. Rong, Y. Zhang, N. Poudyal, X. Xiong, M.J. Kramer, J.P. Liu, Appl. Phys. Lett., 96 (2010) 102513.

[38] X. Xiong, C. Rong, S. Rubanov, Y. Zhang, J. Liu, J. Magn. Magn. Mater., 323 (2011) 2855-2858.

[39] G. Herzer, IEEE Trans. Magn., 26 (1990) 1397-1402.

[40] J. Shield, D. Branagan, C. Li, R. McCallum, J. Appl. Phys., 83 (1998) 5564-5566.

[41] T. Woodcock, Y. Zhang, G. Hrkac, G. Ciuta, N. Dempsey, T. Schrefl, O. Gutfleisch, D. Givord, Scr. Mater., 67 (2012) 536-541.

[42] O. Gutfleisch, K.-H. Müller, K. Khlopkov, M. Wolf, A. Yan, R. Schäfer, T. Gemming, L. Schultz, Acta Mater., 54 (2006) 997-1008.

[43] J. Shield, V. Ravindran, S. Aich, A. Hsiao, L. Lewis, Scr. Mater., 52 (2005) 75-78.

[44] S. Li, B. Gu, H. Bi, Z. Tian, G. Xie, Y. Zhu, Y. Du, J. Appl. Phys., 92 (2002) 7514-7518.

[45] R. Skomski, J. Coey, Phys. Rev. B, 48 (1993) 15812.

[46] O. Gutfleisch, J. Phys. D: Appl. Phys., 33 (2000) R157.

[47] S. Aich, J. Kostogorova, J.E. Shield, J. Appl. Phys., 97 (2005) 10H108.

[48] S. Aich, J. Shield, J. Magn. Magn. Mater., 279 (2004) 76-81.

Chapter 3 Overview of Sm-Co-based magnets

The Sm-Co system offers various alloys or solid solutions with intriguing structural properties; some of the Co-rich alloys draw particular attention by virtue of the desirable magnetic properties for high temperature magnetic applications. Sm-Co magnets, first discovered in the 1960s [1], are also superior due to their thermal stability and excellent corrosion resistance; therefore, they are widely used in microwave tubes, gyroscopes and accelerometers, reaction and momentum wheels to control and stabilize satellites, magnetic bearings, sensors, and actuators [2]. This chapter will firstly present the structural properties of some Co-rich Sm-Co alloys (with atomic percent of Co > 80 %). The magnetic properties as well as the microstructure related to the commercially more relevant alloys will be emphasized including the aspects of alloy optimization and processing techniques. The magnetic properties of some less-common alloys in the Sm-Co system will also be introduced. This chapter will conclude with a brief introduction of one of the derivatives of $SmCo_5$—$SmCo_4B$.

3.1 Structural aspects of Sm-Co alloys

Co-rich Sm-Co alloys with superior high temperature magnetic properties include several compounds, namely $SmCo_5$, Sm_2Co_{17} and $SmCo_7$. Here only $SmCo_5$ and Sm_2Co_{17} are equilibrium phases, as shown in the equilibrium phase diagram in Fig.3.1. It also can be seen that both Sm_2Co_{17} and $SmCo_5$ have a relatively large homogeneity region (i.e. they are not line compounds). Their crystal structure data can be found in Table 3.1. Note that the composition Sm_2Co_{17} exists in two polytypes—the high temperature hexagonal structure with a space group of $P6_3mmc$ and the lower temperature rhombohedral

structure with a space group of $R\bar{3}m$. The phase transformation temperature boundary between the two phases under equilibrium conditions is ~ 1300 ºC [3]. One can distinguish the two structures based on the stacking sequence of the mixed SmCo planes, with the hexagonal structure being ABABAB… and the rhombohedral structure being ABCABC…, both of which are shown in Fig. 3.2. Sm_2Co_{17} and $SmCo_5$ are closely related to each other. The rhombohedral Sm_2Co_{17} structure can be derived from the hexagonal $SmCo_5$ structure by an ordered substitution of a dumbbell of Co atoms for one-third of the Sm atoms (Fig.3.2). When a random substitution of the Co pairs occurs, a non-equilibrium disordered Co-rich phase of hexagonal $SmCo_7$ (Fig. 3.3) is formed [4]. $SmCo_7$ is a metastable phase and can be stabilized between $SmCo_5$ and Sm_2Co_{17} by rapid solidification or ternary alloying elements [2].

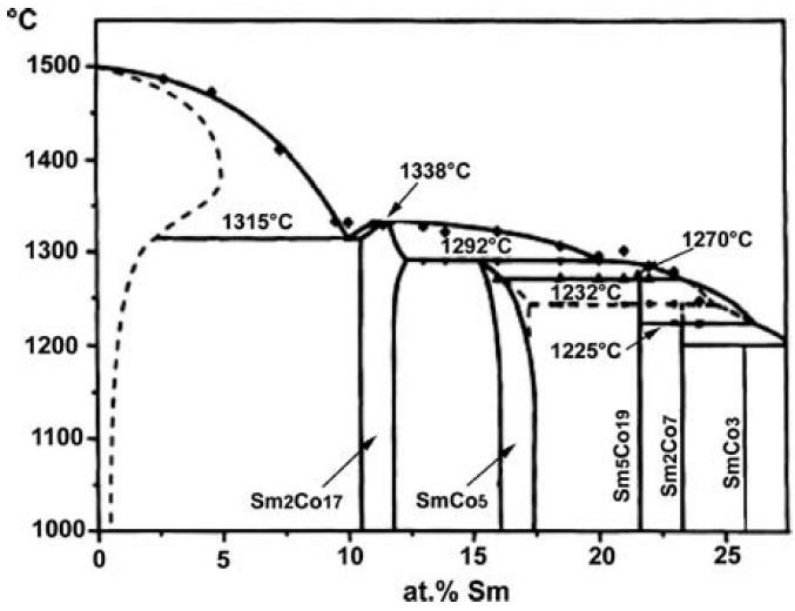

Fig. 3.1 Sm-Co phase diagram in the Co-rich region [5]

Table 3.1 Crystal structure information for some Co-rich Sm-Co compounds [6]

Compound	Space group	Structure type	Lattice constant (Å)
$SmCo_5$	*P6/mmm*	$CaCu_5$	a=5.002 c=3.964
$SmCo_7$	*P6/mmm*	$TbCu_7$	a=4.856 c=4.081
h-Sm_2Co_{17}	*$P6_3mmc$*	Th_2Ni_{17}	a=8.360 c=8.515
r-Sm_2Co_{17}	*$R\bar{3}m$*	Th_2Zn_{17}	a=8.395 c=12.216

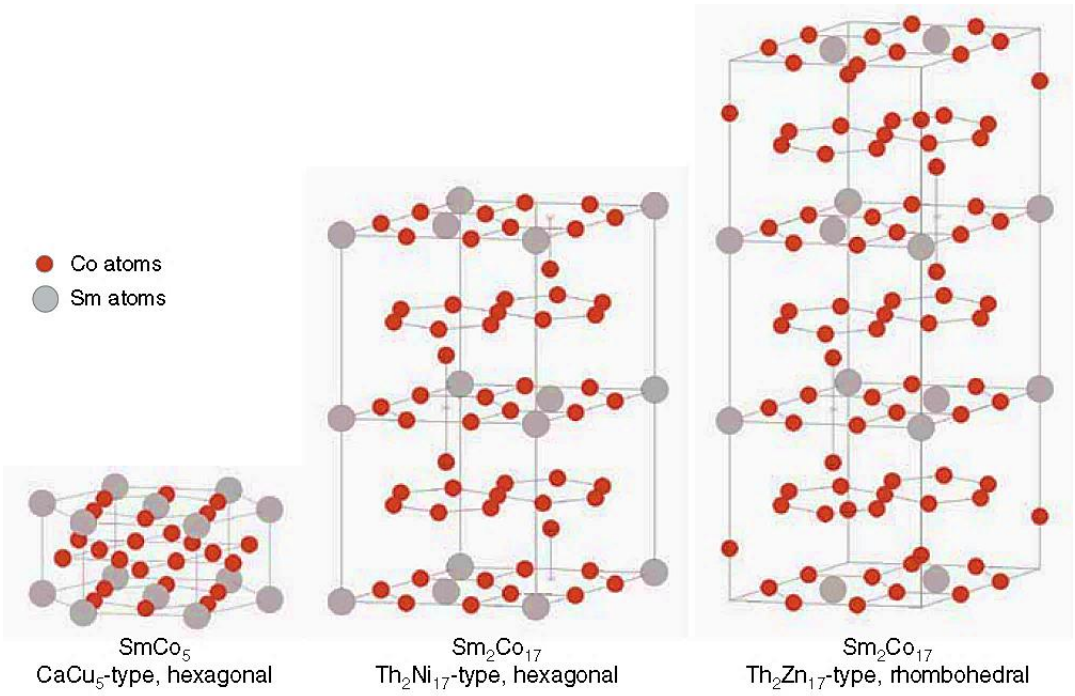

Fig. 3.2 Crystal structures of $SmCo_5$ and Sm_2Co_{17} phases [2]

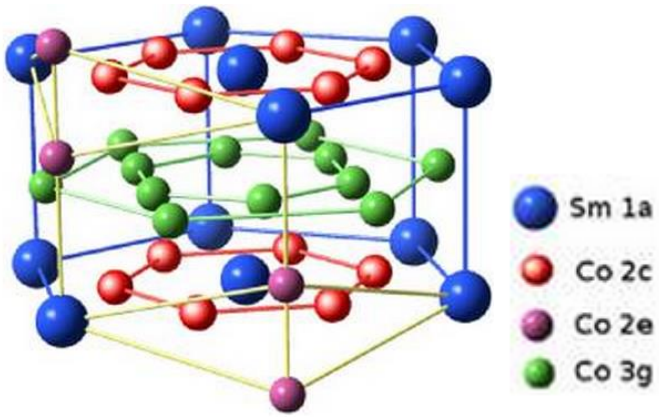

Fig. 3.3 Crystal structure of $SmCo_7$ [7]

3.2 Magnetic aspects of Sm-Co alloys

Some of the Sm-Co alloys show excellent magnetic properties, especially for high temperature applications due to their high Curie temperature and better temperature stability. This section will give an overview of the intrinsic magnetic properties and extrinsic magnetic properties emphasizing the microstructural effects brought by different alloying and processing techniques. Some less-common Sm-Co alloys will also be briefly introduced.

3.2.1 Intrinsic magnetic properties [2]

The intrinsic magnetic properties are governed by magnetic moments and interactions on an atomic scale and are independent of the microstructure of the specific material. In Sm-Co alloys, there are exchange interactions between Sm-Sm, Sm-Co and Co-Co pairs. The strong Co-Co ferromagnetic coupling leads to the large magnetization as well as high Curie temperature. The Sm–Sm exchange coupling occurs indirectly via 4f–5d–5d–4f and is generally very small (since 4f electrons produce magnetic moment

and 4f-4f direct interaction is negligible) compared to the Sm–Co interaction. The Sm-Co proceeds also via an indirect mechanism (4f–5d–3d) in which the strong interatomic direct 5d–3d exchange is transmitted to the 4f electrons via the intraatomic 4f–5d ferromagnetic interaction. The 5d–3d exchange is antiferromagnetic in Sm–Co since the 5d band in Sm is less than half full and the 3d band in Co is more than half full. Qualitatively it can be summarized that as the transition metal spin couples antiparallel to the rare earth spin, the magnetizations of Sm and Co sublattices couple parallel for the light rare earth elements (J = L − S) and antiparallel for the heavy rare earth elements (J = L + S) according to Hund's rule. The orbital magnetic moments in rare earth metals remain unquenched by crystalline fields because the 4f electrons, which produced the magnetic moments, are well inside the atoms and protected from the surrounding atoms. However, the electrostatic crystalline electric field acting on the non-spherical 4f charge distribution favors a certain orientation of its preferred axis and thus also directions of the magnetization. This 3d-4f interaction results in an enormous magnetocrystalline anisotropy. The intrinsic magnetic properties of the commercially relevant phases $SmCo_5$ and Sm_2Co_{17} are listed in Table 3.2.

Table 3.2 Intrinsic magnetic properties of $SmCo_5$ and r-Sm_2Co_{17} [8]

Materials	**T_c (K)**	**M_s (emu/cm^3)**	**K_1 ($10^7 erg/cm^3$)**	**$\|BH\|_{max}$ (MGOe)**
$SmCo_5$	1020	860	17.2	28.8
r-Sm_2Co_{17}	838	970	4.2	36.8

3.2.2 Magnetic aspects of different alloys

(1) $SmCo_5$

$SmCo_5$ has been a research interest both theoretically and experimentally due to its exceptional intrinsic magnetic properties. The large anisotropy field in $SmCo_5$, reflected by the large anisotropy constant of $17\times10^7 erg/cm^3$, was firstly discovered by Karl J. Strnat et al. in 1967 [9]. A milestone energy product as high as 20 MGOe in $SmCo_5$ was achieved through liquid phase sintering in 1969 [10-12]. This production method continues to be used today. It consists of melting and casting the alloy, and thencrushing and grinding the particles to sub-10 μm. The powder then is aligned in a magnetic field and compressed in a die, which is then sintered at a temperature above 1000 ºC to form the final product. It is referred to as liquid phase sintering because an excess of Sm is added before compaction to facilitate the melting at the sintering temperature which helps attain high density. Note that particle size of the powder remains the same before and after compaction, which is an order of magnitude larger than the calculated size of the single-domain particles [12].

One of the unusual and useful properties is that it can be initially magnetized with a field much smaller than its intrinsic coercive field, shown in Fig 3.4. This easy magnetization but difficult demagnetization is a result of nucleation-controlled behavior—the virgin magnets have grains with domain walls that can move relatively easily in the presence of a magnetic field; once the domain walls are driven out, demagnetization requires nucleation of new reverse domains which needs a large nucleation field resulting in a high coercivity.

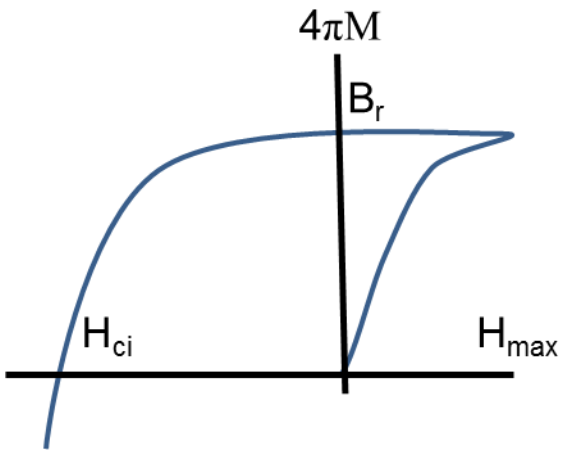

Fig. 3.4 Schematic illustration of magnetization and demagnetization curves for $SmCo_5$

Research interests regarding $SmCo_5$ magnets mainly focus on further optimizing the cost-effectiveness as well as the magnetic properties of $SmCo_5$. Different alloying and processing techniques have been attempted to solve these issues. Early efforts substituted Co with other elements such as Ni [13], Al [14], Sn [15, 16] and Cu [17-19]. Hydrogenation of $SmCo_5$ was attempted in order to improve its magnetic properties, which showed little major promise [20, 21]. Recent efforts have been focused on different processing techniques such as melt-spinning [17, 18], chemical synthesis [22, 23] and plastic deformation with [24, 25] or without [26, 27] surfactants to improve the magnetic behavior. Hot compaction [28] and spark plasma sintering [29] have been tried to produce anisotropic bulk $SmCo_5$ magnets. Due to $SmCo_5$'s superior hard magnetic properties, it is often used as the hard phase in an exchange coupled nanocomposite [30-33].

According to Buschow's reports [34, 35], the $SmCo_5$ system is unstable and tends to decompose at a temperature above 800 ºC. This, to some degree, diverted part of the research interest towards the more Co-rich Sm_2Co_{17} regime.

(2) Sm_2Co_{17}

As described in section 3.1, Sm_2Co_{17} is derived from $SmCo_5$ by an ordered substitution of Co dumbbell pairs for one-third of the Sm atoms. Here the discussion will be focused on the rhombohedral type 2:17 structure rather than the hexagonal mainly because r-Sm_2Co_{17} is used in the commercial magnets. Compared to $SmCo_5$, the r-Sm_2Co_{17} has a higher Curie temperature as well as a larger maximum energy product (Table 3.2), since $(BH)_{max}$ is proportional to the saturation magnetization. However, due to the dumbbell Co substitution for Sm atoms, the anisotropy in Sm_2Co_{17} is reduced significantly. Efforts have been made to increase the intrinsic coericvity by controlling the microstructure. The currently commercial r-Sm_2Co_{17} type sintered magnets usually have a composition of $Sm(Co,Fe,Cu,Zr)_{7.5}$, which is a precipitation-pinning hardened magnet obtained after a typical complex heat treatment regime shown in Fig. 3.5. The optimum microstructure (Fig. 3.6) is a cellular structure with r-Sm_2Co_{17} interiors (typically with a diameter of 100 nm) and $SmCo_5$ cell boundaries (with a thickness of 5-10 nm) rich in Cu content. Here Cu is used to tune the intrinsic magnetic properties of the $SmCo_5$ phase [36]. The majority r-Sm_2Co_{17} phase shows boundaries of coherent twins in the basal plane [37]. The cell boundary phase is coherent with the cell interior [38] since the two structures emerge from the same solid solution. A platelet phase (also referred as the lamellar or Z phase) rich in Zr also exists additionally parallel to the r-Sm_2Co_{17} basal phase (Fig. 3.6). The Z-phase, with the lattice structure unconfirmed, extends over many

r-Sm_2Co_{17} cells with a thickness of 1~3 nm [39]. The Z-phase is considered to stabilize the cellular structure and to provide diffusion paths for Cu, Fe and Co, thereby modifying phase-ordering kinetics [40].

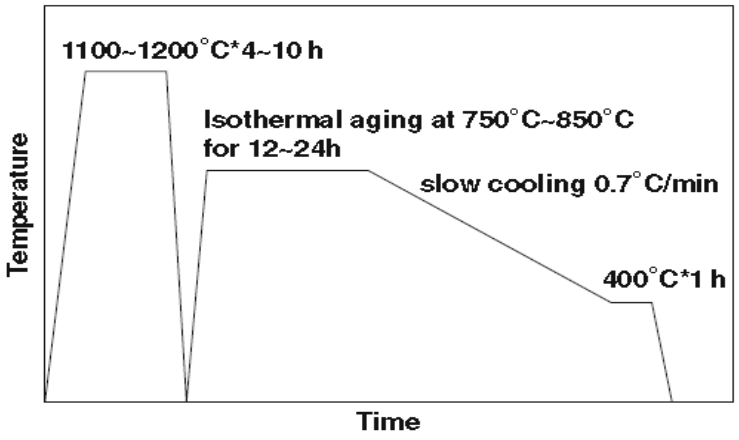

Fig. 3.5 A typical heat treatment procedure for the Sm_2Co_{17} magnets [2]

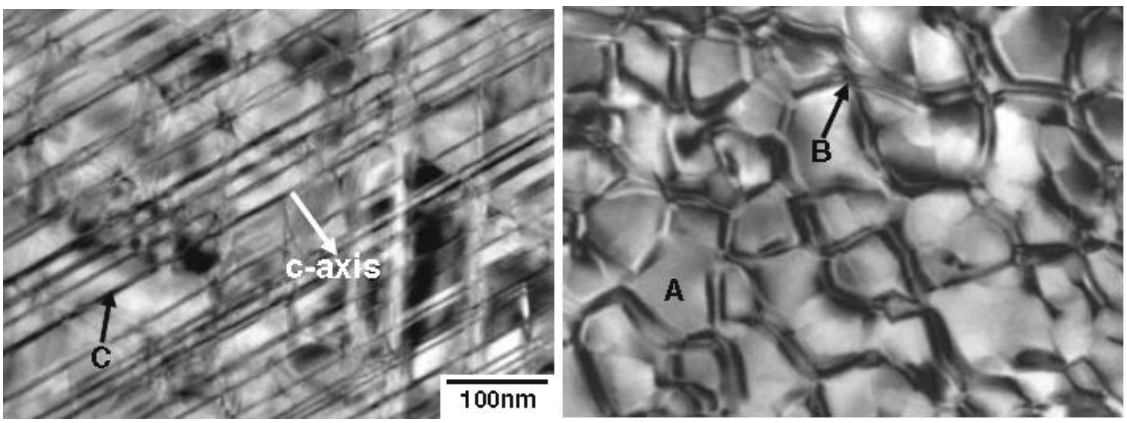

Fig. 3.6 Representative TEM bright field images of a $Sm(Co_{bal}Fe_wCu_xZr_y)_z$-sintered magnet with the nominal c-axis of the r-Sm_2Co_{17} main phase parallel (left) and perpendicular (right) to the imaging plane (A indicates the r-Sm_2Co_{17} type, B the $SmCo_5$ type cell boundary, and C the Z-phases) [41]

The heat treatment at ~ 1200 ºC creates a homogenized solid solution with the $SmCo_7$ type structure [42]. After quenching, the material consists of the supersaturated

$SmCo_7$ phase with partial r-Sm_2Co_{17} order [42]. The isothermal aging at a temperature ~ 850 °C provides necessary grain growth and the diffusion of Sm atoms, resulting in the cellular structure. The slow quenching process at a lower temperature (~ 400 °C) facilitates the redistribution of transition metals which is fundamental in promoting the resultant intrinsic coercivity [43]. It is thought that r-Sm_2Co_{17} forms via nucleation and growth from the $SmCo_7$ structure. Since the solubility of Cu in r-Sm_2Co_{17} at 850 ºC is only 4 at.% [44], his induces enrichment of Cu and Sm in the cell boundary

The $Sm(Co_{bal}Fe_wCu_xZr_y)_z$ magnets represent a complicated system with a large variety of heat treatment and compositional parameters. In order to fine tune the microstructure and microchemistry through the adjustment of those parameters, research has focused on systematically studying the effects of each alloying and processing parameter on the magnetic properties, especially at elevated temperatures [45, 46]. Subtle changes in microchemistry result in changes in the domain wall energy differences between the cell boundary phase and the cell interior, since the domain wall energy differences depend on the wall position as well as the Cu content gradient across the cell boundaries. Generally speaking, coercivity is determined by the difference in the domain wall energies [47] in this pinning controlled magnet. When the domain wall energy $\gamma = 4(AK_1)^{1/2}$ (*A* represents the exchange constant) of $SmCo_5$ is larger than that of r-Sm_2Co_{17}, the domain walls will not be able to enter $SmCo_5$ region, resulting in repulsive pinning. Attractive pinning ensues when the domain walls are trapped in the $SmCo_5$ region when the domain wall energy of r-Sm_2Co_{17} is large [48].

Because of the complexity of designing the optimal magnetic properties in the Sm_2Co_{17} system due to the variety of parameters related to both composition and heat

treatment procedure, there is a strong interest in developing desirable microstructures with fewer variables in the Co-rich Sm-Co system. Extensive research is aimed at designing $Sm(Co,M)_7$ nanoscale magnets.

(3) $SmCo_7$

The $SmCo_7$ phase possesses a disordered $TbCu_7$ type structure at room temperature [49]; it can be derived from a random substitution of Co-dumbbell pair for Sm atoms in the $SmCo_5$ structure. The $SmCo_7$ phase can be obtained by non-equilibrium processing such as melt-spinning [50] and mechanical alloying [51]. It has been reported that $Sm_2(Co, Mn)_{17}$ with the $TbCu_7$ structure exhibits an anisotropy of 105–140 kOe, which is 1.2–1.4 times larger than that of $Sm_2(Co, Mn)_{17}$ with the Th_2Zn_{17} structure [50]. In addition, this structure offers a lower intrinsic coercivity temperature coefficient (β = 0.11% /K) [52]. These two attributes make $SmCo_7$ attractive in high temperature magnetic applications.

To the author's best knowledge, $SmCo_7$ structure is so far mainly synthesized by two approaches: (1) casting with stabilizing agent(s), and (2) ribbons produced by melt-spinning.

When using conventional casting techniques, a third stabilizing agent during synthesis appears to be crucial in forming the disordered $SmCo_7$ structure [53, 54]. For example, Zr, Ti and Cu were found to stabilize the $SmCo_7$ structure as well as bringing in interesting magnetic properties. Specifically, in $SmCo_{6.7}Zr_{0.3}$, it is calculated that the anisotropy constant is increased by 68% compared to that of the pure $SmCo_7$ composition [55], which is also experimentally confirmed [54]. Similarly, in Ti-substituted $SmCo_{7-x}Ti_x$ [56], the anisotropy field reaches a maximum of 175 kOe at x = 0.28. It is also found

that the $SmCo_7$ phase can only stabilized when x (in $SmCo_{7-x}M_x$) < 0.4 for Zr [54] and Ti [56]. Interestingly, Cu substitutions in $SmCo_{7-x}Cu_x$ exhibited a higher solid solubility of x = 0.8 in the 1:7 phase [57, 58]. Generally speaking, the doping elements will substitute for Co atoms in the structure, changing the crystal field interaction, which increases the anistropy field of the 1:7 phase [59, 60]. An extensive discussion of the effect of different alloying on the atomic structure and magnetic properties of the $SmCo_7$ phase can be found in Chapter 6.

The discussion above focused on the effect of doping on the intrinsic properties of the compounds. Extrinsic properties, affected by microstructure, can also play an important role in the magnetic properties. Non-equilibrium processing induces nanostructuring which is beneficial in controlling the microstructure of the magnetic materials. The $SmCo_7$ phase has been successfully stabilized using melt spinning [50] and mechanical milling [61]. The advantage of non-equilibrium processing is that it has a better control of the grain scale. To assist the nanostructuring process, C additions during synthesis proved effective in further refining the grain size by either providing more nucleation sites or forming carbides which inhibit grain growth [62-65].

Recently, Zhang et al. [66, 67] successfully synthesized nanocrystalline $SmCo_7$ in bulk form adopting a route that combines induction melting, ball milling and spark plasma sintering. They found that nanoscale $SmCo_7$ phase can remain stable from room temperature to 600 ºC, which is absent in coarse-grained polycrystalline $SmCo_7$.

Besides the aforementioned Sm-Co alloys, the structural and magnetic properties of the less-common $SmCo_{9.8}$ [68, 69], Sm_5Co_{19} [70] and $SmCo_3$ [71] have also been reported. Zhexu Zhang et al [68] found that the non-equilibrium $SmCo_{9.8}$ phase only

exists stably when the grain size is less that 10 nm while W.F. Liu et al. [69] were able to form this phase by alloying with a small amount of V. Zhang et al. [70] also proved that nanoscaling increased the stability of Sm_5Co_{19} phase. Nanostructuring has proved to increase the cell volume of $SmCo_3$ structure compared to that of the coarse-grained structure [71]. The three compounds above showed intrinsically high anisotropy and high Curie temperatures, which make them potentially attractive for high temperature permanent magnets applications.

3.3 A derivative of $SmCo_5$—$SmCo_4B$

The complex procedures in the aforementioned commercial Sm-Co magnets also led to the research efforts to exploit Sm-Co based intermetallics with other structures. $SmCo_4B$ (Fig 3.7), a pseudo-ternary compound with a hexagonal crystal structure, is derived from the $SmCo_5$ structure by an ordered substitution of B atoms for Co atoms in every second layer [72]. This substitution almost doubles the anisotropy constant in the system, from 17.2 MJ/m^3 for $SmCo_5$ to 30.2 MJ/m^3 for $SmCo_4B$ [8]. However, B substitution also resulted in diluted magnetization which is undesirable for permanent magnet applications. Alloying with Fe can potentially increase the magnetization.

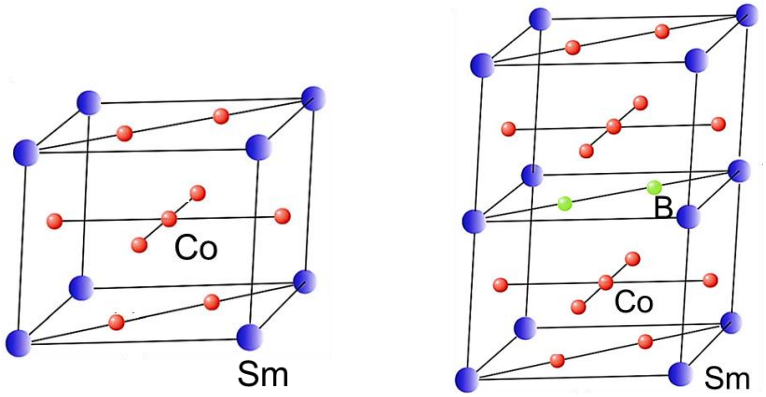

Fig. 3.7 Crystal structures of $SmCo_5$ (left) and $SmCo_4B$ (right) [73]

The current research reports microstructural development in both $Sm(Co,M)_7$ and $SmCo_4B$ systems. In both cases, nanostructuring was achieved by rapid solidification via melt-spinning. In the former system, we focused on alloying to stabilize the 1:7 phase without bringing harm to the magnetic properties. In the latter, Fe substitutions and different heat treatment procedures were performed to improve the magnetic properties.

References

[1] A. Nowick, Rare earth permanent magnets, Elsevier, 2012.

[2] O. Gutfleisch, High-temperature samarium cobalt permanent magnets, in: Nanoscale Magnetic Materials and Applications, Springer, 2009, pp. 337-372.

[3] T.B. Massalski, H. Okamoto, P. Subramanian, L. Kacprzak, Binary alloy phase diagrams, ASM international, 1990.

[4] Y. Khan, Acta Crystallogr., Sect. B, 29 (1973) 2502-2507.

[5] L. Cataldo, A. Lefevre, F. Ducret, M.-T. Cohen-Adad, C. Allibert, N. Valignat, J. Alloys and Compd, 241 (1996) 216-223.

[6] K. Buschow, A. Van der Goot, J. Less-Common Met., 14 (1968) 323-328.

[7] http://www.mpie.de/index.php?id=3356.

[8] J.M. Coey, Magnetism and magnetic materials, Cambridge University Press, 2010.

[9] K. Strnat, G. Hoffer, J. Olson, W. Ostertag, J.J. Becker, J. Appl. Phys., 38 (1967) 1001-1002.

[10] F.F. Westendorp, K.H.J. Buschow, Solid State Commun., 7 (1969) 639-640.

[11] S. Foner, E.J. McNiff, D.L. Martin, M.G. Benz, Appl. Phys. Lett., 20 (1972) 447-449.

[12] K.H.J. Buschow, P.A. Naastepad, F.F. Westendorp, J. Appl. Phys., 40 (1969) 4029-4032.

[13] H. Oesterreicher, F.T. Parker, M. Misroch, Phys. Rev. B, 18 (1978) 480-485.

[14] A. Laslo, C. Colin, O. Isnard, M. Guillot, J. Appl. Phys., 107 (2010) 09A732-709A732-733.

[15] A. Kündig, R. Gopalan, T. Ohkubo, K. Hono, Scr. Mater., 54 (2006) 2047-2051.

[16] H. Zaigham, F.A. Khalid, J. Mater. Eng. Perform., 20 (2011) 1304-1309.

[17] W.-y. Zhang, X.-d. Zhang, Y.-c. Yang, B.-g. Shen, J. Alloys Compd., 353 (2003) 274-277.

[18] A.-r. Yan, W.-y. Zhang, H.-w. Zhang, B.-g. Shen, J. Appl. Phys., 88 (2000) 2787-2790.

[19] B. Barbara, M. Uehara, IEEE Trans. Magn., 12 (1976) 997-999.

[20] M. Kubis, A. Handstein, B. Gebel, O. Gutfleisch, K.-H. Muller, L. Schultz, J. Appl. Phys., 85 (1999) 5666-5668.

[21] H. Zijlstra, F. Westendorp, Solid State Commun., 7 (1969) 857-859.

[22] Y. Hou, Z. Xu, S. Peng, C. Rong, J.P. Liu, S. Sun, Adv. Mater., 19 (2007) 3349-3352.

[23] C. Chinnasamy, J. Huang, L. Lewis, B. Latha, C. Vittoria, V. Harris, Appl. Phys. lett., 93 (2008) 032505.

[24] L. Zheng, B. Cui, G.C. Hadjipanayis, Acta Mater, 59 (2011) 6772-6782.

[25] C. Chen, S. Knutson, Y. Shen, R. Wheeler, J. Horwath, P. Barnes, Appl. Phys. lett., 99 (2011) 012504.

[26] I. Al-Omari, R. Skomski, R. Thomas, D. Leslie-Pelecky, D. Sellmyer, IEEE Trans. Magn., 37 (2001) 2534-2536.

[27] D.L. Leslie-Pelecky, R.L. Schalek, Phys. Rev. B, 59 (1999) 457.

[28] W. Li, H. Sepehri-Amin, L. Zheng, B. Cui, A. Gabay, K. Hono, W. Huang, C. Ni, G. Hadjipanayis, Acta Mater., (2012).

[29] M. Yue, J. Zuo, W. Liu, W. Lv, D. Zhang, J. Zhang, Z. Guo, W. Li, J. Appl. Phys., 109 (2011) 07A711.

[30] C.-b. Rong, Y. Zhang, M. Kramer, J.P. Liu, Phys. Lett. A, 375 (2011) 1329-1332.

[31] P. Saravanan, R. Gopalan, N.R. Rao, M.M. Raja, V. Chandrasekaran, J. Phys. D: Appl. Phys., 40 (2007) 5021.

[32] L.M. Ortega, J.E. Galindo, J.F. Mancilla, C. Santillan, J.M. Aquino, J. Appl. Phys., 111 (2012) 07B505.

[33] C. Rong, Y. Zhang, N. Poudyal, X. Xiong, M.J. Kramer, J.P. Liu, Appl. Phys. Lett., 96 (2010) 102513-102513-102513.

[34] K.H.J. Buschow, J. Less-Common Met., 29 (1972) 283-288.

[35] K.H.J. Buschow, J. Less-Common Met., 37 (1974) 91-101.

[36] H. Nagel, A.J. Perry, A. Menth, J. Appl. Phys., 47 (1976) 2662-2670.

[37] J. Fidler, J. Magn. Magn. Mater., 30 (1982) 58-70.

[38] J. Livingston, D. Martin, J. Appl. Phys., 48 (2008) 1350-1354.

[39] J.M.D. Coey, Rare-earth iron permanent magnets, Oxford University Press, 1996.

[40] L. Rabenberg, R. Mishra, G. Thomas, J. Appl. Phys., 53 (1982) 2389-2391.

[41] O. Gutfleisch, K.-H. Müller, K. Khlopkov, M. Wolf, A. Yan, R. Schäfer, T. Gemming, L. Schultz, Acta Mater., 54 (2006) 997-1008.

[42] C. Maury, L. Rabenberg, C. Allibert, Phys. Status Solidi A, 140 (1993) 57-72.

[43] X. Jiang, A. Devaraj, B. Balamurugan, J. Cui, J.E. Shield, J. Appl. Phys., 115 (2014) 063902.

[44] A. Perry, J. Less-Common Met., 51 (1977) 153-162.

[45] J. Liu, T. Chui, D. Dimitrov, G. Hadjipanayis, Appl. Phys. Lett., 73 (1998) 3007-3009.

[46] A. Lefévre, L. Cataldo, M.T. Cohen-Adad, B. Mentzen, J. Alloys Compd., 275 (1998) 556-559.

[47] R. Skomski, J. Phys.: Condens. Matter, 15 (2003) R841.

[48] J. Zhou, R. Skomski, C. Chen, G.C. Hadjipanayis, D.J. Sellmyer, Appl. Phys. letters, 77 (2000) 1514-1516.

[49] K. Buschow, A. Van der Goot, Acta Crystallogr., Sect. B, 27 (1971) 1085-1088.

[50] H. Saito, M. Takahashi, T. Wakiyama, G. Kido, H. Nakagawa, J. Magn. Magn. Mater., 82 (1989) 322-326.

[51] J. Yang, O. Mao, Z. Altounian, IEEE Trans. Magn., 32 (1996) 4380-4382.

[52] Y. Guo, W. Li, J. Luo, W. Feng, J. Liang, J. Magn. Magn. Mater., 303 (2006) 367-370.

[53] Y. Guo, W. Feng, W. Li, J. Luo, J. Liang, J. Appl Phys., 101 (2007) 023919.

[54] M. Huang, W. Wallace, M. McHenry, Q. Chen, B. Ma, J. Appl Phys., 83 (1998) 6718.

[55] Y. Chen, C. Hsieh, S. Lo, W. Chang, H. Chang, S. Chiou, H. Ouyang, J. Appl Phys., 109 (2011) 07A748.

[56] J. Zhou, I. Al-Omari, J. Liu, D.J. Sellmyer, J. Appl Phys., 87 (2000) 5299.

[57] I. Al-Omari, Y. Yeshurun, J. Zhou, D. Sellmyer, J. Appl Phys., 87 (2000) 6710-6712.

[58] J. Luo, J. Liang, Y. Guo, Q. Liu, L. Yang, F. Liu, G. Rao, W. Li, J. Phys: Condens. Matter, 15 (2003) 5621.

[59] Y. Guo, W. Feng, W. Li, J. Luo, J. Liang, J. Appl. Phys., 101 (2007) 023919--023917.

[60] J. Luo, J. Liang, Y. Guo, Q. Liu, F. Liu, Y. Zhang, L. Yang, G. Rao, Intermetallics, 13 (2005) 710-716.

[61] C. Jiang, M. Venkatesan, K. Gallagher, J. Coey, J. Magn. Magn. Mater., 236 (2001) 49-55.

[62] S. Aich, J.E. Shield, J. Alloys Compd., 425 (2006) 416-423.

[63] H. Chang, C. Guo, C. Hsieh, W. Chang, J. Phys. Chem. Solids, 73 (2011) 13-17.

[64] H. Chang, S. Huang, C. Chang, C. Chiu, W. Chang, A. Sun, Y. Yao, J. Appl. Phys., 101 (2007) 09K508-509K508-503.

[65] A.-R. Yan, Z.-G. Sun, W.-Y. Zhang, H.-W. Zhang, B.-G. Shen, Appl. Phys. A, 71 (2000) 311-314.

[66] Z. Zhang, X. Song, W. Xu, Acta Mater., 59 (2011) 1808-1817.

[67] Z. Zhang, X. Song, W. Xu, M. Seyring, M. Rettenmayr, Scr. Mater., (2010) 594-597.

[68] Z.-X. Zhang, X.-Y. Song, W.-W. Xu, N.-D. Lu, J. Alloys Compd., 539 (2012) 108-115.

[69] W. Liu, G. Rao, H. Yang, Z. Ouyang, G. Liu, X. Feng, J. Liang, J. Alloys Compd., 361 (2003) 62-65.

[70] Z. Zhang, X. Song, Y. Qiao, W. Xu, J. Zhang, M. Seyring, M. Rettenmayr, Nanoscale, (2013).

[71] N. Lu, X. Song, J. Zhang, Nanotechnology, 21 (2010) 115708.

[72] A. Pedziwiatr, S. Jiang, W. Wallace, E. Burzo, V. Pop, J. Magn. Magn. Mater., 66 (1987) 69-73.

[73] M. Pugaczowa-Michalska, A. Kowalczyk, Intermetallics, 14 (2006) 1448-1451.

Chapter 4 Experimental procedures

This chapter will describe the fundamental mechanisms of all the techniques involved and some basic operating procedures of the specific apparatuses utilized in the sample synthesis and characterization processes.

4.1 Materials synthesis procedures

All samples characterized and investigated were synthesized in the following procedures: **(1)** raw materials were mixed and melted using an arc-melter to form an ingot; **(2)** the ingot was induction melted and rapidly solidified into ribbons in a melt-spinner. Most of the samples also underwent heat treatment at different temperatures. This section introduces the mechanisms, the functions as well as the basic procedures of each procedure.

4.1.1 Arc melting

The raw elemental materials with a 99.99 % or higher purity were weighed (on a precision weighing balance (SARTORIUS) with an error of ± 1 mg) and mixed and loaded onto one of the depressions on the copper hearth in a home-made arc-melter in order to make a homogeneous alloy ingot.

A schematic illustration of the arc-melter setup utilized in this research is shown in Fig. 4.1. The arc-melting method is based on an electric circuit consisting of the following four parts: power supply, a melting electrode, a cooling base and the connecting leads (cables). An electric arc, luminous electrical discharge (mainly consisting of plasma) between two electrodes through ionized gas, is struck between a

tungsten electrode and the copper hearth. The intense heat generated by the electric arc will melt the elements and an alloy ingot is therefore formed. The temperature and luminosity of electric arcs mostly depend on two factors: the type of gas and pressure. When the electric current travels in the gap between the electrodes, it heats the gas around it. By ionizing and changing the chemical composition of the gas, the arc's heat and brightness can be altered [1].

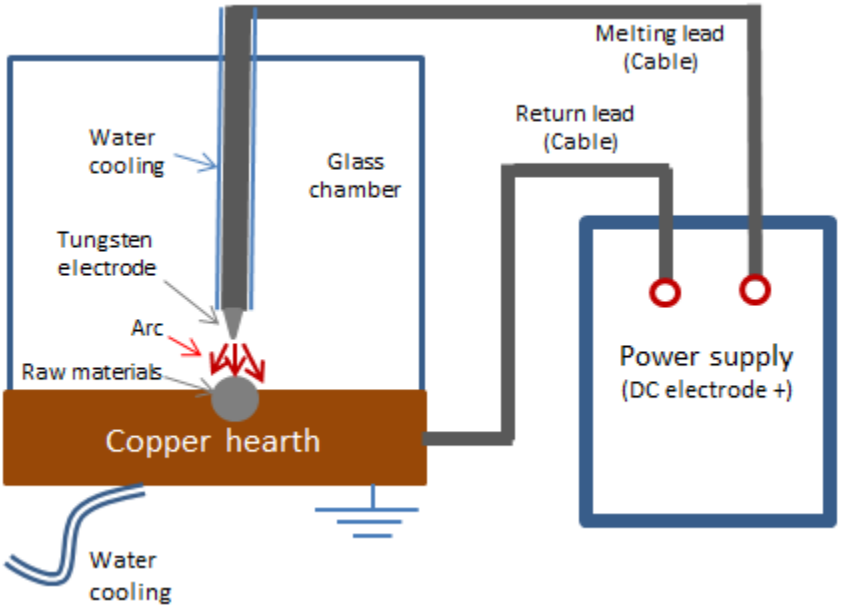

Fig. 4.1 A schematic illustration of an arc-melter

In our lab's setup, the DC power source is supplied by a Synchowave 180 SD (CC, AC/DC squarewave power source) manufactured by Miller Electric. Specifically, the amps output was kept at 180 Amps and the operating mode was kept at TIG position under an electrode positive polarity. A cylindrical glass chamber was used to control the melting environment as well as allowing for visual observation during melting. Cooling water was also present while melting.

If the raw constituents contain elements bearing high vapor pressure or/and light elements, they are put at the bottom covered with heavier elements in order to reduce the evaporation. In this research, an extra 5 wt. % of Sm was added to the sample in order to compensate for Sm loss due to vaporization during melting. The total mass of the sample usually was ~ 5 g. After loading the raw materials onto the finger-shaped depression in the copper hearth and a zirconium piece in a separate depression, the chamber was closed to create an inert atmosphere. The cleanliness of the chamber as well as the O-rings inside is critical for a successful evacuation. A mechanical pump was used for the evacuation and ultra-high purity (UHP) argon was used as the inert gas. The chamber was evacuated to approximately 45 millitorr and flushed with UHP argon at least four times. Eventually, an UHP argon atmosphere was created with a final pressure of – 15 in Hg. A shield is needed to protect the eyes while melting due to extreme brightness. The zirconium ingot was melted first to ensure that the arc melter was operational and an inert atmosphere was present. If the zirconium ingot remains shiny after melting, the atmosphere is inert and is ready to melt the sample. After firstly melting the sample into one ingot, the ingot was then turned over and melted for a second time to ensure homogeneity.

4.1.2 Melt spinning

The alloy ingot was next put in a crucible with an orifice at the bottom, which was then inserted into a copper coil in a melt-spinner obtained from Johanna Otta GmbH in Germany. Melt spinning, short for chill block melt spinning, can result in extended solid solubility, increased chemical homogeneity, refined grain size and formation of

metastable phases. This technique is suitable for producing amorphous or nanocrystalline materials.

Melt spinning was first officially illustrated by Strange and Pim in 1908 [2] while more recent research was initiated by Pond in 1958 [3]. It refers to a process in which a molten alloy jet is first formed and then impinges against a rapidly moving substrate surface which acts both to chill continuously and to transport material away from the melt jet impinging area, resulting in the fabrication of ribbons or tapes [4]. A typical melt spinning apparatus is comprised of a rotating wheel, an induction heater and a crucible with a round nozzle at its bottom, illustrated in Fig 4.2. Here the induction coil is used to heat the materials above its melting temperature and form a liquid. After applying an overpressure on top of the alloy ingot, the liquid will be ejected onto the copper wheel, which serves as an effective heat sink. By adjusting the wheel speed, the size of the nozzle, the overpressure, the distance between the nozzle and the wheel surface, the cooling rate can be adjusted. The typical cooling rate is on the order of 10^6 K/s.

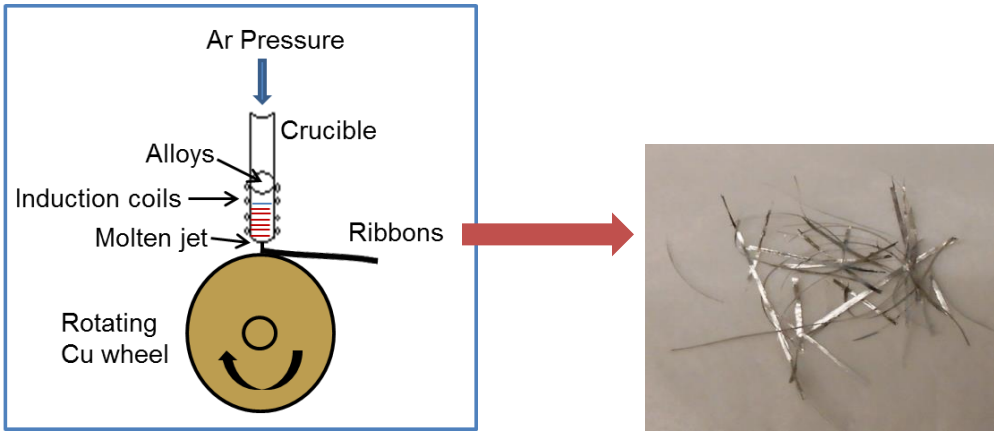

Fig. 4.2 A schematic illustration of a melt-spinner and the resultant ribbons

Melt spinning technique bringing in abovementioned benefits is due to the fact that this technique can provide a unique combination of the thermodynamics and kinetics

in the materials. First of all, the rapid heat extraction results in large undercoolings (representing the difference between the actual nucleation temperature and the equilibrium melting temperature) and leads to solidification under a non-equilibrium condition, which can result in the formation of metastable phases. Additionally, short diffusion distances and formation time can result in a low growth rate, which makes the extended solute solubility and grain refinement possible.

Throughout the projects conducted in this research, the orifice diameter was fixed at 0.5 mm and the distance between the orifice and the copper surface was ~ 1 cm. An inert atmosphere was created in a similar fashion as the one in an arc-melter. The final chamber pressure was kept at ~ 900 mbar and the overpressure applied to the alloy ingot was 0.2 bar. The wheel speed can vary from 5 ~ 60 m/s. Generally speaking, the larger the wheel speed, the smaller the grain scale. The resultant ribbons are usually 20-40 μm thick and 2-3 mm wide (Fig. 4.2).

4.1.3 Heat treatment

Heat treatment, involving heating the materials to a predefined temperature and maintaining for a suitable time followed by cooling, are performed for most of the samples at different temperatures for different holding times. Heat treatment, on one hand, induces faster diffusion of atoms within solid materials by providing the energy needed to break bonds, so that the materials evolve towards their equilibrium state; on the other hand, the thermal energy provided during the heating also accelerates the relief of the internal stress. In addition, the quenching process sometimes can retain a solid solution which is only available at elevated temperatures. Heat treatment can usually crystallize materials in a well-controlled manner and will usually induce grain growth.

The materials (ribbons and ground powder) were first wrapped in tantalum foil and then sealed in a quartz tube with argon atmosphere. The quartz tube was then heat treated in a tube furnace following a specific heat treatment procedure, followed by either water quenching or furnace cooling.

4.2 Characterization aspects

The materials synthesized were subjected to different characterization aspects, including structural, thermal, magnetic and microstructural analysis. This section briefly introduces the fundamentals of each technique.

4.2.1 Structural analysis: X-Ray diffraction (XRD)

X-ray diffraction [5, 6] is a technique capable of providing and identifying the atomic structure of crystalline materials. X-rays are defined as the electromagnetic radiation with wavelength ranging from approximately 10^{-3} to 10 nm, which is comparable to the interatomic distances of materials; therefore they can be used as an important tool in structure determination.

The interference of x-rays with matter is rendered possible due to the crystal structures' periodicity. Atoms arranged in an orderly array in crystals serve as scattering centers of x-rays, re-emitting x-rays at the same wavelength as the incident radiation in all directions. The scattered x-rays are in phase if the orderly arrangement of atoms is in specific directions governed by symmetry and atomic spacings, and out of phase for all other directions, as shown in Fig. 4.3. Here λ represents the wavelength of the incident beam, θ represents the incident angle with respect to the crystal planes and d represents

the atomic spacings. The x-rays scattered that are in phase interfere constructively and form intense beams (diffracted beam), while those that are out of phase interfere destructively and have no diffraction peaks. Based on the position of the diffracted beams, the atomic structure and symmetry can be identified by using Bragg law (Eqn. 4.1).

$$2dsin\theta = n\lambda \quad \textbf{(4.1)}$$

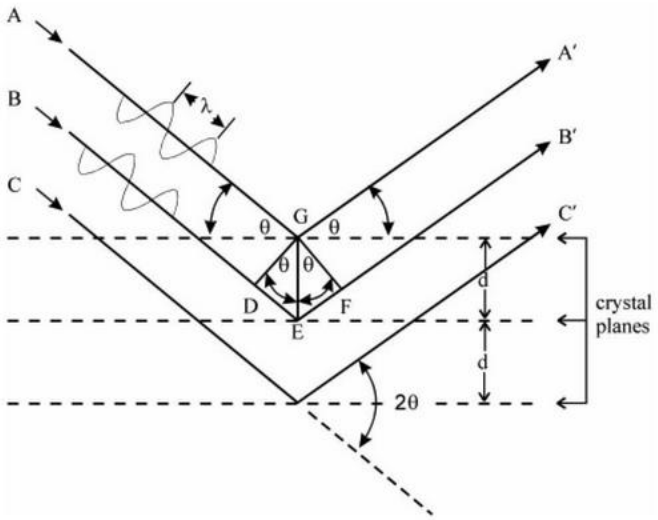

Fig. 4.3 A schematic illustration of XRD by regularly spaced planes of atoms in a crystal [6]

In this research, a Rigaku Multiflex X-ray diffractometer with Cu Kα radiation with λ = 1.5418 Å were used to analyze the powdered samples and the obtained diffractions patterns were compared with x-ray patterns in the International Centre for Diffraction Data (ICDD), a database of powder diffraction patterns; therefore the crystal structure and lattice plane indices can be identified.

One of the advantages of x-ray diffraction is its ability to precisely determine lattice parameters. Usually, for a pure unalloyed phase, it is possible to find reliable

lattice parameters information from the ICDD. However, the changes in lattice parameters induced by doping or alloying in a structure usually should be analyzed on a case-by-case basis. For example, in hexagonal structures, for a specific set of planes with indices of (h, k, l), the d-spacing is related to the crystal lattice parameters *a* and *c* via the following equation:

$$\frac{1}{d^2} = \frac{4}{3}\left(\frac{h^2 + hk + k^2}{a^2}\right) + \frac{l^2}{c^2} \quad \textbf{(4.2)}$$

Here the d-spacing can be obtained from the Bragg law in Eqn. 4.1, and the crystal plane indices can be evaluated by comparing the experimental pattern with one in JCPDS (mainly peak positions and relative intensities). The lattice paramters *a* and *c* of the materials can then be roughly identified by taking into account information from only two peaks. Generally speaking, information from intense non-overlapping peaks is recommended for the lattice parameter determination.

The peak width from the x-ray diffraction patterns can be utilized to determine the grain size of materials. For materials with a nanoscale grain size, due to the non-ideal diffraction conditions, the diffraction peaks broaden significantly when the grain size decreases to less than ~ 100 nm. The grain size is inversely related to the FWHM (full width at half maximum) of an individual peak: the narrower the peak, the larger the grain size. Here we adopted the Scherrer equation [7] (Eqn. 4.3) for the calculation of grain size, where *t* refers to the grain size in nm. *B* refers to the instrumental-corrected FWHM in radians and is defined as $\sqrt{B_0 - B_s}$, where B_0 is the experimental FWHM measured from a peak and B_s is the standard FWHM from a standard Si sample.

$$t = \frac{0.9\lambda}{B\cos\theta} \quad \textbf{(4.3)}$$

X-ray diffraction patterns are also capable of identifying the order-disorder transformations, which occur between Sm_2Co_{17} and $SmCo_7$ structures (both are derivatives of $SmCo_5$). As discussed in Chapter 3, Sm_2Co_{17} is obtained by an ordered substitution of Co dumbbell pairs for one-third of Sm atoms in $SmCo_5$, whereas $SmCo_7$ results from the same substitutions but in a random fashion. As a result, the diffraction patterns of the Sm_2Co_{17} structure shows superlattice peaks emerging from the diffraction of the ordered Co dumbbell atoms, which are absent in the $SmCo_7$ structure. This can be used to distinguish the two structures.

4.2.2 Thermal behavior: Differential Thermal Analysis (DTA)

DTA [8] is a thermoanalytic technique where the material under study and an inert reference are made to undergo identical thermal cycles, while recording any temperature difference between the sample and the reference in a specific atmosphere. Phase changes in the sample, either exothermic or endothermic, can be detected relative to the inert reference. If the sample undergoes a phase transition when the temperature increases, a temperature difference will show up in the thermogram. This is because the heat input will raise the temperature of the reference, but be incorporated as the latent heat of the sample in the phase transition. Thus, a DTA curve provides data on the transformations that have occurred, such as glass transitions, crystallization, melting and phase decompositions. The result is a plot (thermogram) of enthalpy change with respect to temperature or time. Usually, the higher the glass transition temperature, the more stable the glass material is. The area under a DTA crystallization peak (exothermic) is the

enthalpy change and it reflects the relative fraction of the amorphous materials in the sample.

The heart of a DTA measurement system consists of a sample holder and the reference material holder, thermocouples connected to each holder and a furnace (Fig. 4.4). Heating programs can be designed and used to control the measurement. In this research, the DTA is performed using a Perkin-Elmer System 7 with a heating rate of 10 ºC /min under Ar atmosphere. The reference sample is Al_2O_3. For measurement precision, the mass of samples investigated is usually close to 50 mg and the reference material Al_2O_3 will be put on top of the sample to ensure good contact.

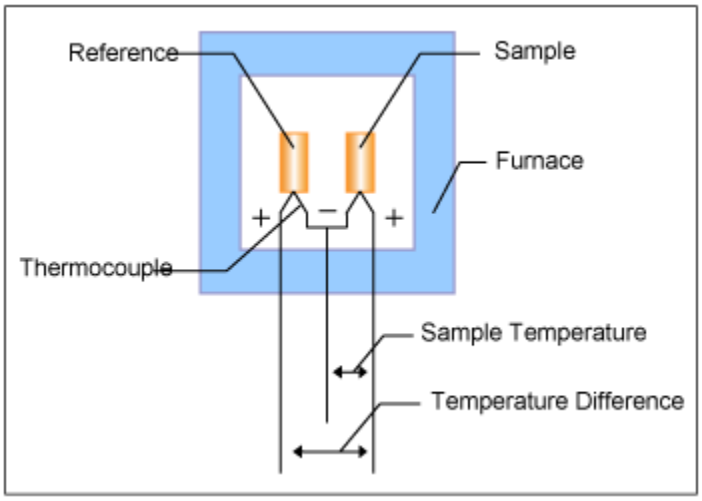

Fig. 4.4 A schematic illustration of a DTA measurement setup [9]

4.2.3 Magnetic characterization: AGFM & SQUID

The magnetic properties of this research, including initial magnetization behavior and hysteresis loops were obtained from either an Alternative Gradient Field Magnetometer (AGFM) or a superconducting quantum interference device (SQUID) magnetometer. The mechanisms of both of them are introduced briefly in this section. In

all measurements, ribbons were first weighed using a precision balance (Sartorius) with a error of 0.001 mg and usually ribbons were cut so that the mass is kept close to 0.2 mg for both AGFM and SQUID measurements. Multiple measurements were performed on different pieces of ribbons produced at the same condition to ensure accuracy. For some measurements, the ribbons were pulse magnetized using a pulse magnetizer of 12.5 T before measurements. The magnetic field was applied parallel to the ribbon plane in all cases so as to minimize the demagnetizing factors.

(1) AGFM

The magnetic properties can be quickly evaluated by the Alternative Gradient Field Magnetometer (AGFM) [10, 11] which allows magnetic measurements on thin samples with low mass. A schematic illustration of an AGFM can be found in Fig. 4.5. Here an alternating field gradient produced by an appropriate coil pair and a fixed dc field will be applied to the sample which is attached to the end of a quartz probe. The field gradient produces an alternating force on the sample, which causes it to oscillate and flexes the probe. The measurements were conducted at room temperature and the maximum field it can achieve is 1.1 T.

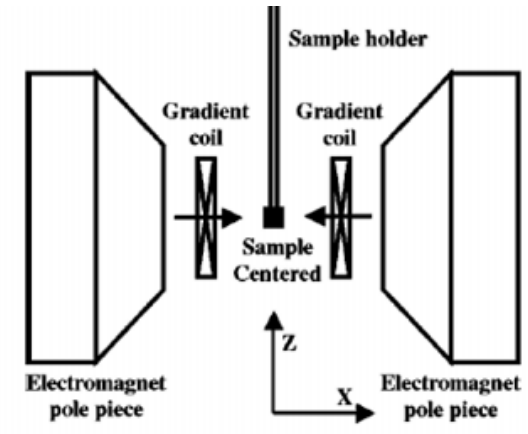

Fig. 4.5 A schematic illustration of an AGFM setup

(2) SQUID

The SQUID magnetometer is a very sensitive (10^{-9} emu) device consisting of two superconductors separated by thin narrow insulating gaps, called Josephson junctions [12]. The measurement is based on the quantum tunneling effects of superconducting electrons across Josephson junctions [11]. A sketch of the device in its usual form is shown in Fig. 4.6. When a superconducting measuring current is made to flow through the ring, it divides so that equal currents pass through each of two Josephson junctions. A changing magnetic flux through the ring generates a voltage and a current in the ring, according to Faraday's Law. Simply speaking, the device is based on the fact that if a constant biasing current is maintained, the measured voltage oscillates with the changes in phase at the two junctions, which depends upon the change in magnetic flux. The flux changes can be measured by counting the oscillations [13].

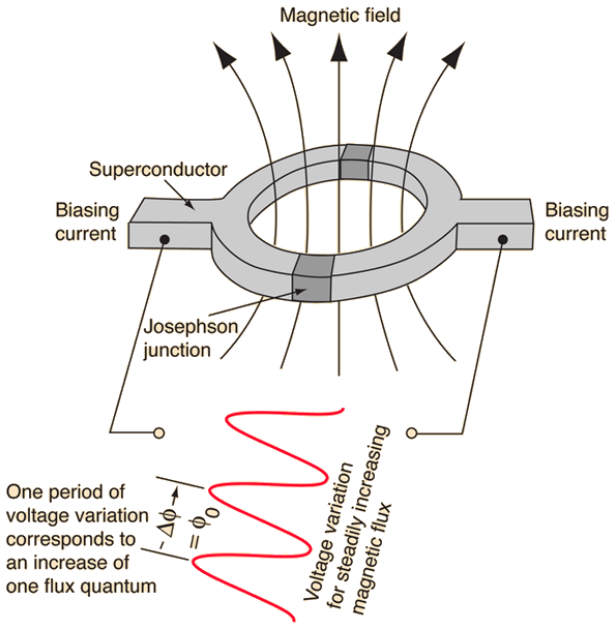

Fig. 4.6 A schematic illustration of a DC-SQUID flux sensor [12]

The magnetic property measurement system (MPMS) comprises the dewar, probe and SQUID assembly, and the electronic control system. The dewar consists of an inner liquid helium reservoir and an outer liquid nitrogen jacket, to reduce excessive liquid helium boil off. The liquid helium is used for maintaining the superconductors as well as for cooling the sample space, if needed. The probe contains a high-precision temperature-control system allowing measurements at a range of temperatures.

In this research, a SQUID magnetometer utilizing a Quantum Design MPMS with a maximum field of 7 T was used for measurement at 300 K. Ribbons were glued and taped onto a silicon substrate which is then inserted in a straw and the straw will be inserted into the sample space for measurements.

4.2.4 Microstructural analysis: TEM/HRTEM

Transmission electron microscopy (TEM) is used to obtain both structural and microstructural information [14]. Unlike optical microscopy, TEM utilize electrons as the source of illumination, which provides much higher resolution (the smallest distance that can be resolved). For instance, for an accelerating voltage of 200 kV in TEM, the resolution is 0.3 nm as compared to 300 nm in a standard optical microscope. High voltage accelerated electrons transmit through the electron transparent samples; through the interaction between the electrons and the sample, different forms of contrast and quantitative information can be generated, which can be interpreted into the microscopic structural detail and the chemical information present in the sample.

The electron column of a TEM consists of an electron gun and 5 or more electromagnetic lenses operating in vacuum. A typical TEM can be divided into three systems labelled in Fig. 4.7. The electron gun (the virtual source), one crucial component in the illumination system, can be: (1) a thermionic (heated filament) gun or (2) a field emission gun where electrons are extracted by a strong electric field. The electron beam is accelerated to an energy in the range of 20 – 1000 keV. The accelerated electrons will travel in a controlled manner, with the help of the first and second condenser lens and a condenser aperture, in order to produce a beam of electrons with a desired diameter. The illumination system can operate in a parallel beam mode and a convergent beam mode. This research mainly used the parallel beam mode which is used for TEM imaging and selected area diffraction (SAD). The objective stage is where the electron beam interacts with the sample and creates images and diffractions patterns which are subsequently magnified using the intermediate lenses and the projector lens. The phosphor

(fluorescent) screen is used for viewing (converting electrons into visible light signal) and either CCD or TV cameras can be used for recording.

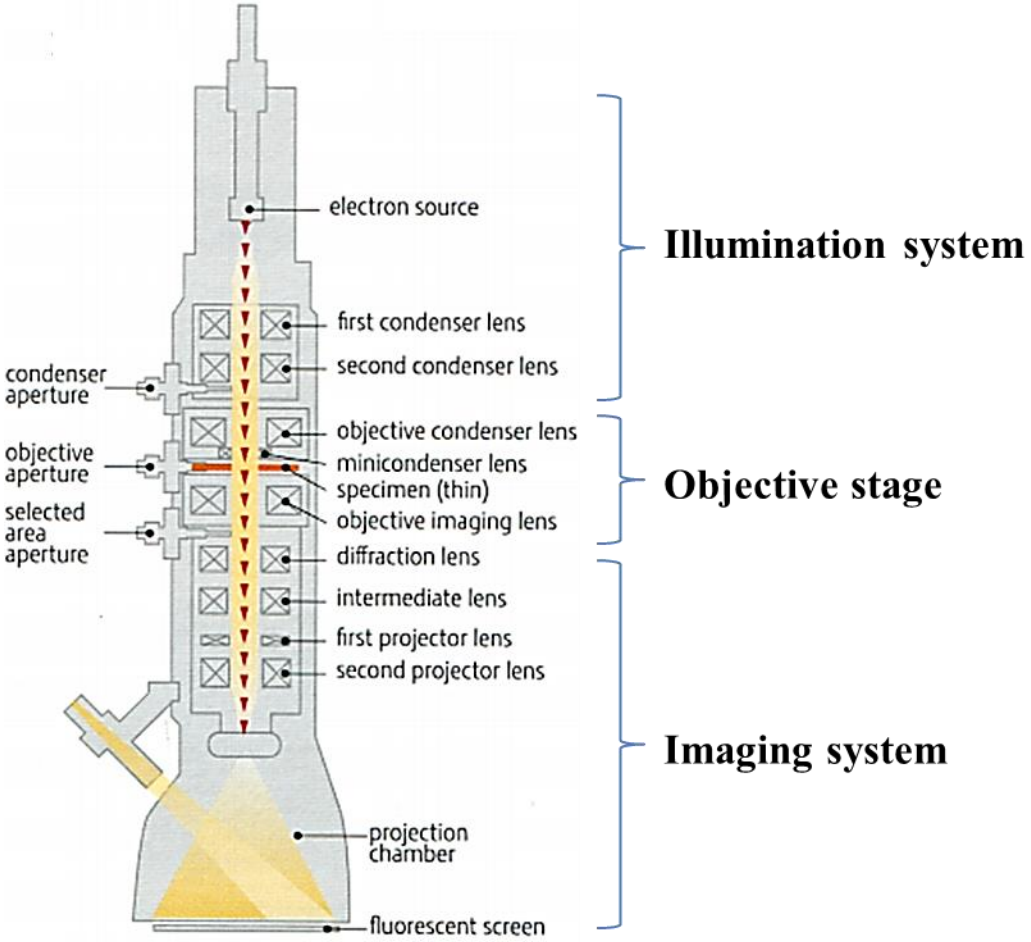

Fig. 4.7 A schematic illustration of the electron column [15]

The objective stage is viewed as the heart of a TEM because both various images and diffraction patterns, incorporating the electron density distribution, are generated here, specifically by the objective lens, shown in Fig. 4.8. The objective lens brings together both the transmitted electrons and the small-angle diffracted electrons to the back focal plane, where the diffraction pattern is formed. If we focus the diffraction lens on the back focal plane of the objective lens, a diffraction pattern can be seen on the screen. However, when we focus the diffraction lens on the image plane of the objective

lens and introduce an aperture in the back focal plane of the objective lens, an image of the sample can be produced on the screen.

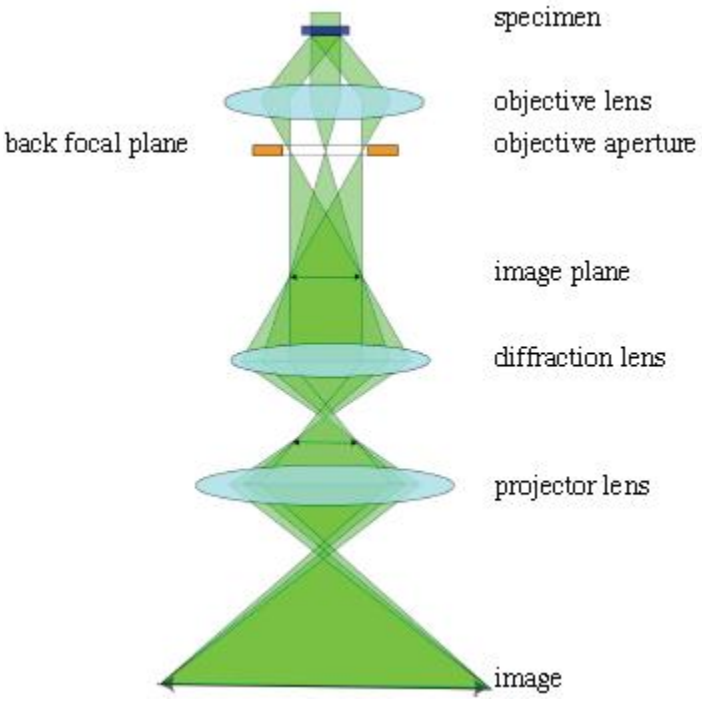

Fig. 4.8 Illustration of formation of images [15]

(1) TEM imaging

A TEM image provides high-resolution information of the internal structure of the material including the grains and crystal structure defects through image contrast. The image contrast, i.e. electron intensity, created by the differential scattering and absorption of electrons are produced by three important mechanisms: (1) mass-thickness contrast (2) diffraction or amplitude contrast and (3) phase contrast.

Mass-thickness contrast originates from incoherent elastic scattering of electrons. Electrons, when they go through the sample, are scattered off axis by elastic nuclear interaction (Rutherford scattering). In general, both the atomic number *Z* and the

thickness of the sample affect the scattering behavior. The cross section (the likelihood of electrons being scattered) is a function of the atomic number *Z*: the higher the atomic number, the more the scattering behavior. In addition, as the thickness of the sample increases, the elastic scattering also increases since the mean free path (the average travel distance) of electrons is fixed. Mass-thickness contrast is the primary mechanism for biological materials and non-crystalline materials.

Diffraction contrast appears by virtue of the interception or allowing of the diffracted electrons by the objective aperture. When a small aperture (5 –70 μm) inserted in the back focal plane intercepts the diffracted beam allowing only the direct beam to contribute to the image, a bright field (BF) image is formed (Fig. 4.9 A). Alternatively, when the objective aperture is inserted in the way that the diffracted beam is used to contribute to the image, a dark field (DF) image will be produced. Dark field images can be produced by either displacing the objective aperture (Fig. 4.9 B) or tilting the sample so that the diffracted beam travels along the optic axis (Fig. 4.9 C). Due to the non-ideal condition of the electron column, the centered dark field approach (Fig. 4.9 C) is mostly adopted since it provides better image quality when the electron path is close to the optic axis. Diffraction contrast is the dominant mechanism for object detail > 15 Å in crystalline materials and is widely used for study of crystal defects. In this research, bright field images were taken and the grain size information, grain morphology and anti-phase boundaries can be obtained or revealed. In terms of grain size analysis, long and short axes of individual grains were averaged to obtain grain size, and at least 20 grains were analyzed for each sample. The grain morphology usually can reveal the nucleation and growth behavior. The anti-phase boundaries occur during the disorder-order

transformation (the $SmCo_7$ structure to the Sm_2Co_{17} structure in this research), as a result of different ordering within an ordered alloy.

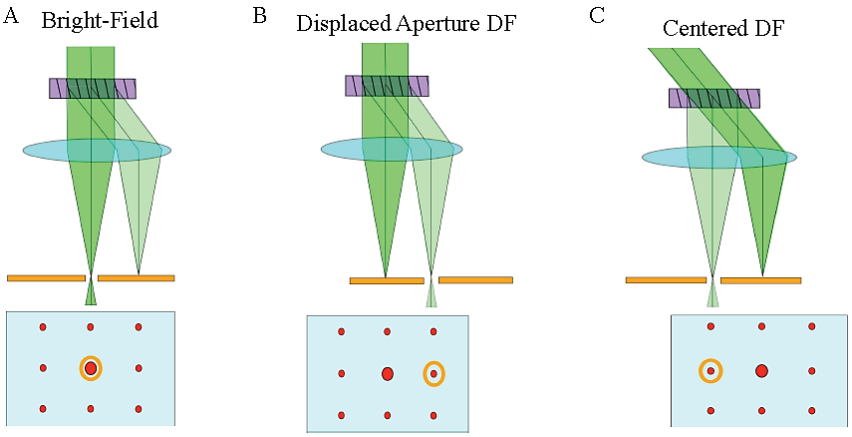

Fig. 4.9 BF and DF image formation [15]

Phase contrast arises from the recombination of the electrons after exiting the sample since differences in the phases of the electron waves create intensity variations in the image. Unlike the diffraction contrast in BF or DF images, where only one direct beam or one diffracted beam were used to form images, the phase contrast—basis for high-resolution (HR) TEM—results from the interference of at least two beams and commonly many beams. Phase contrast is the dominant mechanism for object detail < 10 Å, for example, the lattice fringes, moiré patterns (additional periodicity produced by superimposed similar crystal lattices) and short-range order including that of amorphous materials. It should be noted that in HRTEM, phase contrast also carries the diffuse intensity between Bragg diffractions. When interpreting the high resolution lattice fringes, fast Fourier Transform (FFT) was used to transform the image into a diffraction pattern which can be further analyzed for extraction of the crystal structure information.

(2) Electron diffraction

As mentioned before, if we focus the diffraction lens on the back focal plane of the objective lens without inserting an objective aperture, a diffraction pattern can be seen on the screen. The resultant patterns contain either concentric rings or well-arranged dots depending on the grain structure of the material. The generation of an electron pattern is the same as x-ray diffraction patterns only with different sources of radiation. Simply speaking, the rings or dots correspond to the diffraction peaks in x-ray diffraction patterns. Similarly, superlattice reflections will appear for ordered materials. Electron diffraction patterns can provide information of the phases present and the crystallographic information of materials in a quantitative manner.

Whereas x-ray diffraction is a collective behavior of the entire sample, electron diffraction is able to provide localized information of the material. This is enabled by introducing selected area apertures (Fig. 4.7) after the objective imaging lens, only allowing for a fraction of the electrons passing through and forming the image. Selected area diffraction (SAD) is very useful for identifying detailed structural information regarding specific crystallographic orientations.

One useful expression (Eqn. 4.4) is used to identify the crystal structures via electron diffraction patterns. This expression correlates four parameters: the distance between the diffracted spot (ring) and the direct beam R, the atomic spacings d, the camera length L and the electron wavelength λ. Here R can be directly measured from given electron patterns. The electron wavelength λ can be obtained through Broglie's formula in Eqn. 4.5, where h is the Plank constant (= 6.63×10^{-24} J·s), e is the electronic charge (= 1.6×10^{-19} C), m_0 is the rest mass of the electron (= 9.11×10^{-31} kg), V is the

accelerating voltage and c is the speed of light in vacuum (= 2.998×10^8 m/s). For an accelerating voltage of 200 kV, the corresponding λ is 0.00252 nm. The camera length L is usually obtained from standard Al or Si samples.

$$Rd = \lambda L \tag{4.4}$$

$$\lambda = \frac{h}{[2m_0 eV(1+\frac{eV}{2m_0 c^2})]^{1/2}} \tag{4.5}$$

In this research, microstructural studies via transmission electron microscopy (TEM) were performed using JEOL 2010 operating at 200 kV and a Tecnai Osiris. Electron transparency was achieved by mounting ribbons on slotted Cu support grid and ion milling to perforation using a Gatan PIPS (Precision Ion Polishing System) at 4.5 kV.

4.2.5 Microchemistry observation: 3D Atom Probe Tomography

3D Atom Probe Tomography is a unique method for investigating atomic scale chemistry both at the surface of materials and in the bulk [16]. A 3D atom probe microscope technique is a combination of a focused ion microscope (FIM), a mass spectrometer, a position-sensitive single atom detector, a fast laser and voltage pulsing system, high speed electronics, and reconstruction and analysis software packages. The key technique for the detection of a single ion also includes a local counter electrode and a microchannel plate amplifier (MCP) [17].

Fig. 4.10 is a schematic diagram of a 3D atom probe. The surface atoms of the sample, evaporated by pulsed high voltage or laser, pass the aperture in the local electrode and enter the field free region where their times of flights are recorded by the mass spectrometer. Then the individual ion hits the MCP and the signal is magnified strong enough to be detected by the multi-anode position-sensitive detector [17]. The

chemical species, the X-Y positions of ions and their hitting sequence can be identified using the mass spectrometer. The evaporated volume can then be reconstructed with the spatial and compositional information.

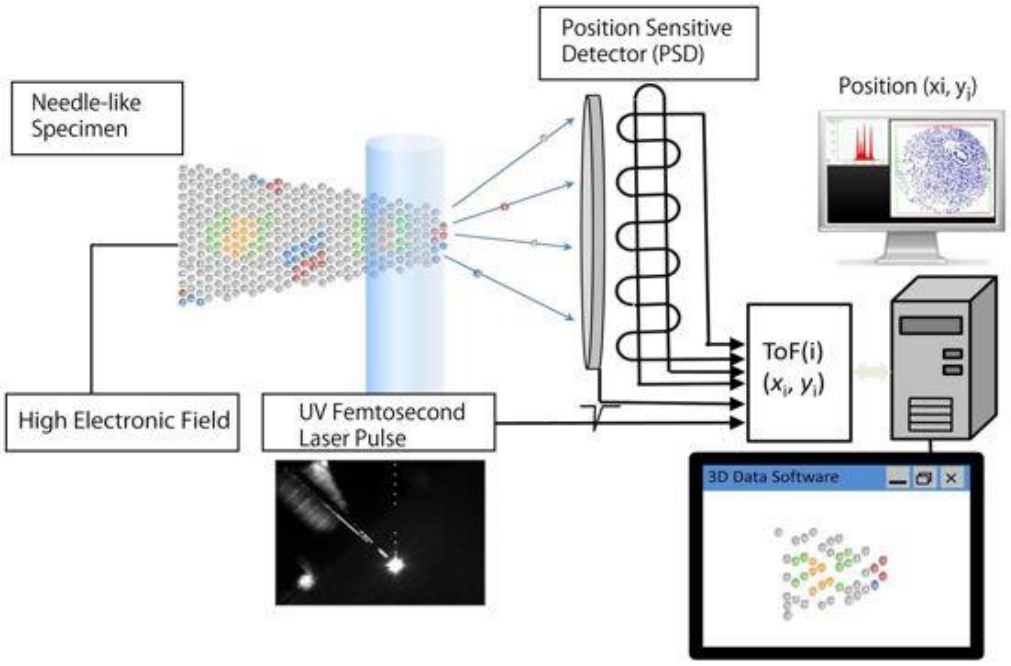

Fig. 4.10 A schematic diagram of 3D atom probe tomography [18]

In this research, the 3D atom probe experiments were conducted using CAMECA LEAP 4000 XHR system in voltage mode of evaporation using 40K sample temperature and evaporation rate maintained at 0.005 atoms per pulse. Samples for atom probe tomography were fabricated by focused ion beam lift-out process using an FEI Helios Nanolab focused ion beam system equipped with an Omniprobe nanomanipulator. The needle shaped sample before laser evaporation is captured in Fig. 4.11.

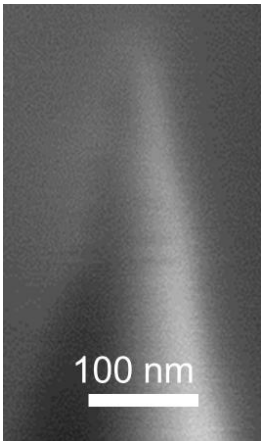

Fig. 4.11 Needle-shaped sample prepared for 3D atom probe observation

References

[1] http://www.wisegeek.com/what-is-an-electric-arc.htm.

[2] U. S. Patent 905, to E. A. Strange and C. H. Pim.

[3] U. S. Patent 2825, to R. B. Pond, Sr. .

[4] H. Liebermann, Mater. Sci. Eng., 43 (1980) 203-210.

[5] S. Stock, B. Cullity, Prentice Hall, Upper Saddle River, NJ, (2001).

[6]https://dl.sciencesocieties.org/publications/books/articles/sssabookseries/methodsofsoilan5/81?show-t-%20%20f=tables&wrapper=no.

[7] A. Patterson, Phys. Rev., 56 (1939) 978.

[8] http://en.wikipedia.org/wiki/Differential_thermal_analysis.

[9] http://www.hitachi-hitec-science.com/en/products/thermal/tec_descriptions/dta.html.

[10] http://www-ipcms.u-strasbg.fr/spip.php?rubrique378.

[11] B.D. Cullity, C.D. Graham, Wiley IEEE publishing, (2009) 130-132, 204, 102.

[12] http://hyperphysics.phy-astr.gsu.edu/hbase/solids/squid.html.

[13] S. Aich, dissertation, Crystal structure, microstructure and magnetic properties of rapidly solidified samarium-cobalt based alloys, 2005.

[14] D.B. Williams, C.B. Carter, The Transmission Electron Microscope, in: Transmission Electron Microscopy, Springer, 2009, pp. 3-22.

[15] http://micron.ucr.edu/public/manuals/Tem-intro.pdf.

[16] http://www.physics.ox.ac.uk/lcfi/FastImSem/PaulBagot.pdf.

[17] http://lib.dr.iastate.edu/cgi/viewcontent.cgi?article=1698&context=etd.

[18] http://www.nims.go.jp/mana/news/press/press_200906151/.

Chapter 5 Study of transition metal alloying tendencies in $SmCo_7$ permanent magnets through a straightforward method

Before discussing experimental results, this chapter discusses the anisotropy variations different alloying elements induce to the $SmCo_7$ structure using a semi-empirical approach and aims to help understand the fundamentals of the anisotropy sources.

The atomic site selection of transition metals in $SmCo_7$ compound was investigated by the extended application of Miedema's binary alloy formation model with appropriate assumptions introduced. The heat of formation of multiple transition metals with respect to both Sm and Co was calculated using this semi-empirical cellular model. By equating the alloying tendencies (strength of affinity) to the selection of nearest neighbors, the site of substitution for Co atoms with different transition metals was determined, in agreement with experimental findings. The results are used to discuss the changes in the intrinsic magnetic properties observed due to the substitution.

5.1 Introduction

Sm-Co intermetallic compound with the $TbCu_7$ structure, due to its high Curie temperature, low intrinsic coercivity temperature coefficient (β = -0.10 to -0.16 % $^oC^{-1}$), strong uniaxial magnetocrytalline anisotropy (105 - 140 kOe) and large magnetization [1], has recently garnered great research interest as a potential high performance permanent magnet [2-4]. It is a metastable structure closely related to the other two Co-rich Sm-Co compounds, i.e. $SmCo_5$ and Sm_2Co_{17}. As it is well known, Sm_2Co_{17} can be obtained from $SmCo_5$ by appropriate substitution for Sm atoms with Co dumbbell pairs [5], while Sm-Co 1:7 is a disordered phase derived from $SmCo_5$ structure by random substitution for Sm atoms with Co dumbbell pairs [6]. However, this

phase, though highly preferred, does not form readily [7]. A third doping element is necessary to stabilize the Sm-Co 1:7 phase with the $TbCu_7$ structure. Among popular doping elements, transition metals are able to introduce a variety of effects to the intrinsic properties of the $SmCo_7$-based magnetic materials, including Curie temperature (T_c) and the anisotropy field. For example, the introduction of a small amount of Cu in this system increased T_c by roughly 100 K [8] and the presence of Zr in the $SmCo_{7-x}Zr_x$ (x = 0-0.8) system significantly increased the anisotropy [9, 10]. Extensive studies of the anisotropy changes due to substitution effects in the $SmCo_7$ structures were reported in Ref [11].

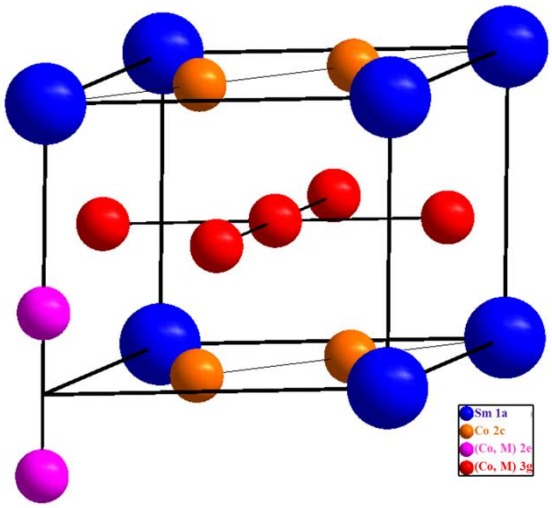

Fig. 5.1 Atomic structure of $Sm(Co, M)_7$

The effect of a specific alloying element on the intrinsic magnetic properties depends on site selection for the substitutional element. The structure of the $Sm(Co, M)_7$ (M denotes any transition metal) intermetallic compound is shown in Fig. 5.1. Different sites for Co atoms are also labeled. There are three different Co sites: 3g, 2e and 2c using the Wyckoff notation. The nearest neighbors for each of the sites are 4 Sm and 8 Co for

3g, 1 Sm and 13 Co for 2e, and 3 Sm and 9 Co for 2c [11]. Streever [12] reported that the uniaxial Co anisotropy in $SmCo_5$ systems primarily arises from the 2c sites, whereas Co atoms on the 3g sites have small negative contributions. However, when Sm is replaced by Co-Co dumbbells at 2e sites, the anisotropy will be reduced [13, 14]. On the other hand, if the doping elements substitute for Co atoms on the 2e sites, the reduction in magnetocrystalline anisotropy is less. Likewise, if the doping elements substitute on the 3g sites, the negative contribution to anisotropy will also be decreased. Thus, it is important to predict *a priori* site the alloying element is most likely to occupy in order to further understand the cause of the doping effects and facilitate alloy designs.

Y. Guo et al investigated the magnetism of Sm-Co 1:7 intermetallics modified with third elements by using a corrected magnetic valence model where the specific site selection was ignored [15]. J. Luo et al studied the doping effects of Si, Cu, Ti, Zr and Hf in the Sm-Co 1:7 phase by taking into account of the enthalpy of formation, atomic radius and electronegativity separately [14]. While first principle calculations have been made to the conventional Sm-Co permanent magnet made from the two-phase nanostructure predicting the solubilities of Cu, Ti and Zr in $SmCo_5$ and Sm_2Co_{17} phases respectively [16], little thorough theoretical attempt has been made to predict the alloying tendencies in the transition-metal-modified Sm-Co 1:7 structure so far due to its disordered nature though relatively extensive experiments have been accomplished to investigate the structural and magnetic properties. In this communication, an approach based on a cellular model is proposed where the heat of formation of transition metals with respect to Sm and Co are calculated to serve this purpose.

The calculations were extended to predict the magnitude of affinity between the transition metal dopants and Sm or Co. As a result, the preferred site occupancy of a specific transition metal in this intermetallic compound can be predicted, which provides good explanations to the effects of doping on the intrinsic magnetic properties. The site predictions that resulted from the model were compared with experimental findings for site occupancy available in the literature.

5.2 Model description and calculations

A.R. Miedema et al. [17] introduced an atomic model which calculates the heat of formation between two metals by considering the energy effects and electron density difference in binary alloys. There are two contributions in the energy effect for heat of formation. One is negative arising from the difference in chemical potential $\Delta\varphi$ for electrons at the two types of atomic cells while the other one is positive representing the discontinuity in the density of electrons, Δn_{ws}, at the boundary between dissimilar cells. It is expressed as

$$\frac{\Delta H}{N_0} = f \times g \times [-Pe(\Delta\varphi)^2 + Q(\Delta n_{ws}^{1/3})^2 - R], \qquad (1)$$

Where ΔH stands for heat of formation per gram atom, *e* is elementary electron charge, *f* and *g* takes into account the actual contact between dissimilar cells. *P* and *Q* are fitted proportionality parameters and *R* takes into account the additional hybridization energy between transition metals and rare earth elements. Constants are taken from ref [17] and ref [18]. Details can be found in the appendix.

This model is widely used in predicting binary alloy formations. However, in order to use this model in the Sm-Co 1:7 phase, a couple of assumptions have to be made. It is assumed this system is in equilibrium state and it has complete mixing between dissimilar atoms excluding the non-substituting scenarios.

The results are shown in Fig. 5.2 and Fig. 5.3. It can be seen that the magnitude of heat of formation is dependent on the atomic concentration of the components involved. In general, the absolute value follows the trend that it increases first, peaks at around equiatomic concentrations then decreases. It is reasonable since at around equiatomic concentrations, the system has the most contact between dissimilar atoms. In addition, Sm and Co form the most stable compound compared with other transition metals given the fact that they have the most negative enthalpy value.

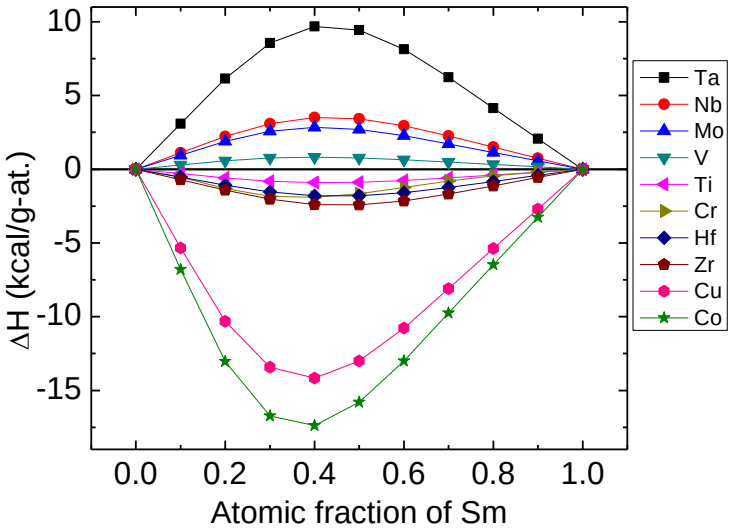

Fig. 5.2 Heat of formation for transition metals with respect to Sm

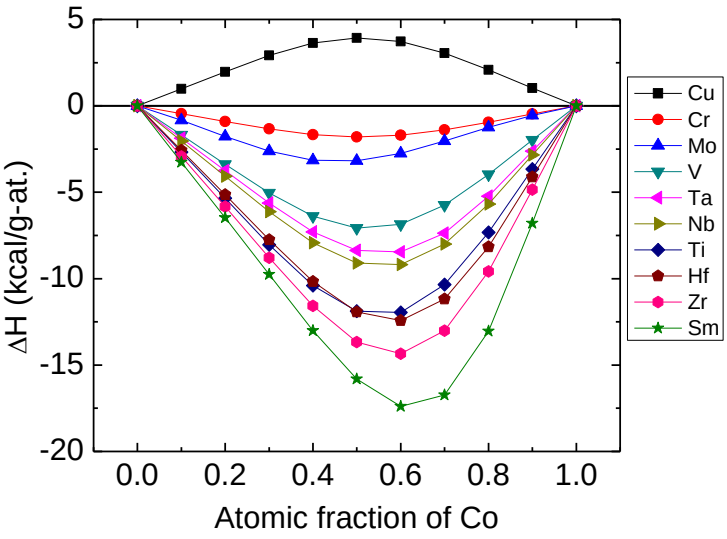

Fig. 5.3 Heat of formation for transition metals with respect to Co

Apart from what is described above, the transition metals involved in this discussion can be classified into three categories shown in Table 5.1. One is those metals which have positive heats of formation with Sm and negative with Co; in our case, Mo, Nb, Ta and V belong to this category. The second is those which have positive heats of formation with Co but negative with Sm, such as Cu. The rest of the metals belong to the category that they have larger negative heats of formation with Co than with Sm, which are Cr, Hf, Ti and Zr.

Positive ΔH implies that the two elements avoid interaction, whereas negative ΔH indicates that interaction is preferred. For instance, according to our calculation, Nb has a positive ΔH with Sm, while it has a negative ΔH with Co; therefore it will associate with Co rather than Sm. However, for Zn the situation is completely the opposite since it bears a positive ΔH with Co and a negative ΔH with Sm.

Table 5.1 Signs of heat of formation between different transition metals and Sm & Co

	Category I				Category II	Category III			
	Mo	*Nb*	*Ta*	*V*	*Cu*	*Cr*	*Hf*	*Ti*	*Zr*
Sm	+	+	+	+	-	-	-	-	-
Co	-	-	-	-	+	--	--	--	--

"-" denotes negative sign, "--" denotes relative larger negative value.

5.3 Discussions

The question now is whether or not the relative heats of formation calculations can predict *a priori* site preferences of alloying elements. To determine this, one can compare calculated ΔH , and thus the predicted site preferences, with actual site occupancies, the latter information available in the literature for many substituents. For example, since ΔH of Nb/Sm is positive and ΔH of Nb/Co is negative, it is predicted that Nb would occupy the 2e sites since these sites minimize Sm nearest neighbors and maximize Co nearest neighbors. By the same fashion, Cu will go to 3g sites with most number of Sm atoms and least number of Co atoms as neighbors. Likewise we can predict where other transition metals will go. Specific site predictions and specifications are shown in in Table 5.2.

Table 5.2 Site predictions based on enthalpy calculations and actual site occupancy from experimental results

Elements	Predictions	Actual sites
Cr	2e	2e [19]
Cu	3g	3g [20]
Hf	2e	2e [21]
Mo	2e	2e [19]
Nb	2e	2e [11]
Ta	2e	2e [19, 22]
Ti	2e	2e [23]
V	2e	2e [24]
Zr	2e	2e [10], 3g [10, 25]

As seen in Table 5.2, there is a tremendously strong agreement between the predicted site occupancy based on our thermodynamic model and the site occupancy reported in the literature. It should be noted, however, that this technique applies to substitutional additives, but does not address solubility limits.

In terms of magnetic properties, our findings also qualitatively support the experimental data found from literature. As stated in introduction part, the third element which substitutes either 3g site or 2e site is going to increase the c-axis anisotropy, extrinsically substantiated by the fact of the increase in coercivity with increasing amount of the third element (Table 5.3). On the other hand, due to the non-ferromagnetic nature of those third elements, the saturation of the system will no doubt experience a decrease which is also consistent with the data shown in Table 5.3. The increasing amount of the

third element also results in decreased Curie temperature as expected due to the decline of interaction between the sublattices.

Table 5.3 Saturation magnetization, coericivity and Curie temperature of $SmCo_{7-x}M_x$ compounds

Elements	x	M_s (emu/g)	H_c (kOe)	T_c(ºC)
Cr [19]	0.1	65	1.2	
	0.2	62	2.4	
Cu [8, 20]	0.1			850
	0.3			828
Hf [21]	0.1	104	244*	807
	0.2	102	282*	805
Mo [19]	0.1	71	1.2	
	0.2	69	2.7	
Nb [11]	0.1	69	5.0	
	0.2	62	10.1	
Ta [26]	0	75	1.9	
	0.1	65	4.2	
	0.2	60	7.5	
Ti [23]	0.21	96	156*	756
	0.28	94	175*	745
V [24]	0.1	58	6.2	
	0.2	55	9.0	
Zr [9]	0.2	103	215*	762
	0.3	96	240*	760

*denotes anisotropy field

5.4 Conclusions

The heat of formation of transition metals with respect to Sm and Co was investigated using a cellular model which takes into consideration the synergic effect of the differences in electron density distribution, chemical potentials and atomic molar volumes between dissimilar cells. It has been demonstrated that this calculations were able to predict the site preferences of each transition metal in the system, and the predicted substitution sites together with the magnetic properties obtained fit well with the experimental results available in the literature. This model can also be extended to non-transition metals substituents, as well as other systems which might provide further insights in materials with multi-elemental doping events. This ability to *a priori* predicted site occupancies will significant impact alloy design, making alloy design more straightforward.

Aknowledgement

The authors are grateful to the National Science Foundation under Grant No. DMR0804744.

References

[1] Z. Zhang, X. Song, W. Xu, Acta Mater., 59 (2011) 1808-1817.

[2] J. Liu, T. Chui, D. Dimitrov, G. Hadjipanayis, Appl. Phys. Lett., 73 (1998) 3007-3009.

[3] J. Shield, V. Ravindran, S. Aich, A. Hsiao, L. Lewis, Scr. Mater., 52 (2005) 75-78.

[4] J. Zhou, R. Skomski, C. Chen, G.C. Hadjipanayis, D.J. Sellmyer, Appl. Phys. Lett., 77 (2000) 1514-1516.

[5] Y. Khan, Acta Crystallogr., Sect. B, 29 (1973) 2502-2507.

[6] K. Buschow, A. Van der Goot, Acta Crystallogr., Sect. B, 27 (1971) 1085-1088.

[7] Y. Guo, W. Li, W. Feng, J. Luo, J. Liang, Q. He, X. Yu, Appl. Phys. Lett., 86 (2005) 192513-192513-192513.

[8] I. Al-Omari, Y. Yeshurun, J. Zhou, D. Sellmyer, J. Appl. Phys., 87 (2000) 6710-6712.

[9] M. Huang, W. Wallace, M. McHenry, Q. Chen, B. Ma, J. Appl. Phys., 83 (1998) 6718.

[10] Y. Chen, C. Hsieh, S. Lo, W. Chang, H. Chang, S. Chiou, H. Ouyang, J. Appl. Phys., 109 (2011) 07A748.

[11] Z. Guo, H. Chang, C. Chang, C. Hsieh, A. Sun, W. Chang, W. Pan, W. Li, J. Appl. Phys., 105 (2009) 07A731-707A731-733.

[12] R. Streever, Phys. Rev. B, 19 (1979) 2704.

[13] S. Aich, J. Shield, J. Magn. Magn. Mater., 279 (2004) 76-81.

[14] J. Luo, J. Liang, Y. Guo, Q. Liu, F. Liu, Y. Zhang, L. Yang, G. Rao, Intermetallics, 13 (2005) 710-716.

[15] Y. Guo, W. Feng, W. Li, J. Luo, J. Liang, J. Appl. Phys., 101 (2007) 023919--023917.

[16] R. Sabirianov, A. Kashyap, R. Skomski, S. Jaswal, D.J. Sellmyer, Appl. Phys. Lett., 85 (2004) 2286.

[17] A. Miedema, R. Boom, F. De Boer, J. Less-Common Met., 41 (1975) 283-298.

[18] C. Colinet, A. Pasturel, A. Percheron-Guegan, J. Achard, J. Less-Common Met., 102 (1984) 167-177.

[19] C. Hsieh, H. Chang, Z. Guo, C. Chang, X. Zhao, W. Chang, J. Appl. Phys., 107 (2010) 09A738-709A738-733.

[20] J. Luo, J. Liang, Y. Guo, Q. Liu, L. Yang, F. Liu, G. Rao, W. Li, J. Phys.: Condens. Matter, 15 (2003) 5621.

[21] J. Luo, J. Liang, Y. Guo, L. Yang, F. Liu, Y. Zhang, Q. Liu, G. Rao, Appl. Phys. Lett., 85 (2004) 5299-5301.

[22] Z. Guo, C. Hsieh, H. Chang, M. Zhu, W. Pan, A. Li, W. Chang, W. Li, J. Appl. Phys., 107 (2010) 09A705-709A705-703.

[23] J. Zhou, I. Al-Omari, J. Liu, D.J. Sellmyer, J. Appl. Phys., 87 (2000) 5299.

[24] C. Hsieh, H. Chang, C. Chang, Z. Guo, C. Yang, W. Chang, J. Appl. Phys., 105 (2009) 07A705-707A705-703.

[25] J. Luo, J. Liang, Y. Guo, Q. Liu, L. Yang, F. Liu, G. Rao, J. Alloys Compd, 372 (2004) 187-189.

[26] Z. Guo, C. Hsieh, H. Chang, M. Zhu, W. Pan, A. Li, W. Chang, W. Li, J. Appl. Phys., 107 (2010) 09A705.

Appendix:

In general the heat of formation can be expressed as

$$\Delta H \sim -Pe(\Delta\varphi)^2 + Q(\Delta n_{ws}^{1/3})^2 - R \qquad (1)$$

In order to apply equation 1, the overall parameters were obtained as follows. It was assumed that the chemical potential for electrons, φ, has a one-to-one correspondence to the experimental value of the electronic work function, $\varphi_{\exp}$, of pure metals, and it was taken as the best fit of $\varphi_{\exp}$. The value for n_{ws} can be derived theoretically from charge distributions in a pure metal crystal, i.e., the summation of atomic charge densities. It can also be measured experimentally from the ratio of the bulk modulus *B* and the molar volume V_m. An approximately justified relation of $n_{ws}^2 \sim B/V_m$ was used to estimate n_{ws} f or those metals for which by summing up free atom charge distributions leads to unreliable results. Values of φ and n_{ws} for different metals are listed in Table 5.4.

Information concerning the sign of ΔH was obtained from binary phase diagram. For intermetallic compounds where entropy effects are relatively insignificant, it is assumed that ΔH has a negative sign for all binary systems in which stable intermetallic compounds have been observed, whereas it is taken as positive for those with no compounds but with mutual solid solutions smaller than 10 at.%. According to the sign analysis, the value of R/P and Q/P were obtained as Q/P = 9.4e in units V^2 per (density unit)$^{2/3}$ and $R/P = 0.5eV^2$.

In order to get the absolute ΔH values, one needs more information such as the value of *P* which was determined to be $P = 1.05V^{-1}$. Furthermore, the dependence of

ΔH on the atomic concentrations of the metals has to be specified, which brings in the concept of "surface concentration" analogous to "volume concentration". For metals A and B with atomic concentrations C_A and C_B and molar volumes V_A and V_B, the surface concentrations C_A^S and C_B^S can be defined as follows,

$$C_A^S = \frac{C_A V_A^{2/3}}{C_A V_A^{2/3} + C_B V_B^{2/3}} \qquad (2)$$

$$C_B^S = \frac{C_B V_B^{2/3}}{C_A V_A^{2/3} + C_B V_B^{2/3}} \qquad (3)$$

For ordered compounds or solutions, the actual contact between two dissimilar cells will be larger than statistical values, so the empirical values for the concentration difference between two metals will contain two factors which are denoted by f and g which are defined as follows,

$$f = C_A^S C_B^S [1 + 8(C_A^S C_B^S)^2] \qquad (4)$$

$$g = \frac{2(C_A V_A^{2/3} + C_B V_B^{2/3})}{V_A^{2/3} + V_B^{2/3}} \qquad (5)$$

As a result, the absolute value for heat of formation per gram atom is shown to be

$$\frac{\Delta H}{N_0} = f \times g \times [-Pe(\Delta\varphi)^2 + Q(\Delta n_{ws}^{1/3})^2 - R] \qquad (6)$$

where N_0 is Avogadro's number.

Table 5.4 Parameters needed in equation 6

Elements	φ (Volt)	$n_{ws}^{1/3}$	$V_m^{2/3}$ (cm^2)
Co	5.10	1.75	3.50
Cr	4.65	1.73	3.70
Cu	4.55	1.47	3.70
Hf	3.55	1.43	5.60
Mo	4.65	1.77	4.40
Nb	4.00	1.62	4.90
Ta	4.05	1.63	4.90
Ti	3.65	1.47	4.80
V	4.25	1.64	4.10
Zr	3.40	1.39	5.80
Sm	3.20	1.21	7.37

(n_{ws} in density units; all the values are taken from ref [17], except that for Sm[18])

Chapter 6 Combined effects of chromium and carbon on phase formation and magnetic behavior of melt-spun Sm-Co magnets

It has been shown that different alloying in the $SmCo_7$ structure can result in variations in the intrinsic magnetic properties such as the anisotropy constant and the saturation magnetization. As discussed in Chapter 2, microstructures through processing techniques can lead to changes in the extrinsic properties such as coercivity. This chapter presents the structural and magnetic properties of Cr and C modified Sm-Co alloys (forming the 1:7 structure) obtained from melt-spinning. The effect of heat treatment will also be discussed. The results reported in this chapter have been published in ref [1].

The effects of Cr and C additions on the structures and magnetic properties of Sm-Co alloys have been investigated. X-ray diffraction revealed that the metastable $TbCu_7$-type structure was formed during melt spinning at 40 m/s. The lattice parameters varied with Cr and C content, suggesting dissolution of the alloying additions in the $SmCo_7$ structure. Increasing Cr and C content also promoted the formation of an amorphous phase, as indicated by both x-ray diffraction and differential thermal analysis. The alloying additions significantly refined the microstructural scale from ~1 μm for the simple binary $Sm_{12}Co_{88}$ alloy to approximately 30 nm for the sample with additions of 6 at.% C and 9 at.% Cr. The coercivity of the as-solidified samples increased from 0.5 kOe for the simple binary alloy to 9.8 kOe for the alloy modified with 3 at.% C and 4.5 at.% Cr. The coercivity was also found to be strongly dependent on the temperature of thermal treatments. The coercivity initially increased, and then dramatically decreased before again increasing at higher annealing temperatures. X-ray diffraction and TEM analysis suggest that the development of the ordered Sm_2Co_{17} structure upon annealing may be

influencing the coercivity. Differences in initial susceptibility of the annealed samples suggest a combination of domain wall pinning and nucleation-controlled magnetization mechanisms.

6.1 Introduction

Sm-Co-based permanent magnets have garnered great attention since the late 1960s due to their superior magnetic properties [2, 3]. While Sm-Co 1:5 type and Sm-Co 2:17 type magnets are being produced extensively in industry for high temperature and/or corrosive environment applications, considerable attention was drawn to Sm-Co 1:7 type magnetic materials in the last decade due to their potential application as novel high-temperature permanent magnets [4]. The Sm-Co 1:7 phase, which originated from the $TbCu_7$ structure [5], is a metastable phase from which precipitation-hardened magnets can be derived upon appropriate thermal treatments, but with excellent intrinsic magnetic properties as well.

There is an increasing interest in developing Sm-Co-based permanent magnets with high energy product through alloying and different processing techniques. Conventional melting has proved effective in creating $SmCo_7$ structure while the non-uniform and large-scale microstructure limits the magnetic properties in as-solidified materials. The development of rapid solidification techniques, especially melt spinning, could further manipulate the energy product through the control of the solidification conditions. Formation of appropriate microstructures depends on selective alloying additions which are thought to significantly reduce the microstructural scale and modify the magnetic behavior. For example, the alloying combination of Nb and/or C [6] were

confirmed to refine the grain size from around 1 micron for the simple binary alloy to about 50 nm, resulting in coercivity as high as 40 kOe. Boron containing samples in melt-spun $Sm(CoFeCuZr)_zM_x$ (M = B or C) were also reported to have better magnetic properties owing to the refinement in grain size [7]. P. Saravanan [8] investigated the effect of Sn on melt spun $SmCo_{6.8-x}Zr_{0.2}$ ribbons where a maximum coercivity of 5.1 kOe was obtained. C. C. Hsieh et.al studied the crystal structure and magnetic properties of V [9], Ta, Mo, Cr [10] and Ge [11] doped $SmCo_7$ ribbons, most of which showed a pronounced increase in coercivity, 7.5 kOe specifically for Cr doped alloys. Less research has focused on the heat treatment effect of alloyed $SmCo_7$ materials, with most thermal treatments and alloy compositions mirroring commercial processes [12, 13]. Here we investigate the rapidly solidified structure, grain size refinement and magnetic property changes of Sm-Co based magnets associated with alloying additions Cr and C, as well as the materials' response to thermal post-solidification thermal treatments.

6.2 Experimental

Alloying ingots with nominal compositions of $(Sm_{0.12}Co_{0.88})_{100-(x+y)}Cr_yC_x$ with x ranging from 1 to 6 with a fixed ratio of y/x = 3/2 (compositions are denoted with only C content "x" throughout the text but Cr is present with the exact ratio) were made from high purity (> 99.95 %) elements by arc melting in a high purity argon atmosphere. An extra 5 wt. % Sm was added to the sample in order to compensate for loss due to Sm vaporization during melting. The ingot was then rapidly solidified by melt spinning in high-purity argon at a chamber pressure of 1 atm. and a tangential wheel velocity of 40 m/s.

The samples were analyzed by x-ray diffraction using a Rigaku Multiflex X-ray diffractometer with Cu Kα radiation. The powdered samples were mounted on an off-cut SiO_2 single crystal to avoid the diffraction effects of the sample holder. Crystallization behavior was monitored by differential thermal analysis (DTA) using a Perkin-Elmer System 7 with a heating rate of 10 ºC /min. For annealing, ribbons and powder of the same composition were first wrapped in tantalum foil and then were sealed in quartz capsules with titanium granules inside in an ultra-high purity Ar atmosphere after repeated evacuations. Heat treatments were done at temperatures ranging from 600 ºC to 800 ºC for 15 minutes followed by water quenching. The magnetic properties were measured by Alternating Gradient Force Magnetometry (AGFM) after pulse magnetizing in a 12 T magnetic field. The magnetic field was applied parallel to the ribbon plane in all cases so as to minimize the demagnetizing factors. Transmission electron microscopy (TEM) was accomplished with a JEOL 2010 operating at 200 kV. Electron transparency was achieved by mounting the melt-spun ribbon on slotted Cu support grid and ion milling to perforation using a Gatan PIPS (Precision Ion Polishing System) at 4.5 kV. The grain size was calculated using the Scherrer equation from x-ray diffraction line widths after subtraction of instrument broadening and measured directly from TEM images.

6.3 Results and discussion

The phase formation in $(Sm_{0.12}Co_{0.88})_{100-(x+y)}Cr_yC_x$ as a function of x and y was determined by x-ray diffraction. As Fig. 6.1 shows, the primary phase was indexed to the $TbCu_7$-type structure. Lattice parameters were modified dramatically, as indicated by the

peak shift in the x-ray diffraction pattern (Fig. 6.1 inset), with the calculated results shown in Fig. 6.2. With the increase in alloying content, the "c" lattice parameter increased until x = 3, while the "a" lattice parameter decreased monotonically, with experimental errors ranging within 0.001 - 0.002 Å (shown in error bars). The structural disorder (amorphization) at x = 6 precluded lattice parameter determination of this sample. The trend observed here is similar to that previously observed in Zr- [14] and Ta- [15] modified $SmCo_7$. The plateauing of both "a" and "c" suggests that the solubility limit of combined C and Cr additions is x ~ 3 and y ~ 4.5. In addition, peak broadening suggested that the grain size decreased upon alloying with Cr and C. The grain size calculated using the Scherrer equation was strongly dependent on the C content (Fig. 6.3). Diffuse scattering was also observed to increase with increasing Cr and C additions, indicative of an increasing amorphous phase fraction. This was confirmed by the differential thermal analysis (DTA) (Fig. 6.4-a), which showed an exothermic peak with an onset at ~ 656 ℃ with increasing intensity as the C content increased (Fig. 6.4-b).

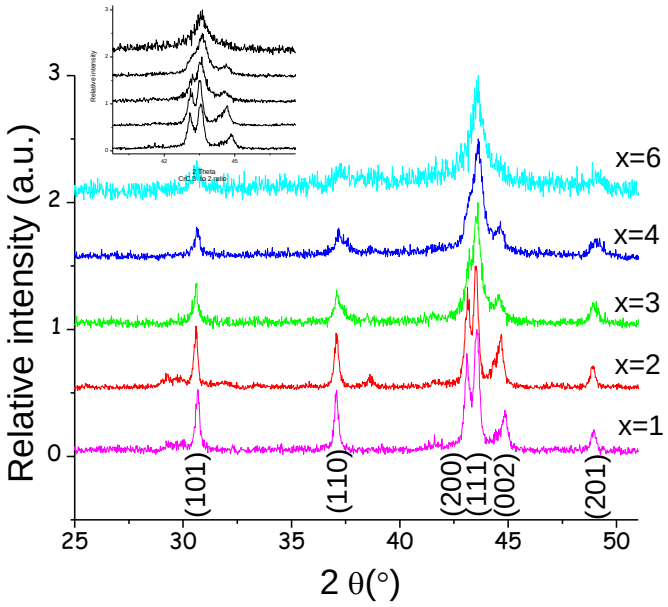

Fig. 6.1 X-ray diffraction patterns for as-spun alloys with different Cr and C content. The inset displays the region between 42° and 47°.

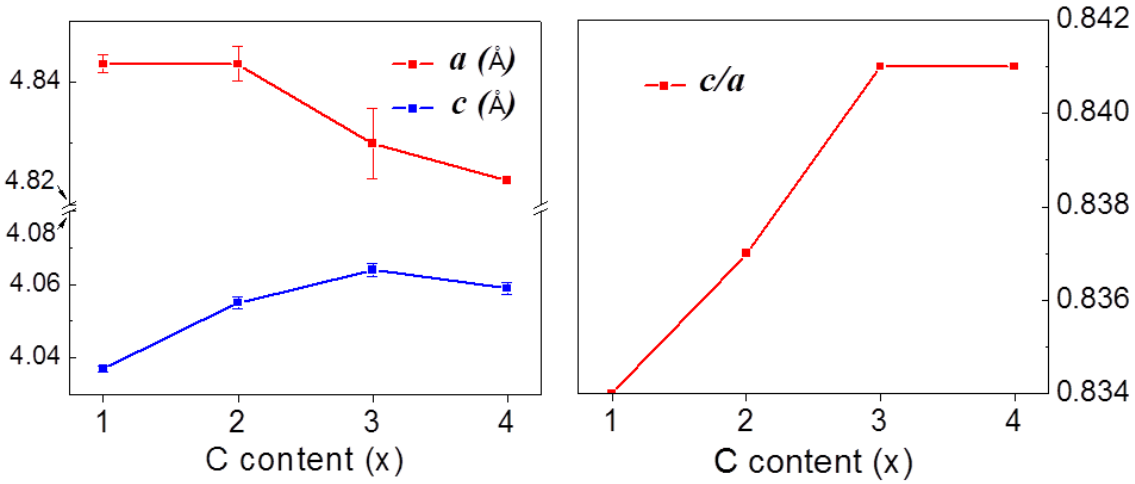

Fig. 6.2 Lattice parameter changes with different C content

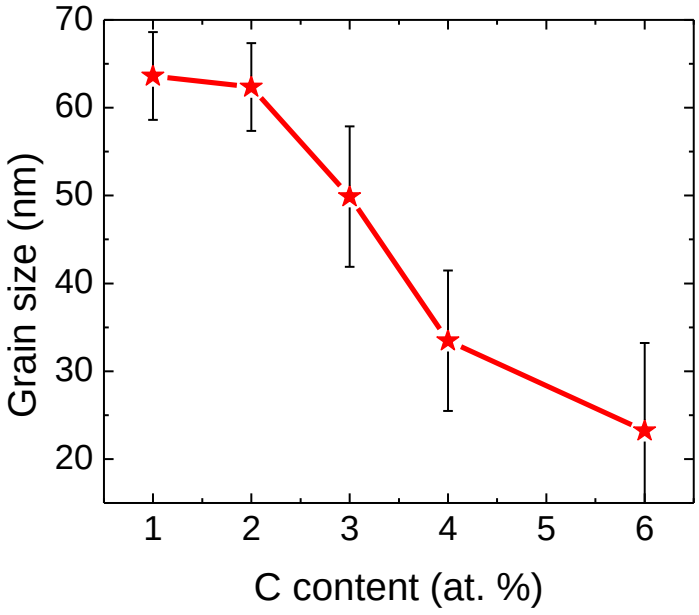

Fig. 6.3 Grain size as a function of C content

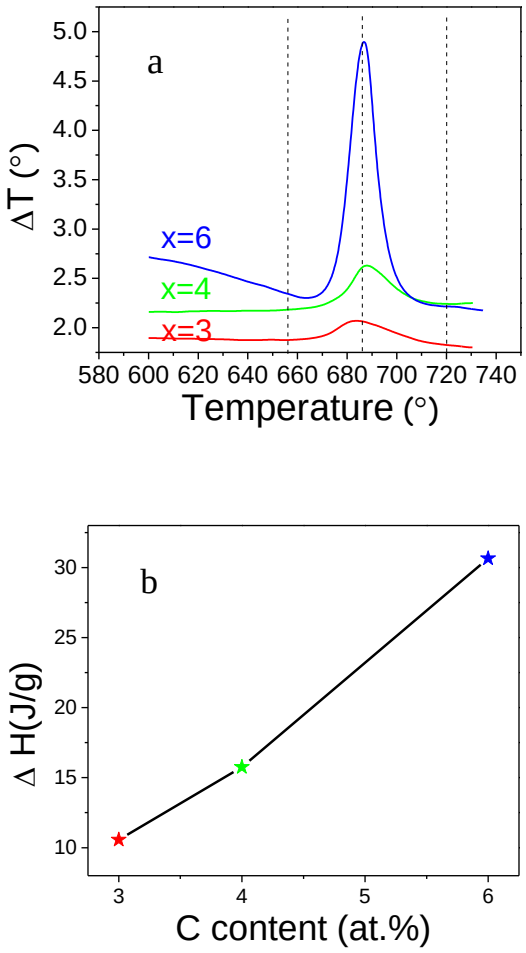

Fig. 6.4 (a) Differential thermal analysis curves for $(Sm_{0.12}Co_{0.88})_{100-(x+y)}Cr_yC_x$ with x = 3, 4 and 6 (y/x = 3/2); (b) Relationship between heat evolution and C content indicating an increasing amorphous fraction with increasing C

Multiple annealing temperatures (as denoted by the dotted lines in Fig. 6.4-a) close to the crystallization temperature of 656 ℃ were investigated in order to understand the phase evolution that resulted from both crystallization and the progression toward equilibrium. The x-ray diffraction patterns for the x = 3 sample (Fig. 6. 5-a) revealed that annealing led to the appearance of a peak at ~38.5° 2θ. This is the (024) peak from the

ordered Sm_2Co_{17} (Th_2Zn_{17}) phase. Other than the diffraction peaks becoming slightly less broad, no other changes were evident. For the x = 6 alloy, similar development of the Sm_2Co_{17} phase was observed, also evident was the appearance of peaks due to Cr_3C_2 after annealing at 800 ℃ (Fig. 6.5-b).

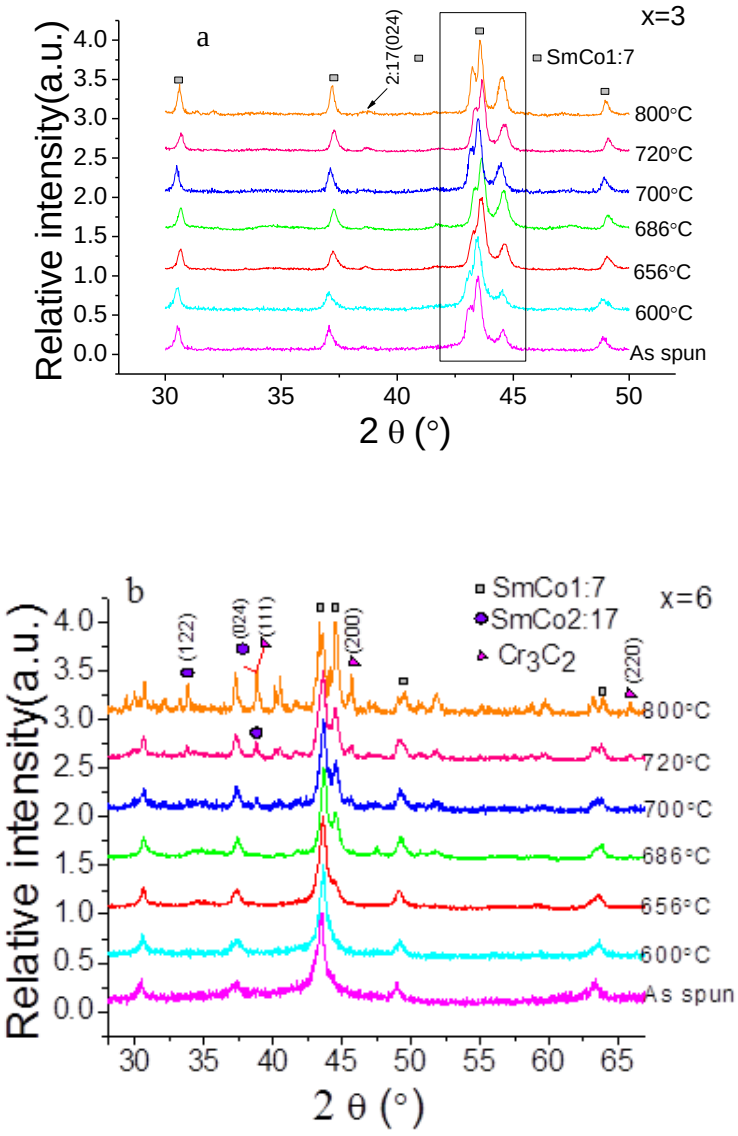

Fig. 6.5 X-ray diffraction patterns for (a) for x = 3 and (b) x = 6 samples annealed at different temperatures

The magnetic measurements were conducted for both the as-spun samples and the as-annealed samples. For the as-spun materials, the coercivity increased at small concentrations of Cr and C due to the significant grain size reduction upon alloying [16] (Fig. 6.6-a). However, above 3 atomic percent C, a dramatic decrease in coercivity was observed despite a continuing grain refinement. The decrease in coercivity is due to the increasing fraction of the soft magnetic amorphous phase. A progressive study of the hysteresis loops showed a single magnetic phase behavior at lower alloying content. However, the hysteresis loops develop a "kink" in the second quadrant when the atomic fraction of carbon amounts to 3 atomic percent or higher resulting from the presence of the amorphous phase.

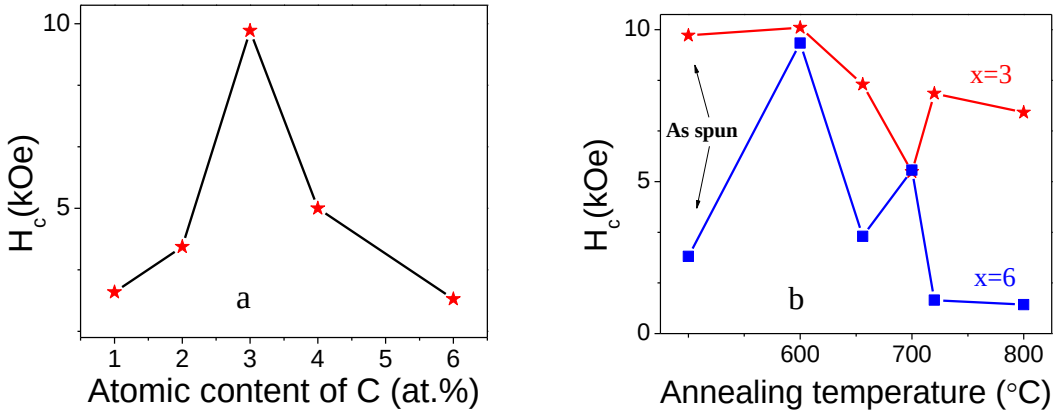

Fig. 6.6 (a) Coercivity as a function of C content for $(Sm_{0.12}Co_{0.88})_{100-(x+y)}Cr_yC_x$. (b) Coercivity as a function of annealing temperature for x = 3 and x = 6.

Often, annealing has the effect of either increasing or decreasing microstructure-dependent magnetic properties such as coercivity due to changes in grain size or phase evolution. Here, the unusual behavior of the coercivity increasing, decreasing, and then

increasing as a function of annealing temperature was observed for both x = 3 and x = 6 series (Fig. 6.6-b). The drastic decrease in coercivity for the x = 6 series at higher annealing temperatures is likely due to the precipitation of CrC and concomitant grain growth. Careful evaluation of the phase evolution and corresponding microstructural changes reveals possible causes at lower annealing temperatures. Fig. 6.5-a shows the region encompassing the (200) and (002) x-ray diffraction peaks for x = 3 annealed at various temperatures. This figure reveals dramatic changes in the peak positions as a function of annealing temperature, indicating significant changes in the unit cell dimensions as the crystallization process proceeds. This may in turn influence the magnetocrystalline anisotropy of the structure, influencing the coercivity. Additionally, the formation of the ordered Sm_2Co_{17} phase may also influence the magnetic behavior, as it has been reported to have lower magnetocrystalline anisotropy than the $SmCo_7$ phase [17]. The stronger effect in the x = 6 is likely due to the larger amorphous phase constitution, which can transform directly to the 2:17 structure [18].

Fig. 6.7 shows two typical hysteresis loops for the x = 3 series. Comparison with analogous materials such as those alloyed with Nb/Hf and C [6, 19] showed that the overall magnetization of the current materials is relatively low. The probable reason is that the 3d shells of Cr atoms are half filled which is a stable state, which might not contribute to the overall magnetic moment. Additionally the interaction with C between both Nb/Hf and Cr is rather different due to different electronegativities, which may also explain the magnetization differences. The two-phase shape of the hysteresis loops suggests limited exchange coupling between 2:17 and 1:7 phases as well.

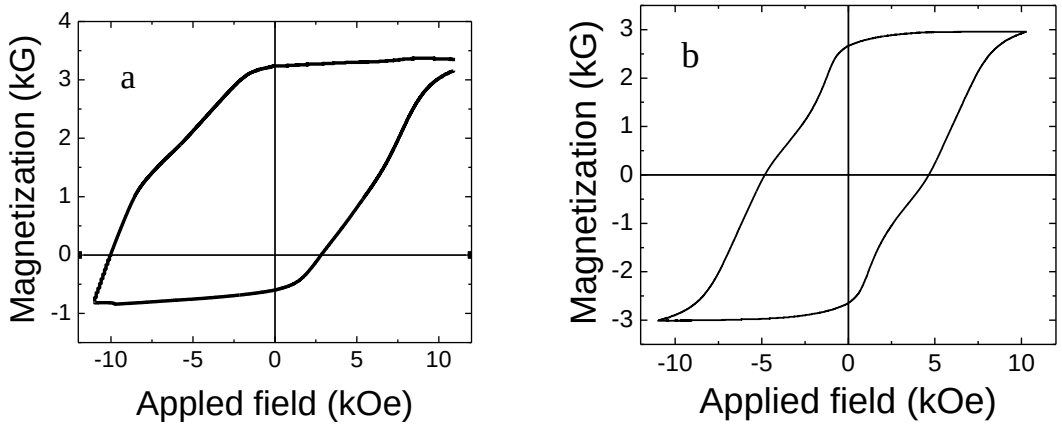

Fig. 6.7 M-H hysteresis loops for x = 3: (a) as-spun, and (b) after 800 ºC annealing

TEM revealed that the observed grain sizes of the as-solidified x = 3 samples were consistent with the Scherrer analysis, and selected area diffraction patterns confirmed the presence of the $SmCo_7$ phase with the $TbCu_7$-type structure (Fig. 6.8). The presence of the amorphous fraction was confirmed from the microstructures of both the as-spun sample (Fig. 6.8 (a)) and the one annealed at 600 °C (Fig. 6.8 (b)). Annealing of the x = 3 sample at 656 °C for 15 minutes produced the initial downward-trend in coercivity (Fig. 6.6-b), which was speculated to come from the large variations in the grain sizes (Fig. 6.8 (c)). For the x = 3 sample annealed at 700 °C (Fig. 6.8(d, e)), there are marked features in the microstructures. For instance, formation of finer grains, as seen in Fig. 6.8 (d), on the order of 30 nm, occurred. These refined grains result from the crystallization of the amorphous phase in the ordered Sm_2Co_{17} form, which was confirmed by the presence of the antiphase boundaries (APB) shown in Fig. 6.8 (e). The APB formation is characteristic of the ordered Sm_2Co_{17} structure, which led to the further deterioration of coercivity due to its lower magnetocrystalline anisotropy [17]. Previous work in Sm-Fe also revealed crystallization of the amorphous phase directly to the 2-17

structure [18]. Also, superlattice reflections corresponding to the Sm_2Co_{17} phase with the Th_2Zn_{17}-type structure were observed in the selected area diffraction pattern, further corroborating the formation of the Sm_2Co_{17} structure (inset). The microstructure of the x = 3 annealed at 720 °C (Fig. 6.8 (f)) showed an increase in the APB density compared with the sample annealed at 700 °C; the APBs can serve as effective pinning sites for domain wall propagation, increasing coercivity, while the more uniform structure can also enhance coercivity (Fig. 6.8 (g)). No chromium carbide precipitation was observed in TEM for any x = 3 samples.

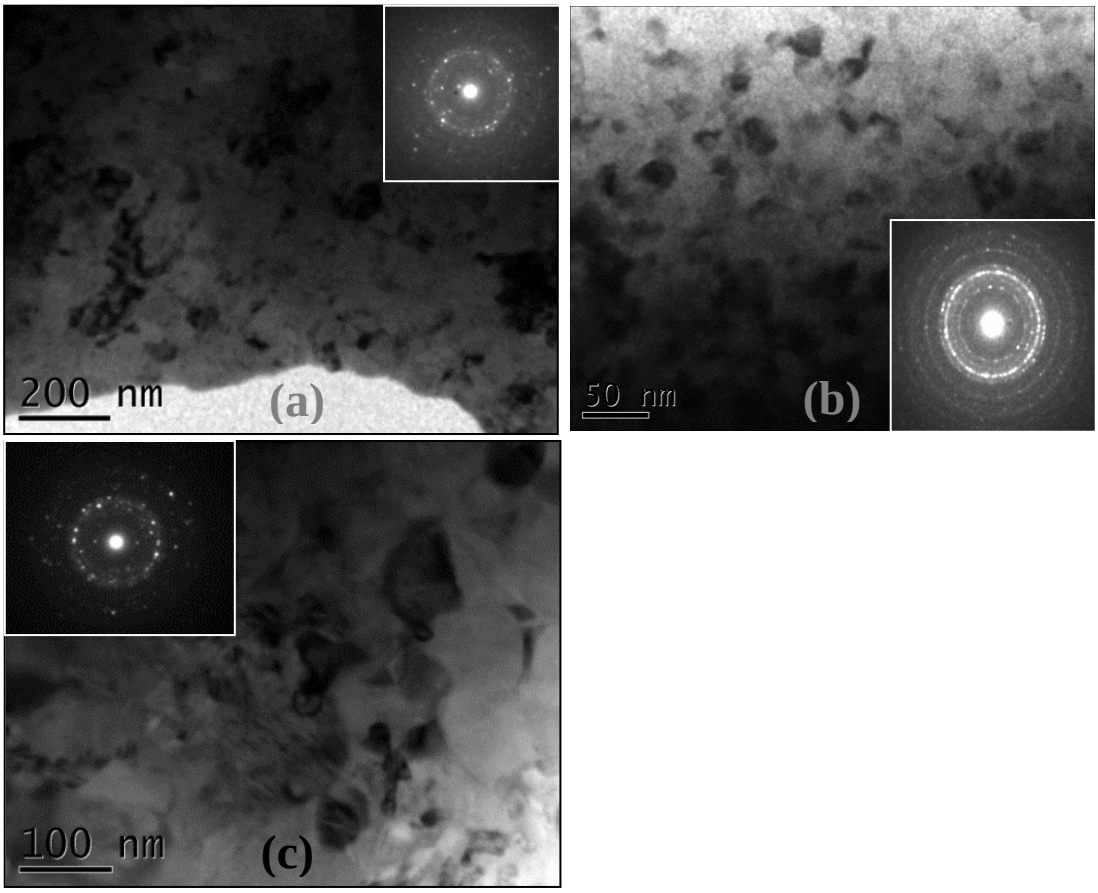

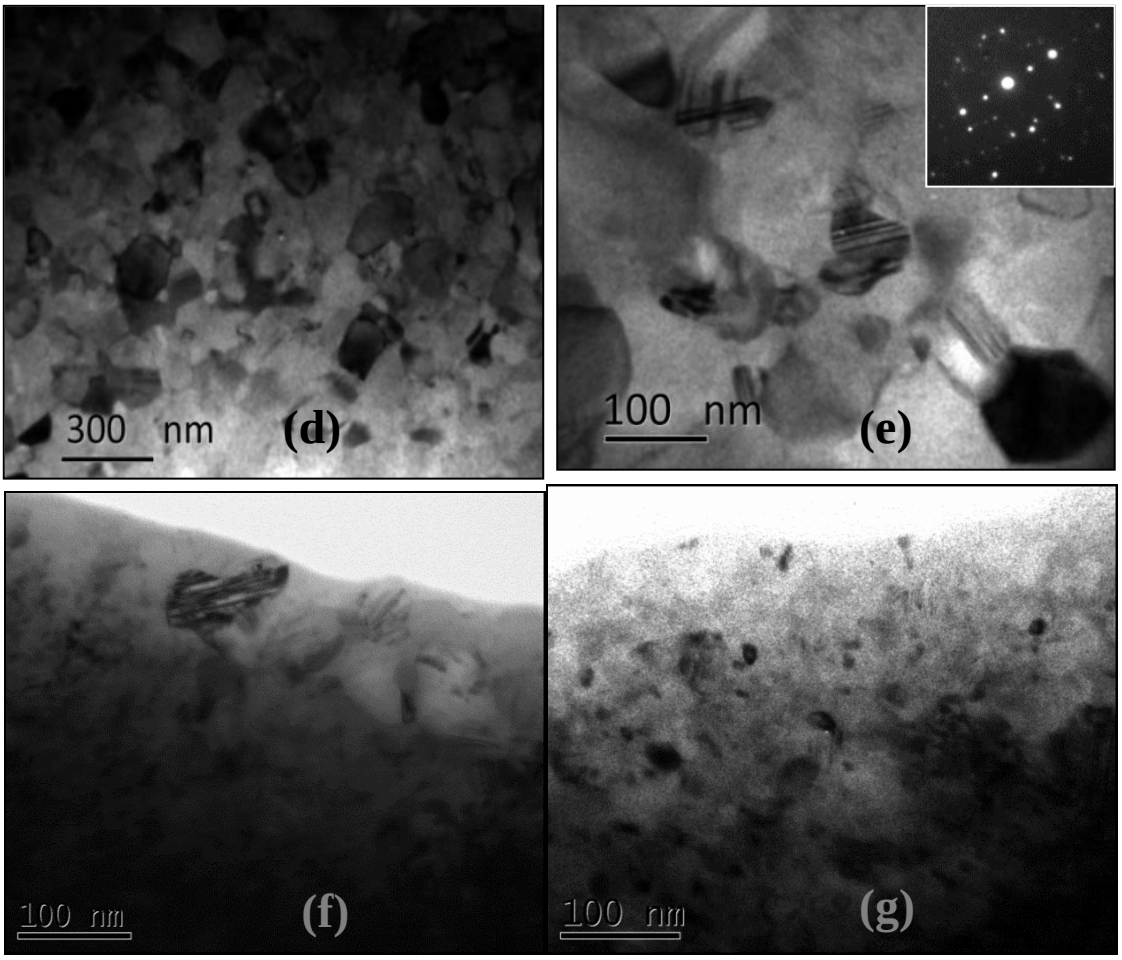

Fig. 6.8 TEM images for x = 3 series: (a) as-spun; after annealing at (b) 600 ºC; (c) 656 ºC; (d, e) 700 ºC; (f, g) 720 ºC. The insets show the selective area diffraction pattern of the corresponding images.

Initial magnetization curves were also obtained for the virgin samples in order to acquire some insight in the magnetization mechanisms. Fig. 6.9 shows typical initial magnetization curves for the x = 3 samples which exhibit features suggesting either nucleation or domain wall pinning magnetization behaviors or the combination. The changes in initial magnetization are associated with the changes in structure and

microstructures induced by both alloying and heat treatment. The presence of an amorphous phase acts as a nucleation site for the reversal due to their soft magnetic behavior whereas the development of APB may serve as pinning sites to inhibit the domain wall propagation through the strong crystalline misfit they created between boundaries. For instance, the magnetizations for the as-spun sample and the sample annealed at 656 °C showed a steep initial slope indicating a strong nucleation-controlled process [20], which resulted from the amorphous materials. The magnetization curve for the sample annealed at 700 °C showed an evident combination of nucleation and domain wall pinning magnetization processes, where the initial domain wall pinning came from the ineffective APB pinning and the latter nucleation magnetization part arose from the Sm_2Co_{17} grains. In comparison, the sample annealed at 720 °C showed more pronounced pinning mechanisms which indicates the effective pinning due to the appropriate density of APB. Further attempts can be made to better understand the mechanisms from the aspect of solid solution limit of the additions in the structure.

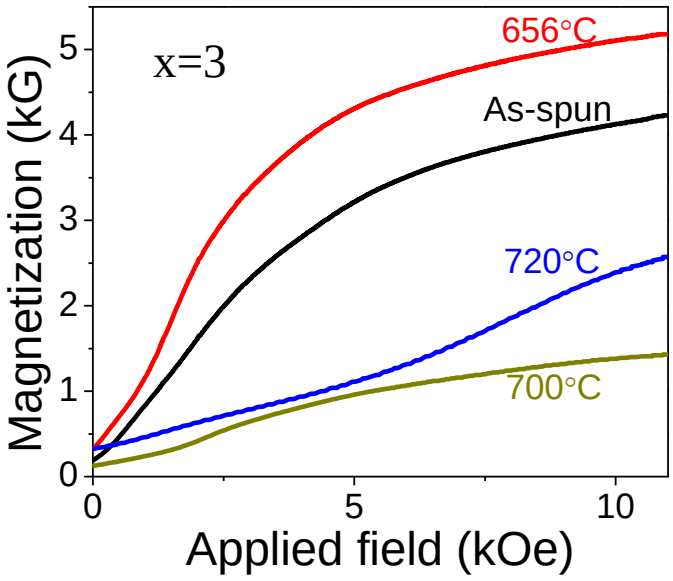

Fig. 6.9 Initial magnetization behavior of thermally demagnetized ribbons for samples with x = 3 under various conditions

6.4 Conclusions

In this study, the effect of Cr and C additions on the crystallization, phase formation and magnetic behavior were investigated for both the as-spun and the as-annealed Sm-Co based samples. Cr and C additions led to nanostructured permanent magnets whose grain size can be as small as 30 nm. The structural analysis, thermal analysis, microstructural analysis simultaneously showed that Cr and C can dramatically modify the microstructure of Sm-Co based alloys by changing the grain size and the phases present hence significantly impact the magnetic behavior. The maximum coercivity obtained was the sample with 3 at.% C and 4.5 at.% Cr alloy additions. Further investigations are still in need to better understand the underlying reasons which lead to

the unusual behavior after annealing. The observations here are intended to offer more insight in alloying modified Sm-Co based magnets which will further facilitate the optimization of the magnetic properties in this system.

Acknowledgements

The authors are grateful to the National Science Foundation under Grant No. DMR0804744.

References

[1] X. Jiang, J.E. Shield, J. Magn. Magn. Mater., 333 (2013) 63-68.

[2] R. F. Sabirianov, A. Kashyap, R. Skomski, S. Jaswal, D.J. Sellmyer, Appl. Phys. Let. 85 (2004) 2286-2288

[3] S.S. Makridis, G. Litsardakis, I. Panagiotopoulos, D. Niarchos, Y. Zhang, G.C. Hadjipanayis, IEEE Trans. Magn. 38 (2002) 2922-2924

[4] Z. Zhang, X. Song, W. Xu, M. Seyring, M. Rettenmayr, Scr. Mater., 62 (2010) 594-597

[5] K. Buschow, A. Van der Goot, Acta Crystallogr., Sect. B: Struct. Sci Crystallogr. Cryst. Chem., 27 (1971) 1085-1088

[6] S. Aich and J. E. Shield, J. Alloys Comp., 425 (2006) 416–423

[7] W. Manrakhan, L. Withanawasam, X. Meng-Burany, W. Gong, G. Hadjipanayis, IEEE Trans. Magn. 33 (1997) 3898-3900

[8] P. Saravanan, D. Arvindha Babu, V. Chandrasekaran, Intermetallics, 19 (2011) 651-656

[9] C. Hsieh, H. Chang, C. Chang, Z. Guo, C. Yang, W. Chang, J. Appl. Phys. 105 (2009) 07A705

[10] C. Hsieh, H. Chang, Z. Guo, C. Chang, X. Zhao, W. Chang, J. Appl. Phys. 107 (2010) 09A738

[11] C. Hsieh, H. Chang, X. Zhao, A. Sun, W. Chang, J. Appl. Phys. 109 (2011) 07A730

[12] W. Gong, J. Appl. Phys. 87 (2000) 6713-6715

[13] A. Yan, O. Gutfleisch, A. Handstein, T. Gemming, K.H. Muller, J. Appl. Phys. 93 (2003) 7975-7977

[14] M. Q. Huang, W. E. Wallace, M. Mchenry, Q. Chen, B. M. Ma, J. Appl. Phys. 83 (1998) 6718-6720

[15] Z. H. Guo, C. C. Hsieh, H. W. Chang, M. G. Zhu, W. Pan, A. H. Li. W. C. Chang, W. Li, J. Appl. Phys. 107 (2010) 09A705

[16] J. E. Shield, D. Branagan, C. Li, R. McCallum, J. Appl. Phys. 46 (1998) 5564-5566

[17] S. Aich, J. E. Shield, J. Magn. Magn. Mater. 279 (2004) 76-81

[18] J. E. Shield, J. Allo. Comp. 291 (1999) 222-228

[19] H. Chang, S. Huang, C. Chang, C. Chiu, W. Chang, A. Sun, Y. Yao, J. Appl. Phys. 101 (2007) 09K508

[20] G.C. Hadjipanayis and A. Kim, J. Appl. Phys. 63 (1988) 3310-3315

Chapter 7 Effect of Fe additions on structural and magnetic properties of $SmCo_{4-x}Fe_xB$ alloys

This chapter continues to investigate the effect of alloying in Sm-Co alloys obtained through melt-spinning. The structure of focus shifts to the $SmCo_4B$ (1:4:1) phase, a derivative of the $SmCo_5$ phase. The 1:4:1 phase is known for its high anisotropy constant (doubles that in the $SmCo_5$ phase). However the B substitution for Co atoms causes the dilution of the magnetization. This project aims to increase the magnetization through Fe additions and the findings have been published in ref [1].

The phase formation and magnetic behavior of $SmCo_{4-x}Fe_xB$ (x = 0, 0.25, 0.5, 0.75, 1 and 2) produced by melt spinning have been investigated. At x = 0, melt spinning resulted in the formation of the $SmCo_4B$ phase and an ultrahigh coercivity of 44 kOe at 300 K. Fe substitution resulted in the formation of an amorphous structure along with the $Sm(Co,Fe)_4B$ phase during melt spinning. A single $Sm(Co,Fe)_4B$ phase was observed after crystallization when $x < 1$, while $Sm(Co,Fe)_4B$ and $Sm_2(Co,Fe)_{17}B_y$ were observed when $x \geq 1$. Hysteresis loops at $x < 1$ displayed a single-phase magnetic behavior which was absent when $x \geq 1$. In the crystallized Fe-containing materials, an increase in both coercivity and magnetization with increasing Fe content was observed until x = 1. Initial magnetization curves revealed nucleation-controlled behavior at $x < 1$ and a combination of nucleation and domain wall pinning at x = 1 and x = 2. The average grain size for the annealed $SmCo_{4-x}Fe_xB$ samples measured from TEM micrographs was 110 nm for both x = 0.5 and x =1 and 90 nm for x = 2.

7.1 Introduction

Rare-earth/transition metal intermetallics, based on their strong anisotropy arising from the combined localized 4d and itinerant 3d magnetism, have been a research focus in the last few decades. In addition to the well-developed $SmCo_5$, Sm_2Co_{17} and $Nd_2Fe_{14}B$ compounds, efforts have also been given to other related systems [2, 3]. In particular, the substitution of B atoms for Co in the $SmCo_5$ structure results in the $SmCo_4B$ structure, where B replaces a Co atom in every second layer [4]. $SmCo_4B$ forms with the prototypical $CeCo_4B$-type hexagonal pseudo-binary structure [5]. The substitution of B atoms for Co increases the anisotropy field to 120 T at 4.2 K for the $SmCo_4B$ structure (compared to 71 T for $SmCo_5$) [6]; hence $SmCo_4B$ offers great potential as a hard magnetic material.

Most of the previous studies related to rare earth-transition metal borides [7-9] were based on conventional solidification techniques which results in relatively large grain sizes. Rapid solidification (e.g. melt spinning) can tremendously refine the microstructural scale of the product. Additionally, rapid solidification, a non-equilibrium processing, is also capable of producing other microstructural features—amorphous and metastable phases—which cannot be obtained during conventional solidification. The microstructural benefits can either directly alter magnetic properties or generate favorable properties after further engineering. For example, rapid solidification resulted in Co precipitates which successfully enhanced the remanence in $SmCo_7$ system [10]. A wide range of magnetic properties can be created through different post-processing of melt-spun NdFeB-based magnets [11, 12].

While the substitution of Co by the metalloid element B lowers the overall magnetization of $SmCo_4B$, additional substitution of Co by Fe is expected to increase the magnetization which has been observed in both YCo_4B [13] and $SmCo_7$ systems [14]. In addition, energy product, being an extrinsic parameter, is strongly affected by microstructure. For instance, in order to obtain the best properties in exchange-coupled magnets, the scale of the soft phase is optimally on the same order as that of the hard phase domain wall width [15].

The $SmCo_4B$ compound, bearing high magnetocrytalline anisotropy, is a potential candidate for a hard magnetic material, especially with magnetization enhancement through Fe substitutions. However, solubility limits of Fe in the $SmCo_4B$ structure are expected to be limited, given that the $SmFe_5$ base structure does not form. Additionally, the Fe may influence the solidification behavior, altering nanostructural evolution. The present investigation seeks to better understand the effect of nanostructuring on the phase formation and the magnetic properties of the $SmCo_4B$ compound, as well as the effect of Fe substitution on the phase evolution, structure, and magnetic properties of $Sm(Co,Fe)_4B$ alloys.

7.2 Experimental

Alloys with nominal compositions of $SmCo_{4-x}Fe_xB$ (x = 0, 0.25, 0.5, 0.75, 1 and 2) were made from high purity (> 99.95 %) elements by arc melting followed by melt spinning in high-purity argon atmosphere at a tangential wheel velocity of 30 m/s. An extra 5 wt. % of Sm was added to the sample in order to compensate for Sm loss due to

vaporization during melting. The resulting ribbons were less than ~35 μm thick, ~3 mm wide and with varying lengths.

Some of the ribbon samples were crushed to powder, mounted on an off-cut SiO_2 single crystal and analyzed by x-ray diffraction (XRD) using a Rigaku Multiflex x-ray diffractometer with Cu Kα radiation. The thermal behavior of the materials was studied by differential thermal analysis (DTA) using a Perkin-Elmer System 7 with a heating rate of 10 °C/min. For annealing, ribbons were first wrapped in tantalum foil and then sealed in quartz capsules with titanium granules inside in an ultra-high purity Ar atmosphere after repeated evacuations. Isothermal heat treatments were conducted at temperatures ranging from 700 °C to 900 °C for different time lengths followed by water quenching. The magnetic properties, measured parallel to the ribbon plane along the longer direction to minimize the demagnetizing effect, were measured using a superconducting quantum interference device (SQUID) magnetometer at 300 K with a maximum field of 7 T after pulse magnetizing under a 12.5 T field. Transmission electron microscopy (TEM) was performed using a JEOL 2010 operating at 200 kV and a Tecnai Osiris. Electron transparency was achieved by mounting ribbons on slotted Cu support grid and ion milling to perforation using a Gatan PIPS (Precision Ion Polishing System) at 4.5 kV. Long and short axes of individual grains were averaged to obtain grain size, and at least 20 grains were analyzed for each sample.

7.3 Results and discussion

The phase constitution of the $SmCo_4B$ alloy as a function of different annealing temperatures was examined by XRD. The diffraction pattern of the as-spun sample was

indexed to the $SmCo_4B$ phase (Fig. 7.1). XRD on ribbons and ground powders showed no detectable difference, which was indicative of random grain orientation typical for melt spinning at 30 m/s. The x-ray diffraction peaks were also broadened, suggesting a nanoscale grain structure. Scherrer analysis estimated the grain size to be ~30 nm. Similar refinement of the grain size has been observed in other B-containing rare-earth alloys [16-18]. However, no glass formation was observed, as was observed previously in Sm-Co-B alloys [18], as DTA did not reveal any exothermic phenomena indicative of crystallization events.

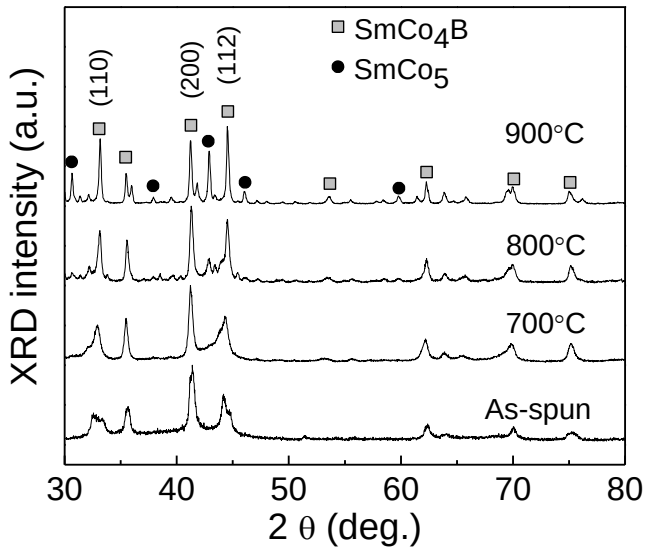

Fig. 7.1 X-ray diffraction patterns of $SmCo_4B$ in the as-spun and annealed states

Transmission electron microscopy (TEM) of the as-spun $SmCo_4B$ sample revealed aspects of the microstructure (Fig. 7.2). The as-solidified $SmCo_4B$ consisted of mostly equiaxed grains with sizes on the order of 50-100 nm, slightly larger than that determined from Scherrer analysis. This may be due to the small sample size typical of

TEM or the presence of structural disorder (i.e., strain) that contributed to the peak width but was unaccounted for in the peak width determination for the Scherrer analysis. Additionally, regions of spherulite crystals were also observed for as-solidified $SmCo_4B$. These appear to be regions where a number of crystals nucleated and grew in different directions from a single nucleation site. The lack of this feature in the $SmCo_5Fe_x$ analogue [19] suggests that B is critical for this feature to form.

Subsequent heat treatment of the $SmCo_4B$ as-spun samples resulted in the evolution of the $SmCo_5$ phase along with $SmCo_4B$ (Fig. 7.1). The phase fraction of $SmCo_5$ increased as the annealing temperature increased. The sharpening of the peaks in the as-annealed samples indicated grain growth.

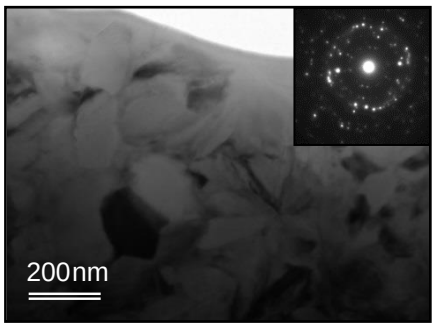

Fig. 7.2 TEM micrograph and the corresponding SAD pattern for as-spun$SmCo_4B$

The hysteresis curve of the as-spun $SmCo_4B$ sample displayed a smooth demagnetization curve with a coercivity of 44 kOe (Fig. 7.3). The initial magnetization behavior on a thermally demagnetized specimen implied a predominantly nucleation-controlled magnetization process [10], similar to what has been observed for $SmCo_5$ [20] but different from Al- and Ga-alloyed $SmCo_5$, which showed pinning-controlled behavior [21]. The heat treatment resulted in a monotonic decrease in coercivity with increasing annealing temperatures due to changes in the phase constituency and grain growth (Fig.

7.4). The hysteresis loop (Fig. 7.5) showed a slight kink at low field in the demagnetization behavior, which was suggestive of the existence of two or more magnetic phases with difference reversal fields. This two-phase behavior implied that the $SmCo_5$ and $SmCo_4B$ phases were not effectively exchange-coupled, which typically requires microstructural scales below ~20 nm [22]. The magnetization remained more or less stable before and after annealing with relatively low magnetization of ~300 emu/cm^3 due to the B dilution. The observed magnetization in $SmCo_4B$ is also lower than the reported calculated value of 670 emu/cm^3 [23] possibly because the applied field (70 kOe) is far below the anisotropy field (1200 kOe) of the material so that these experimental values at 70 kOe are significantly lower than true saturation values.

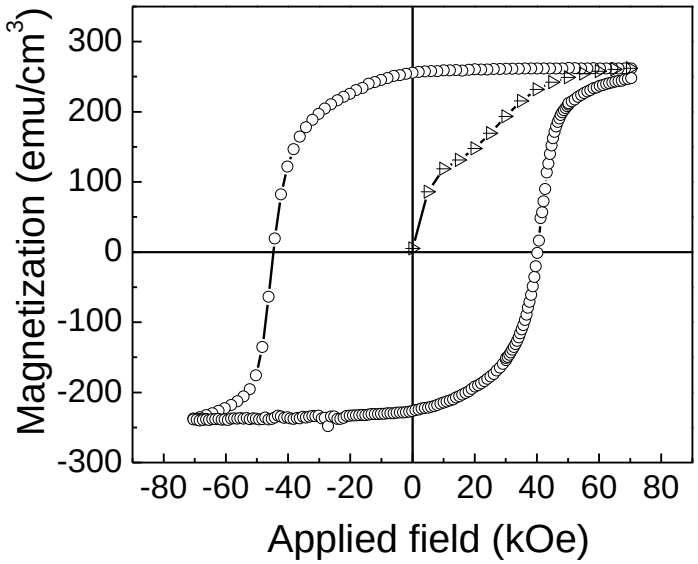

Fig. 7.3 Hysteresis loop for the as-spun $SmCo_4B$ ribbons

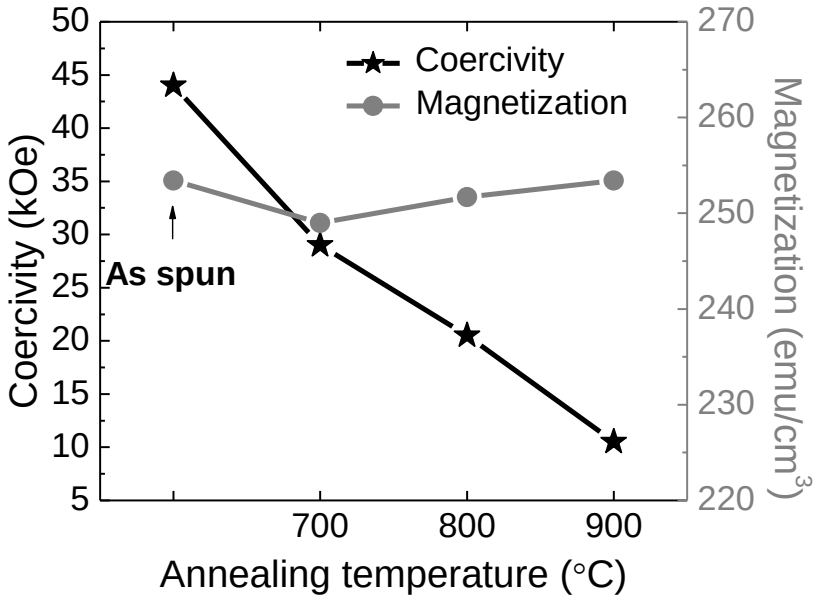

Fig. 7.4 Coercivity and magnetization ($H_{applied}$ = 70 kOe) of the as spun and annealed $SmCo_4B$ ribbons

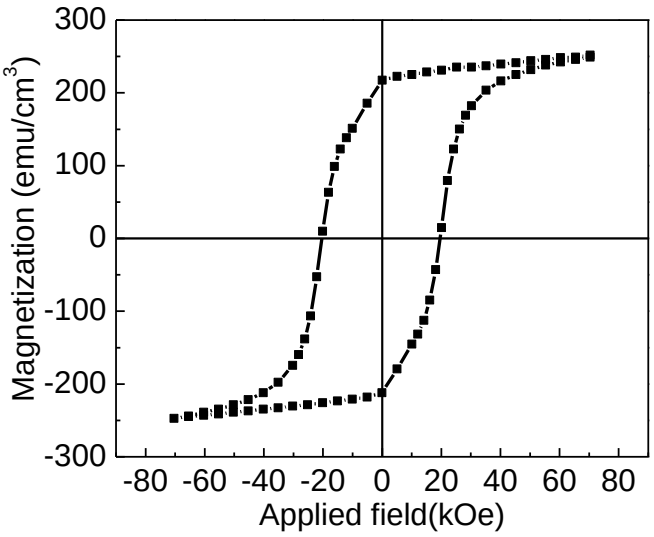

Fig. 7.5 Hysteresis loop for the $SmCo_4B$ sample after annealing at 800 °C

X-ray diffraction of the as-spun Fe-containing samples revealed the presence of both amorphous (indicated by the diffuse scattering feature centered at $2\theta \sim 40°$) and crystalline phases, with the crystalline peaks indexing to the $SmCo_4B$ structure (Fig. 7.6 and Fig. 7.7). Diffraction peaks were found shifting to the left indicating Fe substitution for Co which resulted in lattice expansion (Fig. 7.8). DTA showed strong exothermic peaks for all the Fe-containing as-spun samples. The increase in the crystallization temperature with increasing Fe content (Fig. 7.9) suggests that Fe enhanced the glass stability of the system.

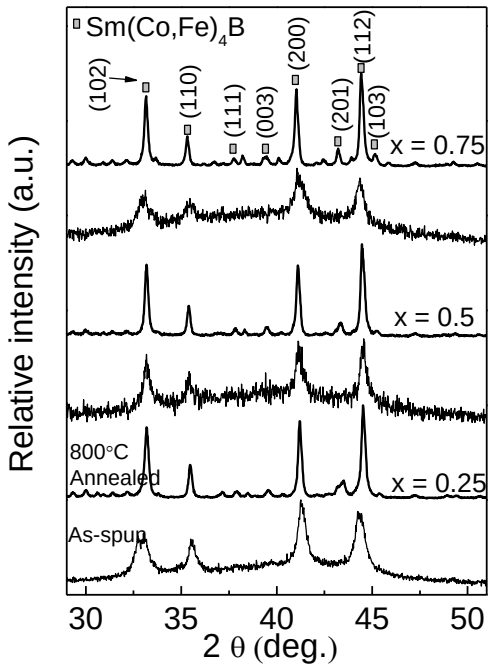

Fig. 7.6 XRD patterns of $SmCo_{4-x}Fe_xB$ (x = 0.25 – 0.75). The lower one represents the as-spun sample and the upper one 800 °C annealed sample, as denoted in x = 0.25

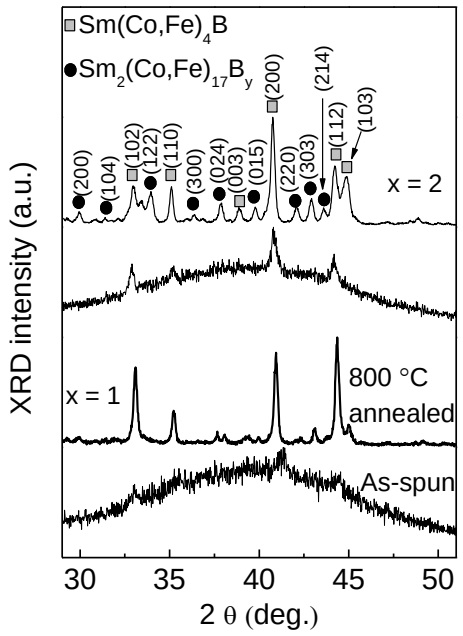

Fig. 7.7 XRD patterns of $SmCo_{4-x}Fe_xB$ (x = 1 – 2).The lower one represents the as-spun sample and the upper one 800 °C annealed sample, as denoted in x = 1

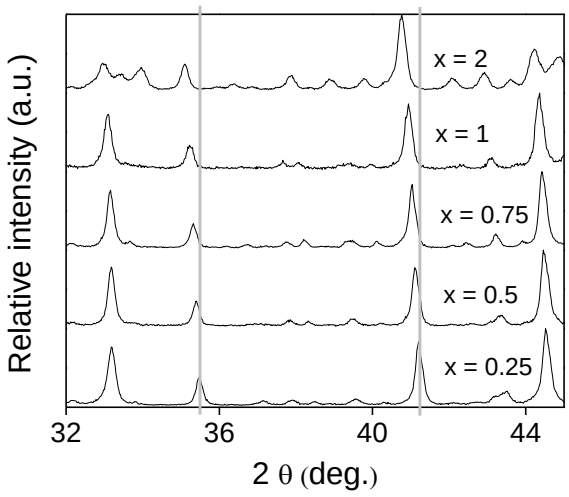

Fig. 7.8 X-ray diffraction patterns showing the peak shifting to the left with increasing Fe content

X-ray diffraction of the Fe-containing samples heat treated at 800 °C for 30 min is shown in Fig. 7.6 and Fig. 7.7. When $x < 1$, the diffraction revealed the presence of only hexagonal $Sm(Co,Fe)_4B$ (1:4:1), whereas when $x \geq 1$, rhombohedral $Sm_2(Co,Fe)_{17}B_y$ (2:17:y) phase was also detected. The 2:17:y phase is the interstitially-modified rhombohedral Th_2Zn_{17}-type structure [24, 25]. The differing phase formation in the Fe-containing alloys, specifically the apparent de-stabilization of the 1:4:1 phase, is likely due to the low solubility of Fe in the 1:4:1 phase. The 1:4:1 phase is a derivative of the $CaCu_5$-type $SmCo_5$ structure, and the $SmFe_5$ analog does not exist in the Sm-Fe equilibrium system. Thus, other Fe-containing phases necessarily form.

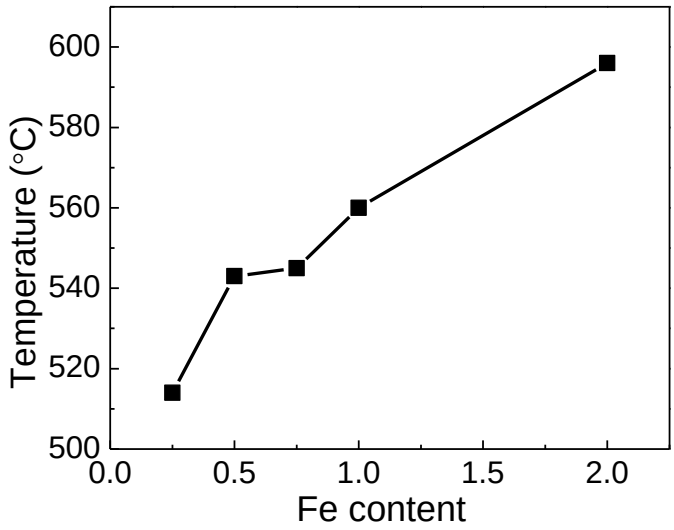

Fig. 7.9 Crystallization onset temperature from DTA for $SmCo_{4-x}Fe_xB$

The phase content for the annealed alloys was also corroborated by the initial magnetization behavior of the corresponding ribbon samples (Fig. 7.10) [10]. At $x < 1$, the alloys showed a predominantly nucleation-controlled magnetization behavior. However, when $x \geq 1$, the initial curves showed a distinctive combination of both

nucleation and domain wall pinning behavior. This is consistent with the x-ray diffraction showing two phases. The more pronounced nucleation trend in the x = 2 alloy implied early magnetization of the relatively soft 2:17:y phase.

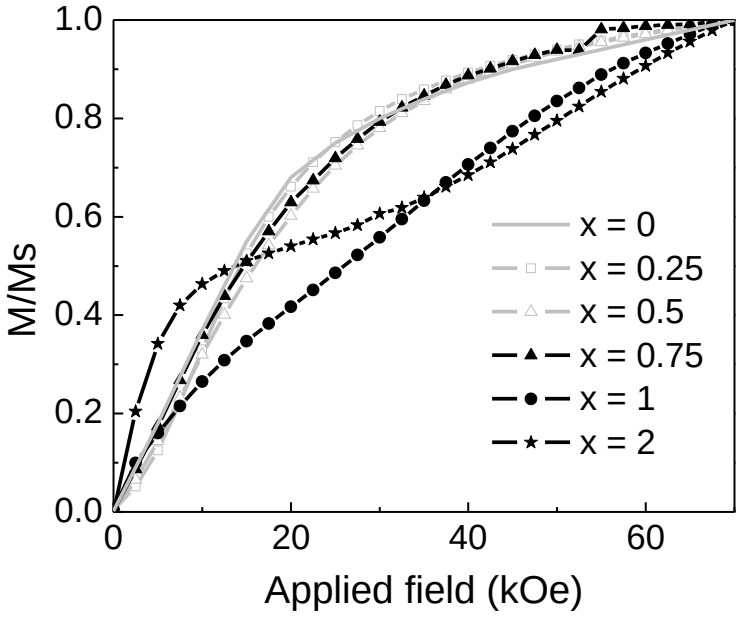

Fig. 7.10 Initial magnetization behavior of thermally demagnetized ribbons for 800 °C-annealed $SmCo_{4-x}Fe_xB$

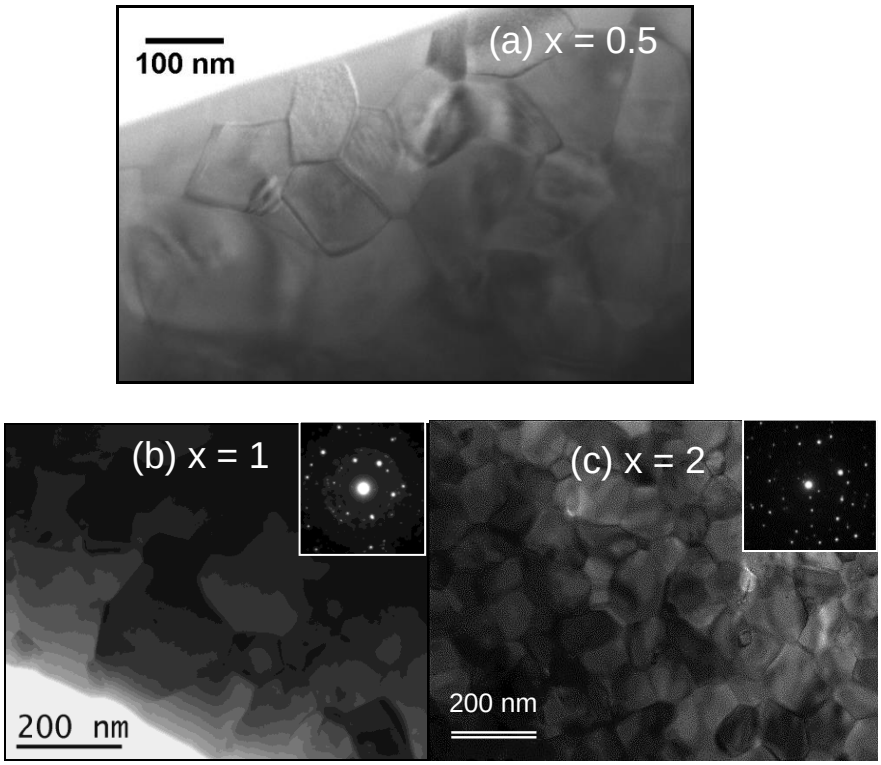

Fig. 7.11 TEM micrographs (with corresponding SAD patterns) for as-annealed $SmCo_{4-x}Fe_xB$ (x = 0.5, 1 and 2)

Fig.7.11 shows the TEM micrographs and statistical analysis of the grain sizes of heat treated $SmCo_{4-x}Fe_xB$ (x = 0.5, 1 and 2) samples. The annealed samples had equiaxed grains, which commonly occurs during crystallization from amorphous precursors formed during rapid solidification. Indexing of the SAD patterns matched well with the phases determined by x-ray diffraction. For x = 1, it is suspected that the larger grains resulted from the grain growth of the primary phase (1:4:1) during annealing, while the relatively smaller grains resulted from the crystallization of the secondary phase (2:17:y). Homogenous grain structure is observed in the x = 0.5 and x = 2 samples. Grain size was measured to be 110 ± 20 nm for x = 0.5 and x = 1 and 90 ± 20 nm for x = 2.

The Fe-containing samples showed soft magnetic behavior in the as-solidified state because of the large amorphous phase fraction. Heat treatment that resulted in crystallization dramatically improved the magnetic properties of all the Fe-containing samples (Fig. 7.12). Fig. 7.13 showed the second quadrant of the hysteresis loops which enables a closer examination. Generally, the annealed sample without any Fe (x = 0) showed the lowest magnetization and coercivity. As x increased, both magnetization and coercivity increased compared to the x = 0 alloy. However, pronounced two-phase magnetic behavior was observed when $x \geq 1$. The degree of the kink suggested that the volume fraction of the relatively soft phase, i.e., the 2:17:y phase, increased when x increased from 1 to 2. Note that there was a small kink in the x = 0.75 sample (Fig. 7.13), where the second phase fail to show in both x-ray diffraction and the initial magnetization behavior due to little volume fraction. On the other hand, saturation magnetization displayed a consistent increase with increasing Fe content.

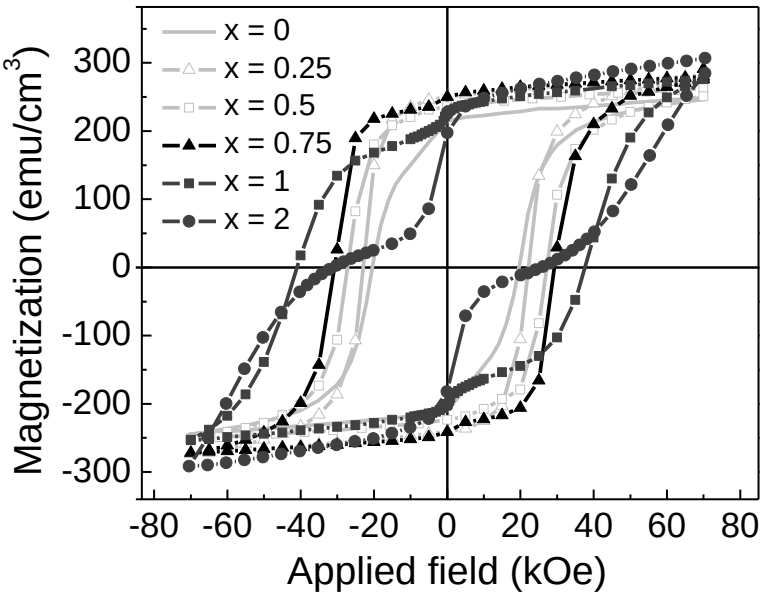

Fig. 7.12 Hysteresis loops for 800 °C-annealed $SmCo_{4-x}Fe_xB$

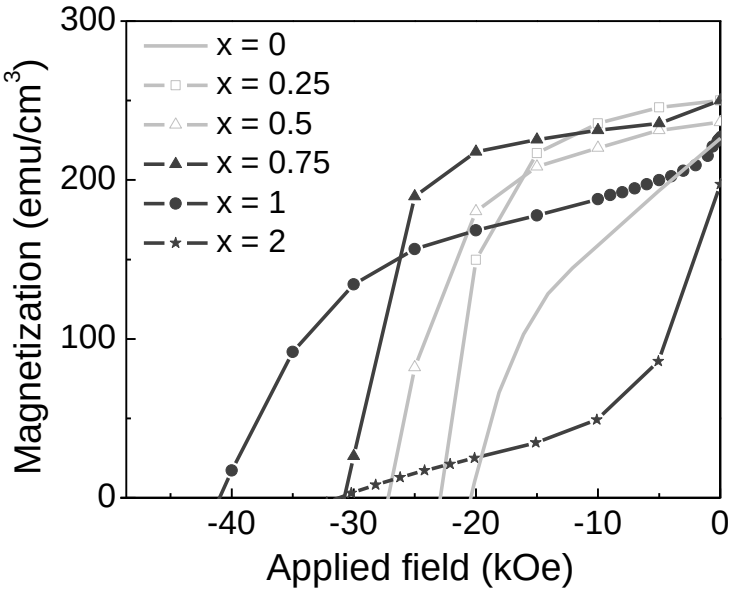

Fig. 7.13 Second quadrant of the hysteresis loops illustrated in Fig. 7.12

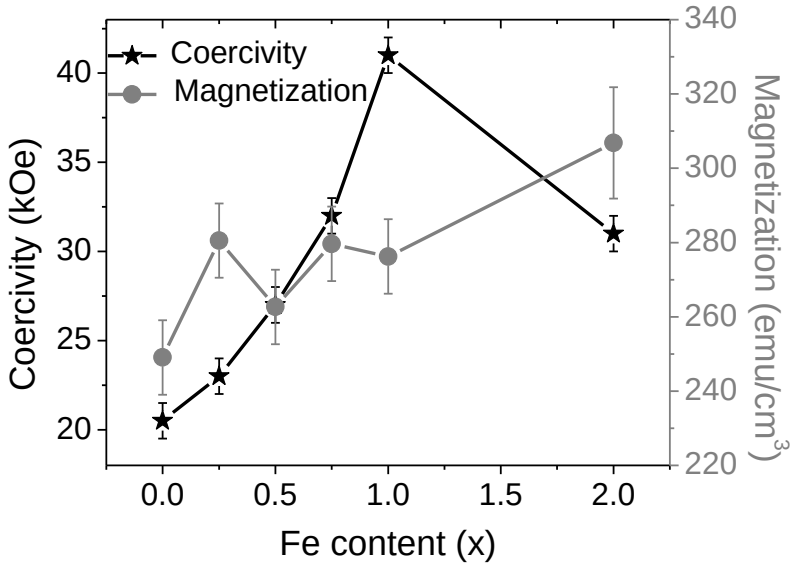

Fig. 7.14 Coercivity and magnetization ($H_{applied}$ = 70 kOe) change with respect to Fe content for $SmCo_{4-x}Fe_xB$ samples annealed at 800 °C (the bars on top of each data points denote the uncertainty involved in the measurement)

The coercivity variation of the annealed $SmCo_{4-x}Fe_xB$ is shown in Fig. 7.14. This change of coercivity is presumably due to changes in the magnetocrystalline anisotropy, given the fact that the samples underwent the same heat treatment procedure. The coercivity showed a continuous increase until x = 1, different from the behavior observed in melt-spun $SmCo_{5-x}Fe_x$ reported elsewhere [26], where Fe resulted in a decrease in coercivity. The disparity is likely due to B, which may both alter intrinsic magnetic properties and influence the microstructural and/or phase evolution. When x = 2, the switching field for the hard phase reached ~ 60 kOe, which is an increase compared to that at lower Fe concentrations. It appears that Fe additions increase the anisotropy field of the $SmCo_{4-x}Fe_xB$ phase. This in agreement with the theoretical calculation that Fe substitutions in $SmCo_{5-x}Fe_x$ increased the anisotropy field for $x \leq 0.35$ [27]. It is interesting that more Co can be substituted by Fe in $SmCo_4B$, observed here, than can substitute in $SmCo_5$, while enhancing magnetocrystalline anisotropy. The decrease in coercivity at x = 2 may result from the presence of two phases with different reversal behavior, as the hysteresis loops showed two-phase behavior, indicating little exchange coupling and the independent reversal of the 2:17:y and 1:4:1 phases. It is interesting to note that the interstitial B atoms appears to modify the magnetic behavior of the rhombohedral Sm_2Fe_{17} phase from easy plane to uniaxial anisotropy, given the relative hardness of the early-switching phase, which has been shown previously for interstitial modifications using N, C or B [24, 25] as well as for the Al [28] and Ga [29] modified compounds. As expected, with increasing Fe content, an overall increase in magnetization was observed with a maximum increase of 24 % at x = 2. Note that this

recorded magnetization is the value at $H_{applied}$ = 70 kOe, and is not necessarily the saturation magnetization.

7.4 Conclusions

The structural and magnetic behavior of the rapidly solidified Sm-Co-B alloys modified by Fe was investigated. Intrinsic properties, phase constitution and microstructure played a synergic effect on the change in magnetic properties. The giant coercivity of 44 kOe in $SmCo_4B$ phase was attributed to its high magnetocrystalline anisotropy and favorable microstructure. In the crystallized Fe-containing materials $SmCo_{4-x}Fe_xB$, x = 1 is seen to be the critical limit for both Fe substitution and the optimal magnetic properties. When x < 1, Fe substitution resulted in a single $Sm(Co,Fe)_4B$ phase and single-phase magnetic behavior; when x > 1, $Sm_2(Co,Fe)_{17}B_y$ crystallized out of the 1:4:1 phase which led to two-phase magnetic behavior. The increasing coercivity with increasing Fe content until x = 1 was attributed to its unusual magnetocrystalline anisotropy contribution to the 1:4:1 phase. Additionally, the microstructure of the annealed $SmCo_2Fe_2B$ showed a uniform distribution of grains which is potential in creating exchange-coupled nanocomposite magnetic material.

Acknowledgements

The authors are indebted to funding from the National Science Foundation under grant number DMR0804744 and Army Research Office under grant number W911 NF-10-1-0099. This research was performed in part in Central Facilities of the Nebraska Center for Materials and Nanoscience, which is supported by the Nebraska Research

Initiative. Valuable discussion with Dr. Ralph Skomski from Department of Physics and Astronomy in University of Nebraska-Lincoln is highly appreciated as well.

References

[1] X. Jiang, B. Balamurugan, J.E. Shield, Manuscript submitted, J. Allo. Compd., 2014.

[2] Y. Hou, Z. Xu, S. Peng, C. Rong, J.P. Liu, S. Sun, Adv. Mater., 19 (2007) 3349-3352.

[3] Z. Zhang, X. Song, W. Xu, M. Seyring, M. Rettenmayr, Scr. Mater., (2010) 594-597.

[4] Y. Kuzma, N. Bilonizhko, Sov. Phys. Crystallogr., 18 (1974) 447-449.

[5] H. Oesterreicher, F. Spada, C. Abache, Mater. Res. Bull., 19 (1984) 1069-1076.

[6] H. Ido, K. Sugiyama, H. Hachino, M. Date, S. Cheng, K. Maki, Physica B: Condensed Matter, 177 (1992) 265-269.

[7] H. Ido, H. Ogata, K. Maki, J. Appl. Phys., 73 (1993) 6269-6271.

[8] H. Ağıl, N. Kervan, S. Kervan, H. Sözeri, A. Gencer, J. Alloys Compd., 478 (2009) 437-440.

[9] P. Salamakha, O. Sologub, C. Mazumdar, E. Alleno, H. Noël, M. Potel, C. Godart, J. Alloys Compd., 351 (2003) 190-195.

[10] J. Shield, V. Ravindran, S. Aich, A. Hsiao, L. Lewis, Scr. Mater., 52 (2005) 75-78.

[11] Z. Liu, H. Davies, J. Phys. D: Appl. Phys., 42 (2009) 145006.

[12] Z.Q.J. Kung-Te Chu, Vamsi M Chakka and J P Liu, J. Phys. D: Appl. Phys., 38 (2005) 4006-4014.

[13] T. Dung, N. Thuy, N. Hong, T. Hien, J. Franse, J. Appl. Phys., 69 (1991) 4633-4635.

[14] J. Luo, J. Liang, Y. Guo, Q. Liu, F. Liu, L. Yang, Y. Zhang, G. Rao, J. Phys. Condens. Matter, 16 (2004) 4963.

[15] E.F. Kneller, R. Hawig, IEEE Trans. Magn., 27 (1991) 3588-3560.

[16] J.E. Shield, Y. Liu, R. Marr, Z. Chen, B. Ma, IEEE Trans. Magn., 40 (2004) 2901-2903.

[17] M. Huang, Z. Turgut, B. Smith, Z. Chen, B. Ma, S. Chu, D. Laughlin, J. Horwath, R. Fingers, IEEE Trans. Magn., 40 (2004) 2934-2936.

[18] Y. Horiuchi, S. Sakurada, J. Appl. Phys., 109 (2011) 07A733.

[19] I.C. Tung, H. Zhang, S.Y. Yao, J.C. Shih, B. Shen, T.S. Chin, J. Phys. D: Appl. Phys., 32 (1999) 1587.

[20] R. Ramesh, K. Srikrishna, J. Appl. Phys., 64 (1988) 6406-6415.

[21] A. Laslo, C. Colin, O. Isnard, M. Guillot, J. Appl. Phys., 107 (2010) 09A732-709A732-733.

[22] H. Davies, J. Magn. Magn. Mater., 157 (1996) 11-14.

[23] J.M.D. COEY, Magnetism and magnetic materials, in, Cambridge University Press, 2009, pp. 400.

[24] J. Coey, D. Hurley, J. Magn. Magn. Mater., 104 (1992) 1098-1101.

[25] H. Horiuchi, U. Koike, H. Kaneko, T. Kurino, H. Uchida, J. Alloys Compd., 222 (1995) 131-135.

[26] T. Saito, D. Nishio-Hamane, J. Alloys Compd., 585 (2014) 423-427.

[27] P. Larson, Mazin, II, Papaconstantopoulos, DA, Phys. Rev. B, 69 (2004) 134408.

[28] Z. Wang, R. Dunlap, J. Phys. Condens. Matter, 5 (1999) 2407.

[29] Z. Wang, R. Dunlap, Philos. Mag. B, 69 (1994) 103-111.

Chapter 8 Microstructure of multistage annealed nanocrystalline $SmCo_2Fe_2B$ alloy with enhanced magnetic properties

Chapter 7 has shown that Fe successfully increased the magnetization; however the resultant magnetic properties are far from ideal. For example, the kinky hysteresis loops and the low magnetization are obstacles for the magnets investigated in Chapter 7 to be utilized. The study in this chapter aims to further improve the magnetic properties of the composition possessing the best magnetization and coercivity—$SmCo_2Fe_2B$. Secondary heat treatment at a low temperature was attempted and led to intriguing magnetic properties changes. The causes of the changes are investigated using both TEM and 3D atom probe and will be discussed in this chapter. The results in this chapter have been published in ref [1].

The microstructure and chemistry of $SmCo_2Fe_2B$ melt-spun alloy after multistage annealing was investigated using high resolution transmission electron microscopy (HRTEM) and 3D atom probe tomography. The multistage annealing resulted in an increase in both the coercivity and magnetization. The presence of $Sm(Co,Fe)_4B$ (1:4:1) and $Sm_2(Co,Fe)_{17}B_x$ (2:17:x) magnetic phases were confirmed using both techniques. Fe_2B at a scale of ~ 5 nm was found by HRTEM precipitating within the 1:4:1 phase after the second-stage annealing. Ordering within the 2:17:x phase was directly identified both by the presence of antiphase boundaries observed by TEM and the interconnected isocomposition surface network found in 3D atom probe results in addition to radial distribution function analysis. The variations in the local chemistry after the secondary annealing were considered pivotal in improving the magnetic properties.

8.1 Introduction

Microstructure control is essential in improving the magnetic properties of materials [2, 3]. For example, grain size significantly influences coercivity in both hard and soft magnetic materials [4, 5]. Other microstructural features, such as phase distribution, morphology, texture, and defect structure also strongly impact magnetic behavior [6-8]. On the one hand, in exchange-spring magnets comprised of magnetically coupled soft and hard magnetic phases, the magnetic properties are mostly governed by their microstructures [9, 10]. Here the grain size of the soft phase is required to be in the same order as the domain wall thickness of the hard phase to achieve the optimal exchange coupling. Additionally, the volume fraction of phases, namely the phase distribution, is also critical in creating the maximum magnetic properties. For example, an energy product of 19.2 MGOe was obtained by distributing fine-grained α-Fe homogeneously within a $SmCo_5$ hard phase [11]. On the other hand, in the Nd-Fe-B system, the coercivity of a single magnetic phase—$Nd_2Fe_{14}B$—is greatly enhanced by a Nd-rich phase found in the grain boundaries, which effectively weakens the magnetic exchange interactions between the hard magnetic grains [12-14]. Structural defects also influence magnetic performance, such as the antiphase boundaries and twins found in $L1_0$ FePd which inhibit domain wall motion [15].

Developing favorable microstructures can be accomplished from a number of different processing routes. Annealing, involving both grain growth and chemical redistribution, is especially effective. The well-known SmCo 2:17-type permanent magnets adopt a multistage annealing procedure which incorporates homogenization followed by quenching, isothermal aging and slow quenching processes [16, 17]. The

high temperature (~ 1100 °C) homogenization is necessary to ensure uniform elemental distribution [9]. The isothermal aging at a temperature ~ 850 °C provides necessary phase decomposition and the diffusion of Sm atoms, whereas the slow quenching process at a lower temperature (~ 400 °C) facilitates the redistribution of transition metals which is fundamental in promoting the resultant intrinsic coercivity. In a similar fashion, the combination of homogenization (~ 1250 °C) and magnetic field isothermal aging (~ 800 °C) followed by cooling in Alnico magnets ensures the homogeneous distribution of spinodally decomposed phases of a strongly magnetic FeCo and a weakly magnetic NiAl [18, 19], which leads to the characteristic shape anisotropy and large remanence.

Inherently large coercivty and magnetization are both highly desired in permanent magnet design. We recently explored the possibility of combining the $SmCo_4B$ phase (with a high anisotropy field of 120 T [20]) and different levels of Fe substitution with the aim to obtain desirable permanent magnet properties. Different annealing approaches were employed for microstructural refinement. Alloys annealed at 800 °C in Ar atmosphere were referred to as primarily annealed alloys, the results of which can be found elsewhere [21]. Here, we show that a secondary, low-temperature annealing significantly improves both coercivity and remanence, and explore the mechanism through both atom probe and high-resolution microstructural analysis.

8.2 Experimental

An alloy with the nominal composition of $SmCo_2Fe_2B$ was made from high purity (> 99.95 %) elements using arc melting followed by melt spinning in ultra-high-purity

argon at a tangential wheel velocity of 30 m/s. An extra 5 wt. % of Sm was added to the sample in order to compensate for Sm loss due to vaporization during melting.

The as-spun alloy was first annealed at 800 °C for 30 min for crystallization (referred to as the primary annealing). The same set of samples subsequently underwent a secondary annealing, which was performed under a constant flow of either pure N_2 or pure Ar at 475 °C for 5 hours, followed by furnace cooling. The mass of the sample before and after the secondary annealing was carefully monitored to detect any gas absorption. This experiment was repeated several times on different sets of samples to ensure accuracy and reproducibility. X-ray diffraction (XRD) was performed for structural analysis on the crushed powder using a Rigaku Multiflex x-ray diffractometer with Cu Kα radiation. The magnetic properties were measured using a superconducting quantum interference device (SQUID) magnetometer at 300 K utilizing a Quantum Design Magnetic Property Measurement System (MPMS) with a maximum field of 7 T. The magnetic properties of all the samples were measured parallel to the ribbon plane along the longer direction to minimize the demagnetizing effect. The microstructure was investigated using transmission electron microscopy (TEM) using a Tecnai Osiris operating at 200 kV. Electron transparency was achieved by mounting ribbons on slotted Cu support grid and ion milling to perforation using a Gatan PIPS (Precision Ion Polishing System) at 4.5 kV. Samples for atom probe tomography were fabricated by focused ion beam lift-out process using an FEI Helios Nanolab focused ion beam system equipped with an Omniprobe nanomanipulator. APT experiments were conducted using CAMECA LEAP 4000 XHR system in voltage mode of evaporation using 40K sample temperature and evaporation rate maintained at 0.005 atoms per pulse.

8.3 Results and discussion

8.3.1 Magnetic enhancement

The primary annealing crystallized the material into a combination of hexagonal $Sm(Co,Fe)_4B$ (1:4:1) and rhombohedral $Sm_2(Co,Fe)_{17}B_x$ (2:17:x) phases (Fig. 8.1), which resulted in characteristic two-phase magnetic behavior with a high coercivity of 30 kOe (Fig. 8.2).

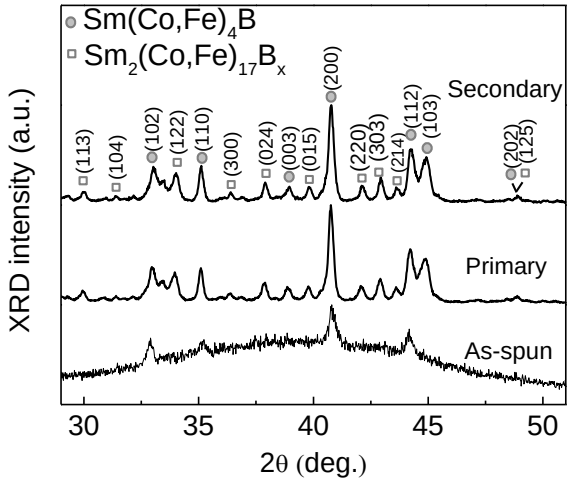

Fig. 8.1 X-ray diffraction patterns showing no differences between the primarily and multistage annealed samples

After annealing at 475 °C in flowing N_2, the alloy did not show an increase in mass, nor did a unit cell expansion occur, which would have been evident by x-ray diffraction peak shifts to lower angles (Fig. 8.1). However, the magnetic behavior exhibited significant changes (Fig. 8.2). Both coercivity and magnetization increased considerably, with the former increased from 30 kOe to 52 kOe. The increase of coercivity was not seen in the arc-melted $SmCo_2Fe_2B$ compound after the same processing [22], indicating that melt-spinning is necessary for enhanced magnetic

properties as a result of multistage annealing. It should be noted that the asymmetry of the complete loop is due to the limited magnetic field, resulting in the measurement of minor loops, which is very common for ultra-hard magnetic materials [23]. The same secondary annealing (475 °C for 5 h) was conducted in flowing Ar to determine if nitrogenation played a role in the magnetic changes. An identical increase in magnetic properties was observed, indicating that the secondary annealing induced subtle structural changes which enhanced magnetic performance and that the annealing atmosphere did not matter. The inability to interstitially modify the Sm_2Fe_{17} compound through nitrogenation suggests that the interstitial sites may already be occupied by B. The relatively large magnetic hardness and high coercivity of the two-phase materials corroborates this conclusion.

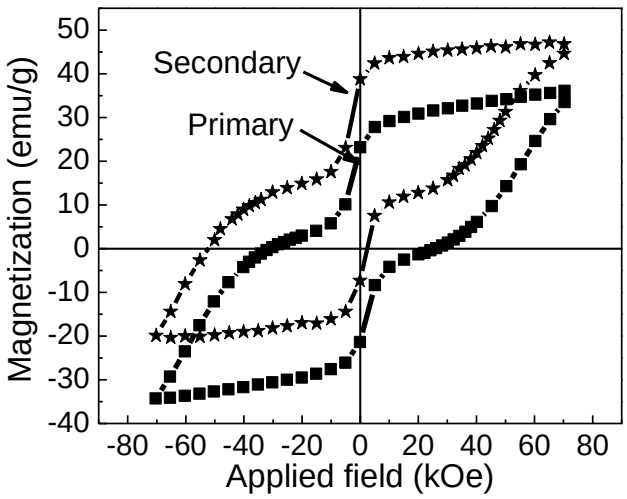

Fig. 8.2 Hysteresis loops for the annealed samples

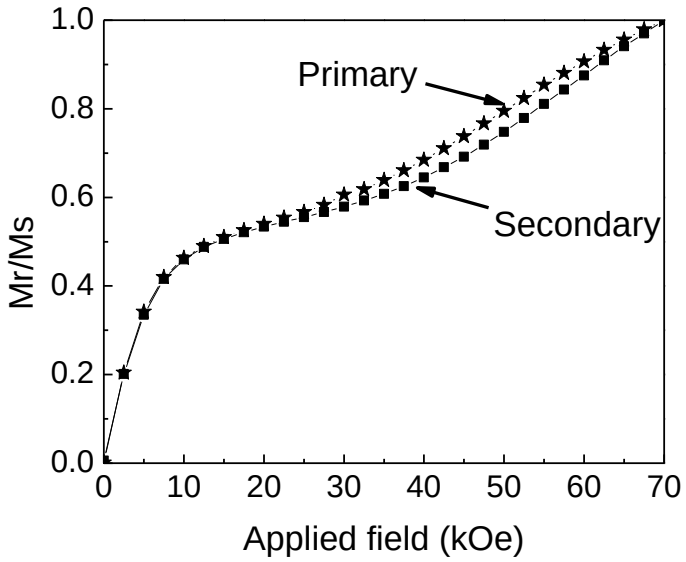

Fig. 8.3 Initial magnetization behavior of thermally demagnetized $SmCo_2Fe_2B$ ribbons after primary and multistage annealing

Initial magnetization curves (Fig. 8.3) of the samples after primary and secondary annealing revealed subtle changes in the magnetization process. Both samples exhibited combined pinning/nucleation-type magnetization, with predominantly nucleation behavior in the low-field regime, indicated by the sharp initial increase in magnetization. This shared nucleation behavior might indicate the invariance of grain size between the two samples, as it is below the single-domain limit for both phases. Both samples showed pinning character as well, indicated by the inflection in the initial magnetization curve. However, the multistage annealed sample showed a slightly stronger domain wall pinning behavior, indicated by a lower slope of the initial magnetization curve between approximately 20 and 40 kOe.

8.3.2 Microstructural observations

The microstructure for the alloy after primary annealing showed a uniform distribution of grains with a size of 105 ± 10 nm (Fig. 8.4). Selected area diffraction was indexed to both 1:4:1 and 2:17:x phases, consistent with what was determined from x-ray diffraction.

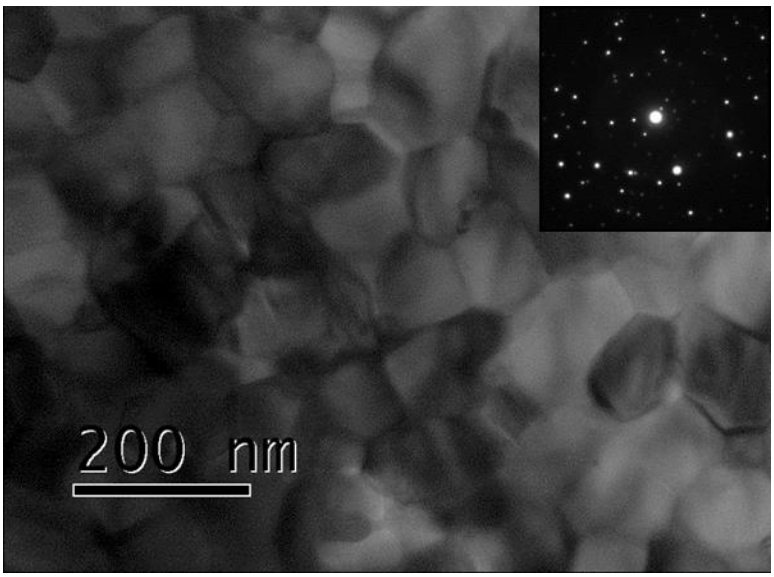

Fig. 8.4 TEM bright field micrograph of the primarily annealed ribbon

TEM studies of the sample after the secondary annealing were performed to determine the microstructural changes, and thus uncover the likely cause of the magnetic property enhancement. Fig. 8.5 (a) reveals that no grain growth occurred during the secondary annealing, as the grain size remained ~105 nm (Fig. 8.4). However, the appearance of ~ 5 nm precipitates was observed in some grains. Additionally, some grains developed planar defect structures reminiscent of antiphase boundaries (APB). High-resolution images coupled with fast Fourier transforms (FFTs) were used to identify the structures of the various phases. The phase with the APBs was determined to be the

2:17:x structure (Fig. 8.5 (b)). The APBs form as the ordering occurs in this structure [24, 25]. Grains of the 2:17:x phase do not contain the ~ 5 nm precipitates. The phase containing the precipitates was determined to be the 1:4:1 phase (Fig. 8.5 (c) and (d)). The lattice parameters determined for both the 2:17:x and 1:4:1 phases were reasonably close to those determined from x-ray diffraction results, and EDS results from individual grains revealed RE:TM ratios close to each of the phases. Specifically, the lattice parameters for the 1:4:1 phase determined from HRTEM were a = 5.57 ± 0.31 Å and c = 6.90 ± 0.30 Å. The a lattice parameter was significantly (~ 0.6 Å) larger than that reported for the pure $SmCo_4B$ phase [26], which is consistent with the unit cell expansion indicated from the peak shifts in the x-ray diffraction pattern [21]. This may be the result of Fe substitution into the structure, though the expansion is greater than would be expected. The structure of the precipitates was also identified by the lattice images and corresponding FFTs of high-resolution images. The lattice spacings observed were consistent with the tetragonal Fe_2B phase with a lattice parameter of 5.55 Å, close to the reported value [26]. This phase was not revealed in x-ray diffraction results because its small scale (~5 nm) would lead to significant peak broadening, making it difficult to observe with the other phases present, as well as its low volume fraction. It should be noted that the Moiré fringes also produced maxima in the FFTs, but these maxima were discounted when determining structures. The Fe_2B phase precipitated upon annealing at the lower temperature because the solubility of Fe and B in the 1:4:1 structure is lower than that at the elevated temperature. In other words, upon quenching from 800 °C, a supersaturated solution formed from which Fe_2B precipitated upon annealing at 475 °C.

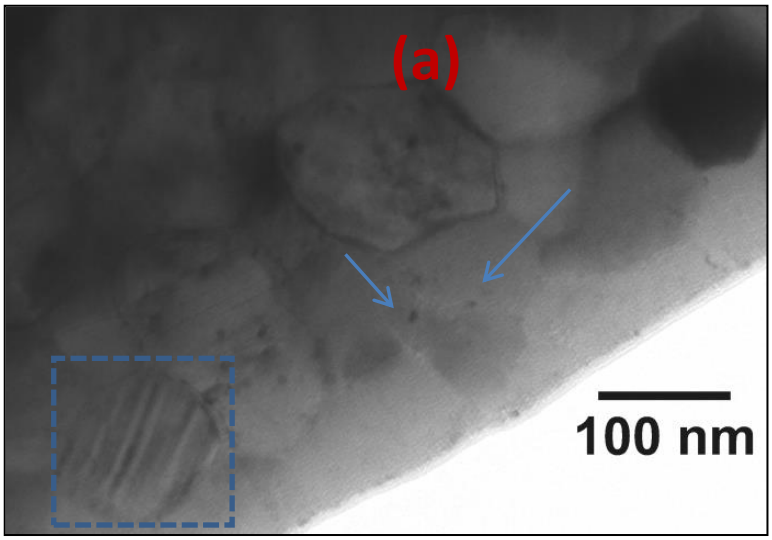
(a)
100 nm

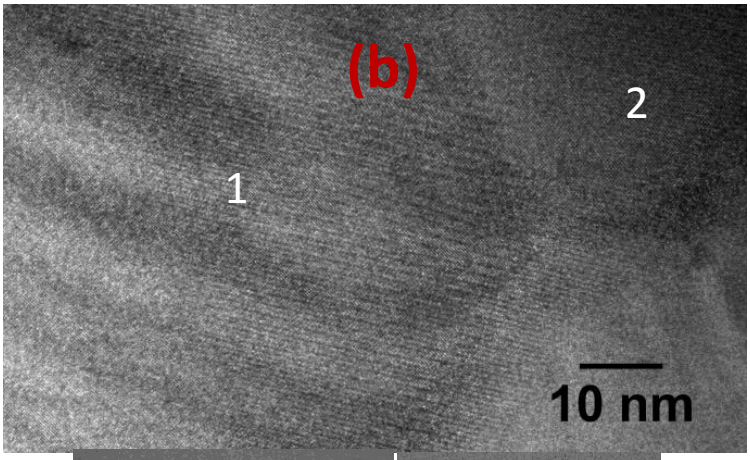
(b)
1
2
10 nm

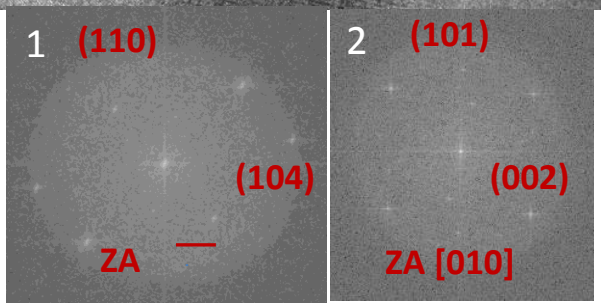
1
(110)
(104)
ZA
2
(101)
(002)
ZA [010]

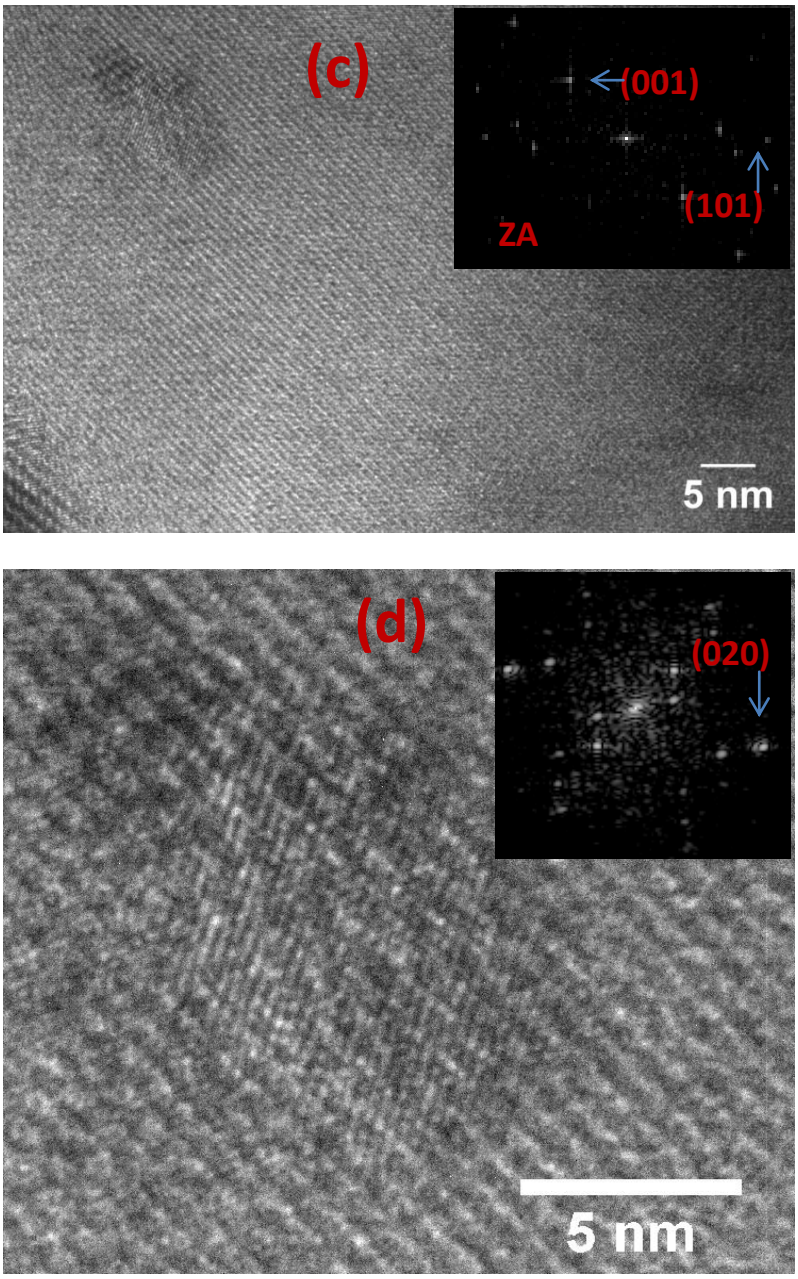

Fig. 8.5 Structural analysis on the multistage annealed sample

(a) TEM bright field micrograph with arrows pointing to precipitates and the dotted square indicating anti-phase boundaries. (b) HRTEM image of APBs, fast Fourier transforms (FFTs) for region 1 (2:17:x phase) and region 2 (1:4:1 phase) were indexed to [441] and [010] zone axis. (c) HRTEM of the precipitate, FFT for the matrix was indexed to [010] zone axis of the 1:4:1 phase. (d) A magnified view of the

precipitate with reflections from FFT being indexed to the (020) planes of the Fe_2B phase.

3D atom probe tomography, capable of providing sub-nanometer spatial resolution, three dimensional compositional analyses of materials [27-30] was employed to determine the local chemistry differences between the single-stage and multistage annealed samples. The APT results from the primarily annealed sample clearly showed evidence of both 1:4:1 and 2:17:x phases (Fig. 8.6(a)). The interface between the two phases is highlighted using a 44 at.% Fe isocomposition surface (Fig. 8.6(b)). The compositional partitioning across the two phases was quantified using a proximity histogram as shown in Fig. 8.6(c).

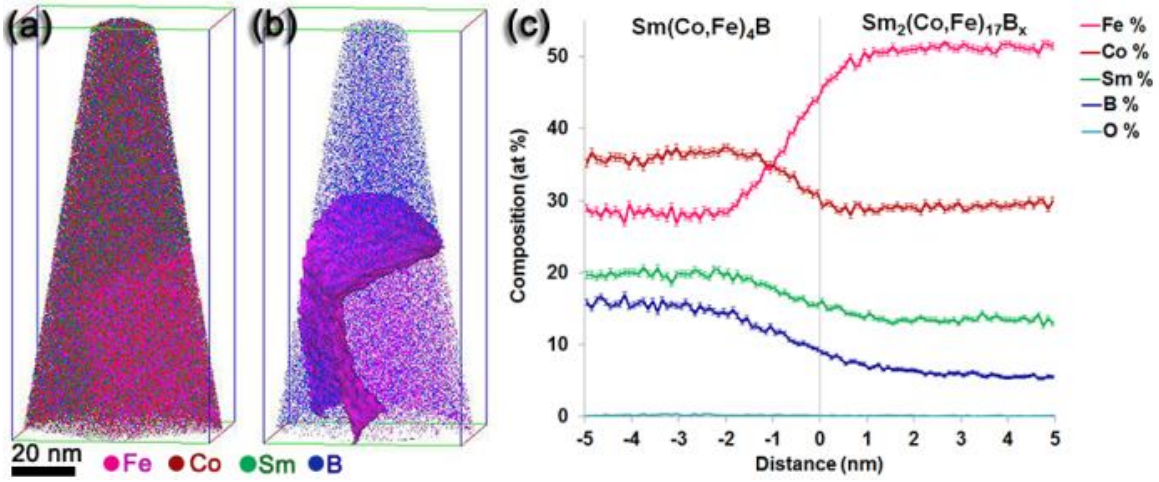

Fig. 8.6 (a) The APT reconstruction from the primarily annealed sample showing the distribution of Fe, Co, Sm and B. (b) The distribution of B and Fe shown at the interface between the two phases denoted by 44 at.% Fe isocomposition surface. (c) The compositional partitioning across the interface between two phases quantified by proximity histogram.

The APT results of the multistage annealed sample also revealed the presence of both 1:4:1 and 2:17:x phases (Fig. 8.7 (a)), with a substantial enrichment of oxygen along the interface (highlighted by dashed lines). The compositional partitioning across the interface estimated using a proximity histogram also showed clear enrichment of O up to 10 at.% at the interface. Additionally, a slight enrichment in Sm was also apparent, as its trend differed slightly from the other elements (Fig. 8.7 (b)), suggesting Sm-O formation. Since Sm is the most reactive of the constituents, this oxide formation might be expected. This high concentration of oxygen was not observed in the sample after only primary annealing, indicating that the low temperature annealing led to oxidation, with the grain boundaries being the high-diffusivity path.

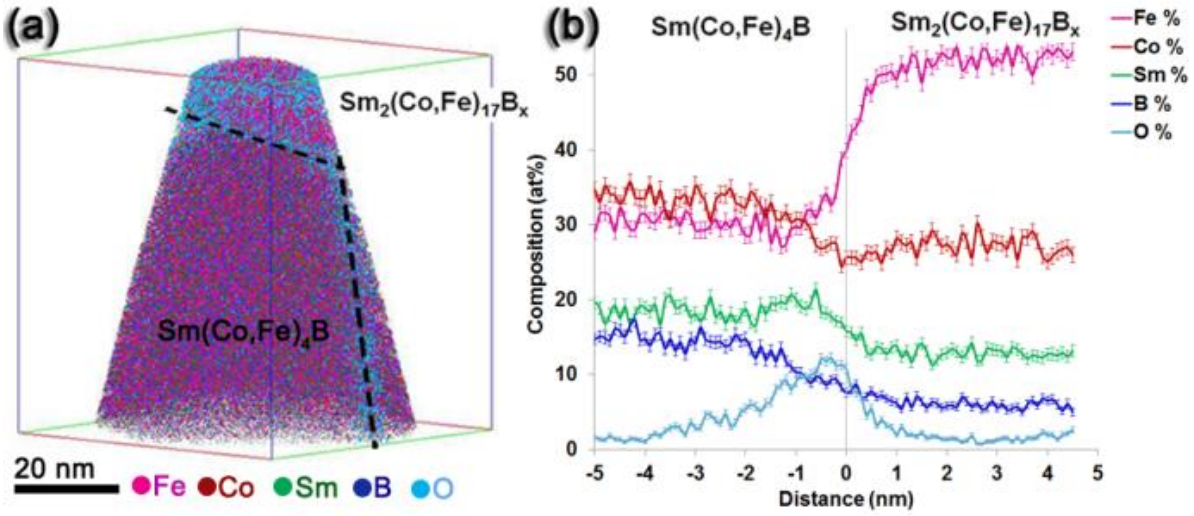

Fig. 8.7 (a) The distribution of Fe, Co, Sm, B and O ions shown in the multistage annealed sample. Clear O enrichment along the interface of the $Sm_2(Co,Fe)_{17}B_x$ and $Sm(Co,Fe)_4B$ phase shown by the overlaid dashed lines on the reconstruction. (b) The compositional partitioning between the two phases quantified using proximity histogram showing the substantially high O segregation (up to ~10 at. %) at the interface.

On detailed analysis of the 2:17:x phase in the multistage annealed sample, a non-random distribution of Fe and Sm was observed (Fig. 8.8(a)). This non-random distribution of Fe and Sm within the same region is also highlighted using 47 at. % Fe isocomposition surface (Fig. 8.8 (b)) and 12 at. % Sm isocomposition surface. These show an interconnected network of isocomposition surfaces (Fig. 8.8 (c)). In order to further quantify the deviation from randomness of local elemental distribution, radial distribution function (RDF) analysis of the 2:17:x phase data after both primary and multistage annealing were compared. The procedure and mathematical explanation of the RDF analysis is provided elsewhere [31]. RDF analysis of atom probe data has been used extensively for understanding solute ordering and clustering tendencies in aluminum alloys [32], titanium alloys [33], nickel-based alloys [34, 35], PbTe-based thermoelectric materials [36] and dilute magnetic semiconductors [37]. A value greater than 1 for the bulk normalized concentration derived through RDF analysis of APT data refers to a positive correlation, a value equal to 1 indicates a random distribution, and a value less than 1 indicates negative correlation. The RDF analysis of the 2:17:x phase data after primary annealing (Fig. 8.8 (d)) indicated a value of 1.06 for the bulk normalized concentration for Fe-Sm bonds, which reduced to 1.0 within 0.3 nm radial distance, whereas a negative correlation was observed for Fe-Fe bonds. After secondary annealing, the bulk normalized concentration of Fe-Sm increased to 1.12 and the positive correlation was observed to be prevalent until a 2 nm radial distance, which is a clear indication of the increased ordering tendency after secondary annealing. This conclusion also corroborates the APBs observed by TEM (Fig. 8.5).

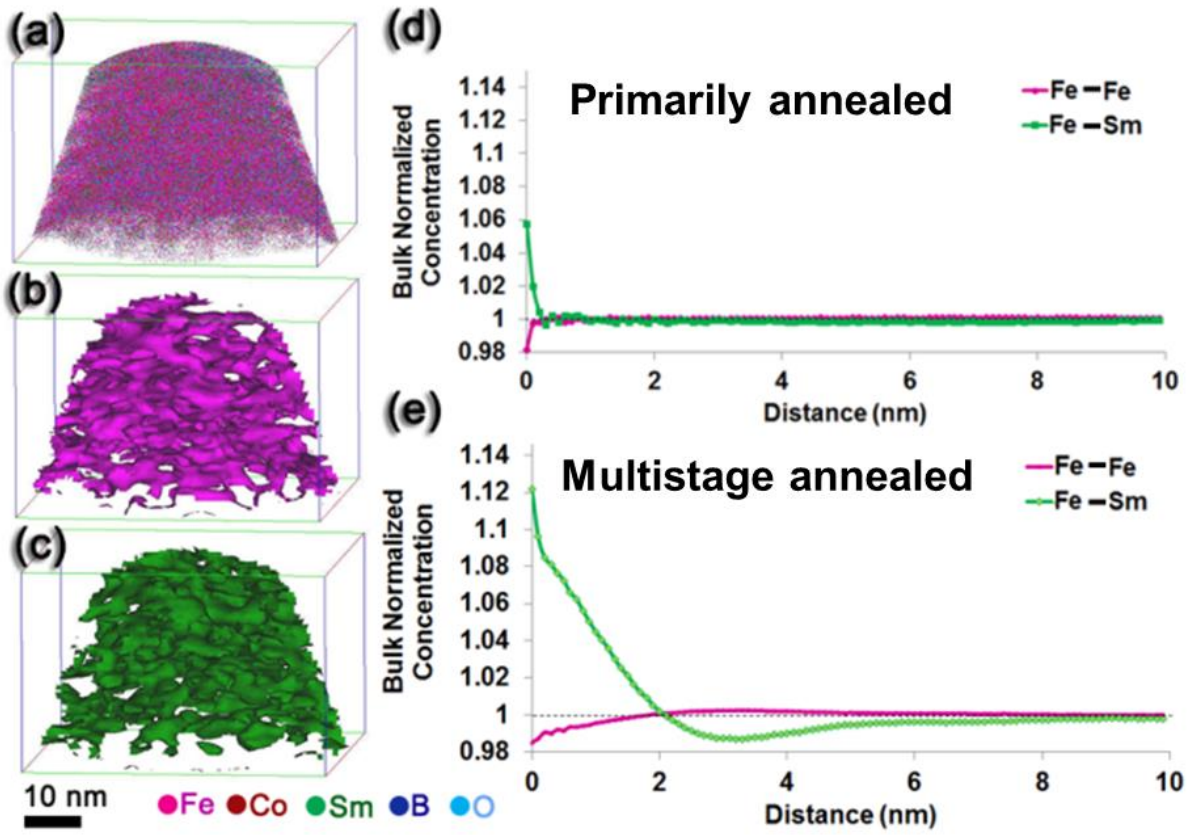

Fig. 8.8 (a) The distribution of Fe, Co, Sm, B and O in $Sm_2(Co, Fe)_{17}B_x$ phase after multistage annealing. (b) Inter-connected isocomposition surface of 47 at. % Fe and (c) 12 at. % Sm indicating presence of ordering. (d) Radial distribution function (RDF) analysis at Fe centers for quantifying compositional ordering in the $Sm_2(Co, Fe)_{17}B_x$ phase in primarily annealed condition showing very minimal ordering tendency whereas (e) shows a high degree of ordering based on the increased Fe-Sm bonds in the first 2 nm radial distance from the Fe centers in $Sm_2(Co, Fe)_{17}B_x$ phase after secondary annealing.

It should be noted that the kink in the second quadrant of the hysteresis loops for both samples resulted from ineffective exchange coupling between the two phases. The 1:4:1 phase and the 2:17:x phase bear different magnetocrystalline anisotropy, hence

resulting in different reversal behavior. In addition, the microstructural scale of both phases (~ 105 nm) is rather large for effective exchange coupling to occur [38].

The coercivity enhancements in the multistage annealed sample can be viewed as a synergetic effect of both the changes in intrinsic properties arising from compositional and structural changes, as well as the microstructural changes. Specifically, the precipitation of Fe-rich precipitates removed Fe from the 1:4:1 phase, increasing its magnetocrystalline anisotropy and thereby increasing the coercivity. Additionally, ordering within the 2:17:x phase could also affect the magnetic properties [39, 40]. Both ordering within the 2:17:x phase and the precipitation of the Fe_2B phase resulted in defects (APBs and precipitates) that are on the same order as the domain wall width, given by $\delta = \pi\sqrt{A/K}$. For $SmCo_4B$, δ is estimated to be 2.8 nm. Pinning centers must be of similar scale as the domain wall width to be effective in inhibiting domain wall motion [41]. The change in pinning behavior observed in the initial magnetization curves (Fig. 8.3) suggests that the APBs and/or precipitates act as pinning centers. It is most probable that the precipitates act as stronger pinning sites, since pinning strength is related to the difference in anisotropy constant K_1 between the main phase and pinning center [42].

Additionally, the formation of the grain-boundary oxide phase may also result in an increase in coercivity. In this case, the oxide acts to reduce the magnetostatic interactions between neighboring grains and promote nonuniform reversal of individual grains, resulting in an increase in coercivity. This is similar to the grain boundary phases in other systems, for example, the Nd-rich phase in Nd-Fe-B [13, 43] and the carbide in Sm-Co magnets [44].

The dramatic magnetization enhancement is due to the Fe_2B precipitation and possibly the ordering within the 2:17:x phase. Fe_2B phase is magnetically soft with a high magnetization; given the favorable grain scale (~ 5 nm), Fe_2B could enhance the remanent magnetization through intergranular exchange coupling [9, 45], which leads to a preference of the average alignment direction. Additionally, magnetization was found dependent on the ordering within $SmCo_7$ structure [46] and Heusler alloys [47]. Therefore, the ordering within the 2:17:x phase might also impact the magnetization.

8.4 Conclusions

Multistage annealed $SmCo_2Fe_2B$ alloy results in a tremendous increase in both coericvity and magnetization. Detailed microstructural investigation using TEM and 3D atom probe of the multistage annealed $SmCo_2Fe_2B$ sample revealed Fe_2B precipitation from the 1:4:1 phase, ordering within 2:17:x phase, and the formation of a thin oxide layer along the grain boundaries, all of which contribute to the increase in magnetic properties. Fe_2B precipitation out of the original $Sm(Co,Fe)_4B$ phase increased the magnetocrytalline anisotropy, hence contributing to the increase in coercivity. On the other hand, as a soft magnetic phase, nanosize Fe_2B grains also accounted for the magnetization enhancement due to its effective exchange coupling with the matrix. It is also suggested that by inhibiting the exchange interaction between the hard grains, the oxide layer might contribute to the increase in coercivity.

Acknowledgements

The authors are obliged to funding from Army Research Office under grant number W911 NF-10-1-0099 and Pacific Northwest National Laboratory Multiscale

Synthesis and Simulation Initiative. Arun Devaraj would like to acknowledge Thevuthasan Suntharampillai for the helpful discussions. A portion of the research described here was performed using Environmental Molecular Sciences Laboratory (EMSL), a national scientific user facility sponsored by the Department of Energy's Office of Biological and Environmental Research and is a part of the Chemical Imaging Initiative conducted under the Laboratory Directed Research and Development Program at Pacific Northwest National Laboratory (PNNL). EMSL is located at PNNL, a multiprogram national laboratory operated by Battelle Memorial Institute under Contract No. DE-AC05-76RL01830 for the U.S. Department of Energy.

References

[1] X. Jiang, A. Devaraj, B. Balamurugan, J. Cui, J.E. Shield, J. Appl. Phys., 115 (2014) 063902.

[2] O. Gutfleisch, J. Phys. D: Appl. Phys., 33 (2000) R157.

[3] T. Woodcock, Y. Zhang, G. Hrkac, G. Ciuta, N. Dempsey, T. Schrefl, O. Gutfleisch, D. Givord, Scr. Mater., 67 (2012) 536-541.

[4] G. Herzer, IEEE Trans. Magn., 26 (1990) 1397-1402.

[5] T. Schrefl, J. Fidler, H. Kronmüller, Phys. Rev. B, 49 (1994) 6100.

[6] K.M. Krishnan, Acta Mater., 47 (1999) 4233-4244.

[7] S. Li, B. Gu, H. Bi, Z. Tian, G. Xie, Y. Zhu, Y. Du, J. Appl. Phys., 92 (2002) 7514-7518.

[8] W.B. Cui, Y.K. Takahashi, K. Hono, Adv. Mater., 24 (2012) 6530–6535.

[9] E.F. Kneller, R. Hawig, IEEE Trans. Magn., 27 (1991) 3588-3560.

[10] H. Zeng, J. Li, J.P. Liu, Z.L. Wang, S. Sun, Nature, 420 (2002) 395-398.

[11] C. Rong, Y. Zhang, N. Poudyal, X. Xiong, M.J. Kramer, J.P. Liu, Appl. Phys. Lett., 96 (2010) 102513.

[12] H. Sepehri-Amin, T. Ohkubo, K. Hono, Acta Mater., 61 (2013) 1982-1990.

[13] H. Sepehri-Amin, T. Ohkubo, T. Shima, K. Hono, Acta Mater., 60 (2012) 819-830.

[14] K. Hono, H. Sepehri-Amin, Scr. Mater, 67 (2012) 530-535.

[15] T. Klemmer, D. Hoydick, H. Okumura, B. Zhang, W. Soffa, Scr. Metall. et Mater., 33 (1995) 1793-1805.

[16] L. Rabenberg, R. Mishra, G. Thomas, J. Appl. Phys., 53 (1982) 2389-2391.

[17] O. Gutfleisch, K.-H. Müller, K. Khlopkov, M. Wolf, A. Yan, R. Schäfer, T. Gemming, L. Schultz, Acta Mater., 54 (2006) 997-1008.

[18] F.E. Luborsky, J. Appl. Phys., 37 (1966) 1091-1094.

[19] Y. Iwama, M. Takeuchi, Trans. Jim, 15 (1974) 371-377.

[20] H. Ido, K. Sugiyama, H. Hachino, M. Date, S. Cheng, K. Maki, Phys. B: Condens. Matter, 177 (1992) 265-269.

[21] X. Jiang, B. Balamurugan, J.E. Shield, Manuscript submitted, J. Allo. Compd., 2014.

[22] H. Ido, O. Nashima, T. Takahashi, K. Oda, K. Sugiyama, J. Appl. Phys., 76 (1994) 6165-6167.

[23] D.L. Leslie-Pelecky, R.L. Schalek, Physical Review B, 59 (1999) 457.

[24] J. Shield, B. Kappes, B. Meacham, K. Dennis, M. Kramer, J. Alloys Compd., 351 (2003) 106-113.

[25] X. Jiang, J.E. Shield, J. Magn. Magn. Mater., 333 (2013) 63-68.

[26] P. Villars, ASM International, Rev Sub edition, (1998).

[27] Y. Chen, T. Ohkubo, M. Ohta, Y. Yoshizawa, K. Hono, Acta Mater., 57 (2009) 4463-4472.

[28] K. Hono, T. Ohkubo, Y. Chen, M. Kodzuka, K. Oh-Ishi, H. Sepehri-Amin, F. Li, T. Kinno, S. Tomiya, Y. Kanitani, Ultramicroscopy, 111 (2011) 576-583.

[29] H. Sepehri-Amin, T. Ohkubo, T. Nishiuchi, S. Hirosawa, K. Hono, Ultramicroscopy, 111 (2011) 615-618.

[30] S. Katakam, A. Devaraj, M. Bowden, S. Santhanakrishnan, C. Smith, R. Ramanujan, T. Suntharampillai, R. Banerjee, N.B. Dahotre, J. Appl. Phys., 114 (2013) 184901.

[31] F. De Geuser, W. Lefebvre, D. Blavette, Philos. Mag. Lett., 86 (2006) 227-234.

[32] C. Monachon, M.E. Krug, D.N. Seidman, D.C. Dunand, Acta Mater., 59 (2011) 3398-3409.

[33] A. Devaraj, S. Nag, R. Srinivasan, R.E.A. Williams, S. Banerjee, R. Banerjee, H.L. Fraser, Acta Mater., 60 (2012) 596-609.

[34] C.K. Sudbrack, R.D. Noebe, D.N. Seidman, Phys. Rev. B, 73 (2006).

[35] Y.Y. Tu, Z.G. Mao, D.N. Seidman, Appl. Phys. Lett., 101 (2012).

[36] I.D. Blum, D. Isheim, D.N. Seidman, J.Q. He, J. Androulakis, K. Biswas, V.P. Dravid, M.G. Kanatzidis, J. Electron. Mater., 41 (2012) 1583-1588.

[37] J.R. Riley, D.E. Perea, L. He, F. Tsui, L.J. Lauhon, J. Phys. Chem. C, 116 (2012) 276-280.

[38] E.F. Kneller, R. Hawig, IEEE Trans. Magn., 27 (1991) 3588-3560.

[39] B. Meacham, J.E. Shield, D. Branagan, J. Appl. Phys., 87 (2000) 6707-6709.

[40] S. Aich, J. Kostogorova, J.E. Shield, J. Appl. Phys., 97 (2005) 10H108.

[41] J. Livingston, J. Appl. Phys., 52 (1981) 2544-2548.

[42] J. Arcas, A. Hernando, J. Barandiaran, C. Prados, M. Vázquez, P. Marín, A. Neuweiler, Phys. Rev. B, 58 (1998) 5193.

[43] D.C. Crew, E. Girt, D. Suess, T. Schrefl, K.M. Krishnan, G. Thomas, M. Guilot, Phys. Rev. B, 66 (2002) 184418.

[44] S. Aich, V. Ravindran, J.E. Shield, J. Appl. Phys., 99 (2006) 08B521-508B521-523.

[45] H. Kronmüller, Nanostruct. Mater., 6 (1995) 157-168.

[46] S. Aich, J. Shield, J. Magn. Magn. Mater., 313 (2007) 76-83.

[47] P.J. Webster, J. Phys. Chem. Solids, 32 (1971) 1221-1231.

Chapter 9 Summary and conclusions

This chapter summarizes the dissertation and highlights some important experimental findings. The projects involved in this dissertation focus on microstructural control of the magnetic properties in Sm-Co-based magnetic materials.

At the $SmCo_7$ stoichiometry, Cr and C additions in the melt-spun ribbons successfully refined the grain size to as small as 30 nm. The structural and thermodynamic modifications induced by the additions significantly impacted the magnetic properties. The maximum coercivity of ~ 10 kOe obtained was the sample with 3 at.% C and 4.5 at.% Cr alloy additions. Annealing at different temperatures on this composition led to unusual magnetic changes which were considered a result of order-disorder transformations between $SmCo_7$ and Sm_2Co_{17} structures, corroborated by the microstructural observation using transmission electron microscopy.

For the $SmCo_4B$ stoichiometry, a giant coercivity of 44 kOe was obtained and was attributed to its high magnetocrystalline anisotropy and refined grain size. Fe substitutions for Co led to amorphorization in $SmCo_{4-x}Fe_xB$ as-spun materials. Annealing at 800 ºC revealed Fe effect on the structural and magnetic properties. Below 1 at.%, Fe substitution resulted in a single $Sm(Co,Fe)_4B$ phase and single-phase magnetic behavior; beyond 1 at.%, $Sm_2(Co,Fe)_{17}B_x$ crystallized out of the 1:4:1 phase which led to two-phase magnetic behavior. The increasing coercivity with increasing Fe content until 1 at.% of Fe was attributed to its unusual magnetocrystalline anisotropy contribution to the 1:4:1 phase.

The best composition found in terms of both magnetization and coericvity $SmCo_2Fe_2B$ underwent a secondary heat treatment at a lower temperature which led to a

tremendous increase in both attributes: the magnetization at 70 kOe increased from 36 emu/g to 47 emu/g while the coercivity increased from 30 kOe to 57 kOe. TEM, HRTEM and 3D atom probe revealed the possible causes. The Fe_2B precipitation (a soft phase with a large magnetization) from the 1:4:1 phase together with the ordering within 2:17:x phase were considered responsible for the increase in the magnetization. With regard to coercivity, Fe_2B precipitation out of the original $Sm(Co,Fe)_4B$ phase increased the magnetocrytalline anisotropy can possibly result in the enhanced coercivity. In addition, the precipitation and ordering, both on the order of the domain wall width of the hard phase, may also provide additional pinning effect, hence increased the coercivity. Lastly, the formation of a thin oxide layer along the grain boundaries is suspected to inhibit the exchange interaction between the hard grains contributing to the increase in coecivity.